

ERNEST ORLANDO LAWRENCE BERKELEY NATIONAL LABORATORY

Ultrafast Measurements of Chlorine Dioxide Photochemistry

RECEIVED NOV 0 6 1997 OSTI

Peter D. Ludowise

Chemical Sciences Division

August 1997 Ph.D. Thesis

MASTER

19980528 083

DTIC QUALITY INSPECTED 1

DISTRIBUTION OF THIS DOCUMENT IS UNLIMITED



DISCLAIMER

This document was prepared as an account of work sponsored by the United States Government. While this document is believed to contain correct information, neither the United States Government nor any agency thereof, nor The Regents of the University of California, nor any of their employees, makes any warranty, express or implied, or assumes any legal responsibility for the accuracy, completeness, or usefulness of any information, apparatus, product, or process disclosed, or represents that its use would not infringe privately owned rights. Reference herein to any specific commercial product, process, or service by its trade name, trademark, manufacturer, or otherwise, does not necessarily constitute or imply its endorsement, recommendation, or favoring by the United States Government or any agency thereof, or The Regents of the University of California. The views and opinions of authors expressed herein do not necessarily state or reflect those of the University of California.

Ernest Orlando Lawrence Berkeley National Laboratory is an equal opportunity employer.

Ultrafast Measurements of Chlorine Dioxide Photochemistry

Peter Daniel Ludowise Ph.D. Thesis

Department of Chemistry University of California, Berkeley

and

Chemical Sciences Division
Ernest Orlando Lawrence Berkeley National Laboratory
University of California
Berkeley, CA 94720

August 1997

Ultrafast Measurements of Chlorine Dioxide Photochemistry

by

Peter Daniel Ludowise

B.S. (University of Wisconsin-Madison) 1991

A dissertation submitted in partial satisfaction of the requirements for the degree of

Doctor of Philosophy

in

Chemistry

in the

GRADUATE DIVISION

of the

UNIVERSITY OF CALIFORNIA, BERKELEY

Committee in charge:

Professor Yongqin Chen

Professor Herbert Strauss

Professor Robert Dibble

Fall 1997

Ultrafast Measurements of Chlorine Dioxide Photochemistry

Copyright © 1997

by

Peter Daniel Ludowise

The U.S. Department of Energy has the right to use this document for any purpose whatsoever including the right to reproduce all or any part thereof

Abstract

Ultrafast Measurements of Chlorine Dioxide Photochemistry

by

Peter Daniel Ludowise

Doctor of Philosophy in Chemistry
University of California, Berkeley
Professor Yongqin Chen, chair

Time-resolved mass spectrometry and time-resolved photoelectron spectroscopy is used to study the ultrafast photodissociation dynamics of chlorine dioxide, an important constituent in stratospheric ozone depletion. Chapter 1 introduces these pump/probe techniques, in which a femtosecond pump pulse excites a molecule to a dissociative state. At a later time, a second femtosecond probe pulse ionizes the molecule. The resulting mass and photoelectron spectra are acquired as a function of the delay between the pump and probe pulses, which follows the evolution of the molecule on the excited state. A comparison to other techniques used to study reaction dynamics is discussed.

Chapter 2 includes a detailed description of the design and construction of the experimental apparatus, which consists of a femtosecond laser system, a molecular beam time-of-flight spectrometer, and a data acquisition system. The time-of-flight spectrometer is specifically designed to have a short flight distance to maximize the photoelectron collection efficiency without degrading the resolution, which is limited by the bandwidth of the femtosecond laser system. Typical performance of the apparatus is demonstrated in a study of the time-resolved photoelectron spectroscopy of nitric oxide.

The results of the time-resolved mass spectrometry experiments of chlorine dioxide are presented in Chapter 3. Upon excitation to the A 2A_2 state near 3.2 eV, the molecule dissociates through an indirect two-step mechanism. The direct dissociation channel has been predicted to be open, but is not observed. A quantum beat is observed in the OClO+ species, which is described as a vibrational coherence of the optically prepared A 2A_2 state.

Chapter 4 presents the results of the time-resolved photoelectron experiments of chlorine dioxide. At short delay times, the quantum beat of the OCIO+ species is observed in the X ¹A₁ state of the ion. At infinite delay, the signal is dominated by the ClO+ ion, observed in a variety of electronic states. The photoelectron data is shown to support the indirect two-step dissociation mechanism derived from the mass results. Conclusions of the mass and photoelectron results are discussed in context of the stratospheric ozone depletion problem.

This work is dedicated to my loving wife, Susy.

Table of Contents

Abstract	1
Dedication	iii
Table of Contents	iv
Acknowledgments	vii
Chapter 1. Introduction	1
References	6
Chapter 2. Experimental Apparatus	9
2.1 Time-of-flight Mass Spectrometry	10
2.2 Time-of-flight Photoelectron Spectroscopy	11
2.21 Resolution Considerations	15
2.3 Femtosecond Laser System	18
2.31 Femtosecond Oscillator	19
2.32 Stretcher	24
2.33 Regenerative Amplifier	27
2.34 Compressor	30
2.35 Pump and Probe Generation	33
2.4 Molecular Beam Apparatus	37
2.41 Free Jet Expansion	37
2.42 Molecular Beam Chamber	39
2.421 Source Chamber	41
2.422 Differential Chamber	43
2.423 Ionization Chamber	43
2.424 Flight Tube	47

2.425 Light	Baffles
2.426 Detect	or
2.5 Data Acquisiti	on System
2.6 Calibration	<i>.</i>
2.61 Nd:YAG	$655\mathrm{nm}$ ns Data 6
2.7 Time-resolved	Photoelectron Spectroscopy of NO6
2.8 Mass Calibrati	on
References	7
Chapter 3. The Photo	odissociation Dynamics of Chlorine Dioxide
Studied by	y Time-resolved Mass Spectrometry8
3.1 Introduction	8
3.2 Experimental .	8
3.3 Results and Di	scussion9
3.31 Product Ki	netic Model9
3.32 OClO Quar	ntum Mechanical Model
3.4 Conclusion	
References	
Chapter 4. The Photo	dissociation Dynamics of Chlorine Dioxide
Studied by	Time-resolved Photoelectron Spectroscopy
4.1 Introduction	
4.2 Experimental	
4.3 Results and Dis	scussion
4.31 Short Pump	/Probe Delay Assignment
4.32 40 ps Delay	Assignment
122.0	of Mass and Photoelectron Data12

4.4 Conclusion	127
References	129
Appendix 1. Derivation of the Two-step Photodissociation Model	131
References	135

Acknowledgments

When I arrived at Berkeley six years ago, I expected a very challenging experience that would make me grow as a scientist, but I never expected to grow as a person as much as I have. Graduate school has been the most difficult task I have ever taken, but I do believe that I am a better person because of it. Now that I have completed this manuscript, I have a chance to thank all of the people who have helped along the way.

First, I would like to thank my advisor, Yong Chen, for an opportunity to work in his group. I chose to work for a new professor so I could maintain a close relationship with him or her through out my career. It certainly is a gamble, but I have learned more from him than I thought possible. His eternally optimistic attitude, especially in the face of adversity, was a constant source of strength.

The other members of my group have also been a great deal of help. Matt Blackwell was my closest associate. His experience in vacuum equipment and computers was essential in the construction of this experiment. If things do not work too well at George Lucas' I.L.M., I hope he opens a microbrewery. Lukas Hunziker, the resident laser expert, helped me many times in operating and maintaining the laser system. Special thanks goes to him for showing me the meaning of Capitola. Dali Xu, a post-doctoral associate, helped in putting the laser system together. Mike Morgen's sense of humor always helped me get through the tough times, and our Yosemite trips will forever remind me of how bad camping can be when you are soaking wet. Bill Price, a former member of the group, was always a source of stimulating discussions.

As a new research group, our resources were quite limited. We relied heavily on the friendly groups of D level to loan us equipment essential for the construction of the molecular beam chamber. The Saykally, Neumark, Lee, and Somorgai groups were especially helpful. Special thanks goes towards David Mordaunt and Harry Beal. Dave is a

great friend who helped me in lab and on the hills of the Sierra. Harry is also a great friend who always had time to listen to my adversities and offered suggestions to alleviate them.

The department staff was always supportive to our needs. Eric Granlund in the machine shop always bent over backwards in helping us design and construct the chambers. He also kept an eye out for us to save time and money in building the experiment. Tom Lawhead in the glass shop also rushed jobs in emergencies to help us. Ron Dal Porto was a source of help in the student shop in showing Matt and I how to 'do-it-yourself', which was essential in our group. Peggy Southard, the group secretary, also worked well under adverse conditions to keep the group together.

The one person who really made it possible for me to finish is my wife, Susy. I cannot thank her enough for all of her support. Now that she has returned to school, hopefully I can do the same for her.

Chapter 1

Introduction

One of the primary goals of modern physical chemistry is the understanding of reaction dynamics. Gas phase dynamics is of particular interest, where solvent perturbations and many-body effects complicate the underlying physics. Unimolecular dissociation is conceptually the simplest, and a vast amount of theoretical and experimental emphasis over the past few decades has been placed on understanding these fundamental reactions (1). Yet, most of these reactions happen in a few vibrational periods of the molecule, which makes them difficult to study (10⁻¹⁴ seconds to 10⁻¹² seconds). One popular and extremely effective technique is to study a reaction by characterizing the energies of all the possible initial and final states. If the quantum states of all the reactants and products are known, the energy flow can be followed through the many degrees of freedom of the transition state.

The first experiments of this type were photofragment translational spectroscopies (2), which have been very good at elucidating the dynamics of unimolecular and bimolecular reactions, but have been hampered by a lack of rotational resolution. One solution is H atom Rydberg time-of-flight spectroscopy (3), which has achieved sub-cm⁻¹ resolution, but has been limited to a small number of molecules (mainly the dihydrides). A concerted effort of the past few decades has been the development of sensitive and specific techniques for state resolved detection of photofragments (1). Laser-induced fluorescence

has been applied to NO- (4), CO- (5), and HO- (6) containing molecules, but this requires a great deal of spectroscopic information. Resonance enhanced multi-photon ionization (REMPI) is inherently mass selective and extremely sensitive, but requires a large amount of information of the resonant states, and has been susceptible to power broadening (7). Other nonlinear laser techniques, such as coherent anti-stokes Raman spectroscopy (8), and resonance Raman spectroscopy (9) have been successful, but have been limited to a small number of molecules for similar reasons.

All of these techniques have been indirect methods of studying reaction dynamics. A more appropriate method would be to make direct spectroscopic measurements of the transition state, recently made possible by the advent of ultrafast laser technology (10). Currently, modelocked Titanium:sapphire laser systems have been proven to deliver high power pulses as short as 10 femtoseconds (11), which is sufficient to detect the primary processes of bond breaking and forming in the gas phase (12).

In the pioneering work of Zewail, femtosecond laser technology has been applied to photodissociation studies of small molecules in the gas phase (12). His femtosecond transition state spectroscopy (FTS) is a pump/probe technique, in which a molecule is excited to a dissociative electronic state by a short pump pulse, where it begins to evolve. At a later time, a second probe pulse excites the molecule from this intermediate state to a higher state. The observed signal is the fluorescence of the third state which is collected as a function of the pump/probe delay. An example of this technique was the study of sodium iodide photodissociation (13). Upon excitation in the ultraviolet, a direct dissociation was observed:

$$NaI + hv_{320 \text{ nm}} \rightarrow NaI^* \rightarrow Na + I.$$

In this case, the fluorescence from a 580 nm probe had a sharp rise and subsequent decay that was indicative of the Na---I* transition state. The fluorescence from a 589 nm had an exponential rise which was indicative of the increase of the Na product. This FTS method has been instrumental in studying elementary photodissociations, but is complicated by the

fact that three electronic states are involved: the ground state, the excited state of interest, and a higher state, which in general, is not well characterized.

A more appropriate method is to probe the dynamics via a well-characterized state. This can be done by a multi-photon transition to the ion state. The ion signal acquired as function of pump/probe delay can be an excellent method in determining all of the reactants and products of a reaction, as well as determining the time dependence of each species. Mass spectrometry has the added advantage of being extremely sensitive, and is always allowed by selection rules (14).

An example of this application is the simple diatomic dissociation of AB, as shown in figure 1.1. This has bound ground electronic states of the neutral, AB, and ion, AB⁺, and a dissociative excited neutral state, AB*. Upon excitation of a pump pulse to AB*, the molecule begins to dissociate. A subsequent interaction of the probe pulse ionizes AB* to AB⁺, or if the molecule has dissociated, ionizes A* to A⁺. The entire mass spectrum is acquired as a function of pump/probe delay, which follows AB as it dissociates on the excited surface, as shown in figure 1.2. This technique has been used only in a small number of cases (14, 15).

Usually in time-resolved mass spectrometry, the energies of the ion states are not determined. This can be determined by photoelectron spectroscopy. This measures the kinetic energy of the ejected electron of the ionized species, eKE, which is related to the ionization potential, I.P., of the ion state. For most small molecules, these states are well characterized by optical spectroscopy and traditional He I photoelectron spectroscopy. In the case of the diatomic dissociation of AB, the resulting vibrational progression at short pump/probe delay time is dominated by the time-dependent Franck-Condon overlap of the AB* state and the AB* ion state. As AB* dissociates, the observed vibrational progression should change.

Figure 1.1 AB Diatomic Dissociation

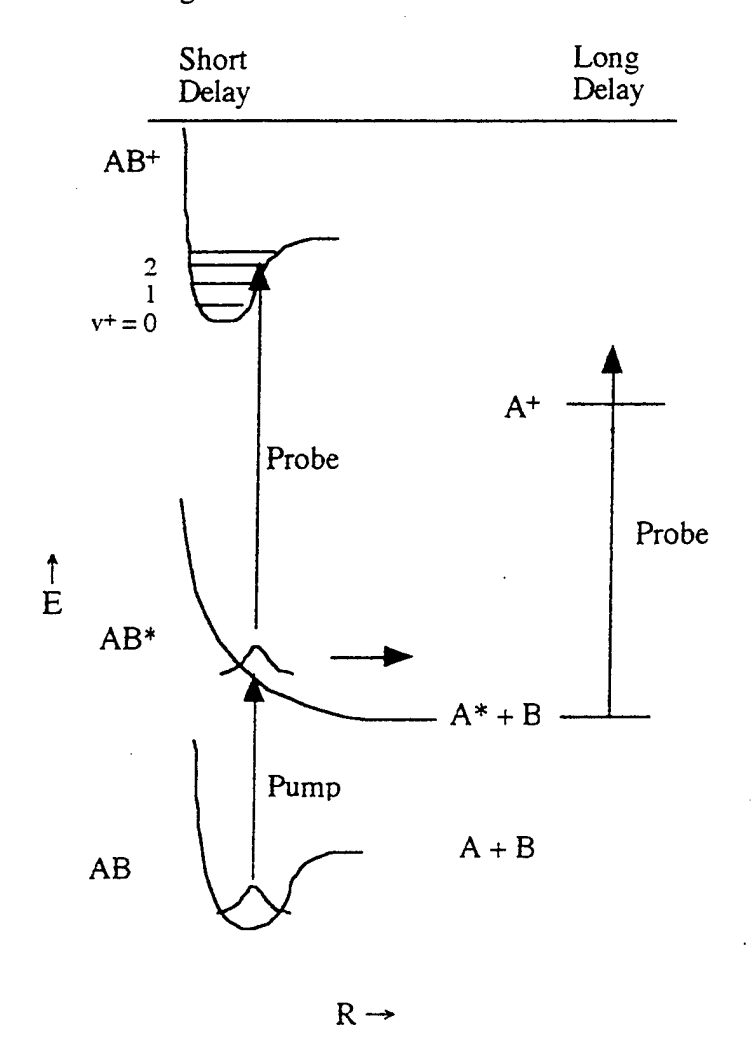


Figure 1.2 Time-resolved Mass Spectra of AB Dissociation

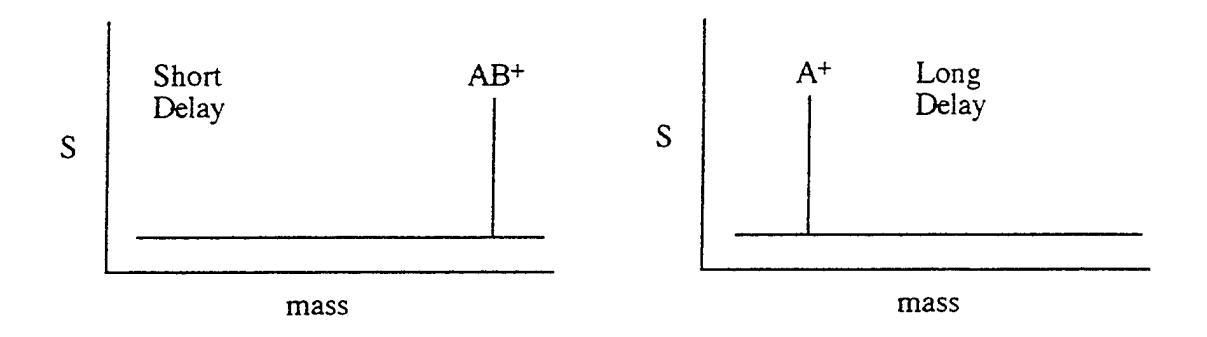
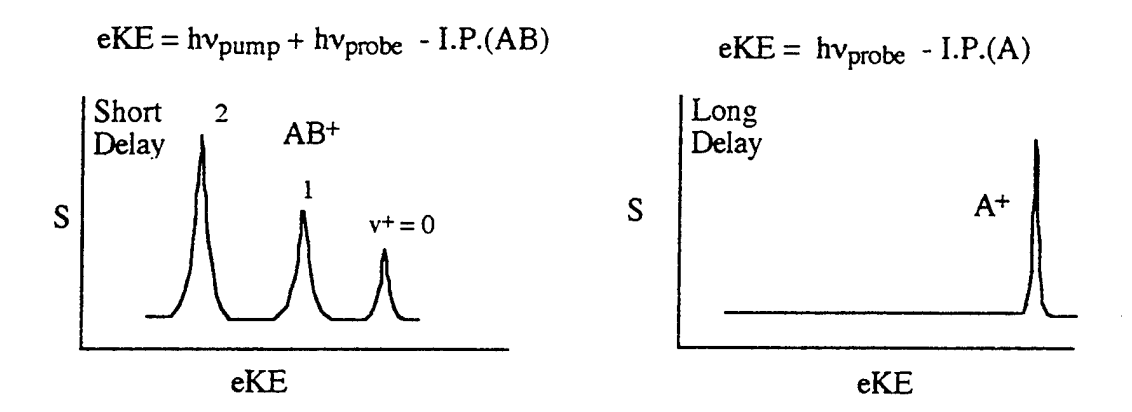


Figure 1.3 Time-resolved Photoelectron Spectra of AB Dissociation



At short pump/probe delay time, the spectrum will dominated by the spectrum of AB⁺. In this case, the probe wavelength have enough energy to reach the lowest three vibrational levels of the ion. At long delay, a single peak is expected from A* ionization. Time-resolved photoelectron spectroscopy is a new technique that has been used in a limited number of cases (14, 15.c, 16).

This work will show that the combination of these time-resolved techniques is very powerful in studying reaction dynamics. A time-resolved mass and photoelectron apparatus was designed and built in this laboratory. Even though these traditional techniques are well established, the apparatus was designed and built with a certain number of features particular to the study of femtosecond reaction dynamics. Chapter 2 is a detailed discussion of the design, construction, and calibration of the apparatus. The performance of the apparatus is demonstrated in the time-resolved photoelectron spectroscopy of nitric oxide. Chapter 3 includes the first experiment studied with the apparatus, specifically the time-resolved mass spectrometry of chlorine dioxide, an important constituent of stratospheric ozone depletion (17). Chapter 4 includes the time-resolved photoelectron spectroscopy of chlorine dioxide, which is used in conjunction with the mass experiments to gain a better understanding of its photochemistry.

Chapter 1 References

- R. Schinke, <u>Photodissociation Dynamics</u>, Cambridge, Cambridge University Press,
 1993. b. P.L. Houston, J. Phys. Chem. 100, 12757 (1996) and references therein.
 c. L. J. Butler and D. M. Neumark, J. Phys. Chem. 100, 12801 (1996) and references therein.
- G. E. Busch, J. F. Cornelius, R. T. Mahoney, R. I. Morse, D. W. Schlosser, K. R. Wilson, Rev. Sci. Instrum. 41, 1066 (1970). b. J. Solomon, J. Chem. Phys. 47, 889 (1967). c. D. R. Herschbach, Angew. Chem. Int. Ed. Engl. 26, 1221 (1987).
 d. Y. T. Lee, Science 236, 793 (1987). e. J. C. Polyani, Science 236, 680 (1987).
- 3.a M.N.R. Ashfold, L. Schnieder, and K. H. Welge, Faraday Disc. Chem. Soc. 91, 128 (1991). b. M.N.R. Ashfold, D. H. Mordaunt, and S. H. S. Wilson, Adv. in Photochem. 21, 217 (1996).
- M. Dubs, U. Bruhlman, and J. R. Huber, J. Chem. Phys. 84, 3106 (1986). b. M. P. Docker, A. Ticktin, U. Bruhlamann, and J. R. Huber, J. Chem. Soc. Faraday Trans.
 85, 1169 (1989). c. M. P. Roellig, P. L. Houston, M. Asscher, and Y. Haas, J. Chem. Phys 73, 5081 (1980). d. H. Zacharias, M. Geilhaupt, K. Meier, and K. H. Welge, J. Chem. Phys 74, 218, (1981).
- 5.a. D. J. Bamford, S. V. Filseth, M. F. Foltz, J. W. Hepburn, and C. B. Moore, J. Chem. Phys. 82, 3032 (1985). b. D. J. Nesbitt, H. Petek, M. F. Foltz, S. V. Filseth, D. J. Bamford, and C. B. Moore, J. Chem. Phys. 83, 223 (1985). c. R. L. Miller, S. H. Kable, P. L. Houston, and I. Burak, J. Chem. Phys. 96, 332 (1992). d. I. M. Waller, H. F. Davis, and J. W. Hepburn, J. Phys. Chem. 91, 506 (1987). e. I. M. Waller, J. W. Hepburn, J. Chem. Phys. 88, 6658 (1988).
- 6.a. P. Andresen, G. S. Ondrey, and B. Titze, Phys. Rev. Lett. 450, 486 (1983).
 b. P. Andresen, G. S. Ondrey, B. Titze, and E. W. Rothe, J. Chem. Phys. 80, 2548 (1984).
 c. G. Ondrey, N. van Neen, and R. Bersohn, J. Chem. Phys. 78, 3732

- (1983). d. R. Vasudev, R. N. Zare, and R. N. Dixon, J. Chem. Phys. 76, 729 (1982).
- 7.a. I. Powis and J. F. Black, J. Phys. Chem. 93, 2461, (1989). b. D. W. Chandler, M. H. M. Janssen, S. Stolte, R. N. Strickland, J. W. Thoman, Jr., and D. H. Parker, J. Phys. Chem. 94, 4839 (1990). c. R. Ogorzalek Loo, C. E. Strauss, H.-P. Haerri, G. E. Hall, I. Burak, and J. W. Hepburn, J. Chem. Soc. Faraday Trans. 285, 1185 (1989). d. J. Steadman and T. Baer, J. Chem. Phys. 91, 6113 (1989). e. G. He, Y. Yang, Y. Huang, Y. Hashimoto, and R. J. Gordon, J. Chem. Phys. 103, 5488 (1995).
- H. B. Levene, J.-C. Nieh, and J. J. Valentini, J. Chem. Phys. 87, 2583 (1987).
 J. J. Valentini, D. P. Gerrity, D. L. Phillips, J.-C. Nieh, and K. D. Tabor, J. Chem. Phys. 86, 6745 (1987).
 C. D. Debarre, M. Lefebvre, M. Pealat, and J.-P. E. Taran, J. Chem. Phys. 83, 4476 (1985).
 d. M. Zahedi, J. A. Harrison, and J. W. Nibler, J. Chem. Phys. 100, 4043 (1994).
- D. Imre, J. L. Kinsey, A. Sinha, and J. Krenos, J. Phys. Chem. 88, 3956 (1984).
 B. R. Johnson, C. Kittrell, P. B. Kelly, and J. L. Kinsey, J. Phys. Chem. 100, 7743 (1996).
- 10.a. J. Manz, and L. Woste, ed, <u>Femtosecond Chemistry</u>, Weinheim, VCH Verlagsgesellschaft, 1994. b. D. Wiersma, ed., <u>Femtosecond Reaction Dynamics</u>. Amsterdam, North-Holland, 1994.
- 11. J.-L. Martin, A. Mingus, G. A. Mourou, and A. H. Zewail, ed., <u>Ultrafast Phenomena</u>
 <u>VIII</u>, New York, Springer-Verlag, 1992.
- 12.a. A. H. Zewail, <u>Femtochemistry Ultrafast Dynamics of the Chemical Bond</u>, Singapore, World Scientific, 1994. b. A. H. Zewail, J. Phys. Chem. 100, 12701 (1996).
- 13.a. T. S. Rose, M. J. Rosker, and A. H. Zewail, J. Chem. Phys. 88, 6672 (1988).
 b. T. S. Rose, M. J. Rosker, and A. H. Zewail, J. Chem. Phys. 91, 7415 (1989).

- 14. I. Fischer, M. J. J. Vrakking, D. M. Villeneuve, and A. Stolow, Chem. Phys. 207, 331 (1996).
- M. Dantus, M. H. M. Janssen, A. H. Zewail, Chem. Phys. Lett. 181, 281 (1991).
 S. A. Trushia, W. Fuss, T. Schikarskirt, W. E. Scmid, et al, J. Chem. Phys. 106, 9386, (1997).
 c. V. Engel, T. Baumert, Ch. Meier, and G. Gerber, Z. Phys. D 28, 37 (1993).
 d. T. Baumert, J. L. Herek, and A. H. Zewail, J. Chem. Phys. 99, 4430 (1993).
 e. M. Blackwell, P. Ludowise, and Y. Chen, J. Chem. Phys. 107, 283 (1997).
- 16.a. D. R. Cyr and C. C. Hayden, J. Chem. Phys. 104, 771 (1996). b. P. Ludowise,
 M. Blackwell, and Y. Chen, Chem. Phys. Lett. 258, 530 (1996). c. B. J. Greenblatt,
 M. T. Zanni, and D. M. Neumark, Science 276, 1675 (1997).
- 17.a. S. Solomon, Nature **347**, 347, (1990). b. V. Vaida and J. D. Simon, Science **268**, 1443 (1995).

Chapter 2

Experimental Apparatus

The goal of this work was to study reaction dynamics on the femtosecond time scale. People have used a variety of pump/probe techniques, in which a femtosecond pump excites a molecule to dissociating state. A second femtosecond probe pulse samples the evolution of the transient state as a function of the delay between the pump and probe pulses. Many probe observables have been used, such as transient absorption (1), laser - induced fluorescence (2), time-resolved coherent anti-Stokes Raman spectroscopy (3), other nonlinear optical spectroscopies (4), and mass spectrometry or photoelectron spectroscopy (5). In the latter case, the probe pulses ionizes the transient species, and the positive ion or the ejected photoelectron is detected. The evolution of the ion or photoelectron signal can be related to the evolution of the molecule on the dissociating state. The advantages of mass and photoelectron spectroscopy is that the detection efficiency is very high compared to the other methods, and the lowest ion states of small molecules are well characterized.

The femtosecond photoelectron and mass spectrometer was completely designed and built in the laboratory, and has certain design features unique to the application of femtosecond photoelectron and mass spectroscopy. It consisted of three separate parts- a laser system, a time-of-flight molecular beam chamber, and a data acquisition system. The

general principles of the time-of-flight technique for mass and photoelectron spectroscopies will be introduced, as well a detailed discussion of the design and construction of each part of the experiment. The performance of the apparatus will be demonstrated in the time-resolved photoelectron spectroscopy of nitric oxide.

2.1 Time-of-flight Mass Spectrometry

Mass spectrometry is one of the most widely used and sensitive techniques of physical and analytical chemistry. There are four main types of mass spectrometry: magnetic sector, quadrapole, time-of-flight, and ion cyclotron resonance. Each type involves the separation of positive ions by magnetic and/or electric fields. There are many advantages of each type, but the time-of-flight technique is one of the simplest and cheapest (6).

The time-of-flight (t.o.f.) design chosen followed the design of Wiley and McLaren (6). Three parallel ion optic plates are used to extract and accelerate positive ions to a known kinetic energy, K.E., with kVolt potentials. The K.E. is related to the charge of each ion, q, the electric field, E, and distance of acceleration, s:

$$K.E. = qEs.$$
 [1]

The ions are accelerated to different velocities, v, depending on their masses, m:

K.E. =
$$\frac{1}{2}$$
 mv². [2]

The ions subsequently enter a field-free regime of a known distance, d, where they separate according to their masses:

K.E. =
$$\frac{1}{2} m \frac{d^2}{t^2}$$
. [3]

Typical t.o.f. designs incorporate acceleration distances of a few centimeters and field-free distances of one meter (5,6). A requirement of this design is a low pressure (10⁻⁶ Torr) to ensure a large mean free path so the ions do not interact with one another or with the walls of the chamber. The ability to distinguish different masses, otherwise known as resolution,

is dependent upon the ability to accurately measure the flight time of the ions. The resolution of this design depends on its ability to reduce the time spread due to the initial kinetic energy and space distributions. The Wiley-McLaren design achieves ion focusing from the source onto the detector by the use of two stages of acceleration. Their treatise gives a thorough explanation of determining the electric field strengths to use when optimizing the resolution of a given geometry (7).

Besides the simple design and construction, this technique has the advantage of acquiring the entire mass spectrum in one laser shot. All of the ions formed by the probe laser will be accelerated and detected. This is extremely useful in determining the products of photodissociations involving different channels. Time-of-flight mass spectrometry is particularly well suited for molecular beams because of its inherently low velocity spread and spatial spread of the beam. Typical experimental resolution of a ns laser photoionization source used in molecular beam studies are of $\frac{\Delta m}{m} = 0.001$ with a 1 meter field-free region (8). The flight tube was kept significantly shorter in this work because of other design issues of photoelectron spectroscopy.

2.2 Time-of-flight Photoelectron Spectroscopy

The information obtained in mass spectroscopy is important in determining the species involved in a chemical reaction, but does not yield any information of the internal energy of the species. This can be determined by photoelectron spectroscopy, which is another well-established molecular spectroscopic technique (9). The photoelectric effect states that kinetic energy of a photoejected electron, eKE, is related to ionization potential, I.P., of a species, and the energy of the radiation used (9):

$$eKE = hv - I.P.,$$
 [4]

where the photon energy is the product of Planck's constant, h, and the frequency of the radiation, v. If the species is an atom, the different eKE peaks correspond to the different

electronic states of the ionized atom. If the species is a molecule, the quantized energies of the photoelectrons refer to the different rotational and vibrational states of the different electronic states of the molecular ion.

Historically, there have been two main types of photoelectron energy spectrometers used (10). Retarding analyzers use electric fields to permit electrons of a specific energy to hit a detector. Acquisition of an energy spectrum involves monitoring the photocurrent as a function of retarding potential. Deflection analyzers use magnetic or electrical fields to force electrons of different kinetic energies to follow different paths to the detector, which has a narrow entrance slit. Spectra are obtained by changing the defection field to allow different energies of electrons to reach the detector. Both methods have been used widely, but each suffers from the disability of being unable to measure low kinetic energies (< 10 eV), mainly due to stray fields deflecting the electrons away from the detector. One solution is the time-of-flight technique (11). The eKE is related to the mass of an electron, m_e, and velocity, v, as in equation [5]:

$$eKE = \frac{1}{2} m_e v^2$$
. [5]

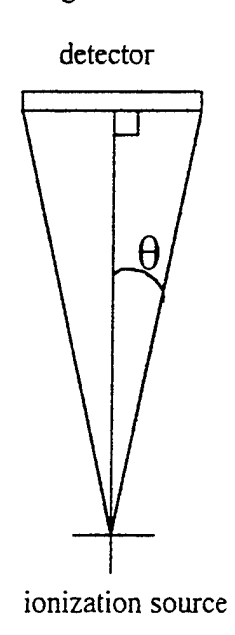
The flight time of the electron is measured across a distance, d, and is converted to a kinetic energy spectrum by equation [6]:

K.E. =
$$\frac{1}{2}$$
 m_e $\frac{d^2}{t^2}$. [6]

This is similar to the t.o.f. mass spectrometry technique, in which the ejected electrons separate according to their different velocities, but no optics are used to extract or accelerate the electrons. Therefore, stray potentials in the field-free drift region are kept to a minimum. This work has the added advantage of using the same detection scheme for the mass spectroscopy experiments, with one detector and flight tube. The ion optics inserted in the flight path for mass acquisition could be removed for the photoelectron measurements.

One of the differences in t.o.f. photoelectron and mass spectroscopies is the detection efficiency. Nearly 100% of the ions formed in the ionization process are accelerated to the detector by the ion optics. No optics are used to collect the electrons, and only those ejected into the solid angle subtended by the detector are collected. Figure 2.1 illustrates this point.

Figure 2.1



The solid angle, Ω , is defined as:

$$\Omega = 2\pi(1-\cos\theta),$$
 [7]

where θ is the half angle from the normal of the detector surface to the radius. There is an angular dependence of photoelectron emission that will dictate how many electrons will be ejected into the solid angle of the detector. This angular dependence has been well studied (12), and can be described by equation [8]:

$$\frac{d\sigma}{d\Omega} = \frac{\sigma_{\text{total}}}{4\pi} (1 + \beta P_2), \qquad [8]$$

in which do is the cross section for emission into solid angle $d\Omega$, σ_{total} is the total cross section, and P_2 is the second Legendre polynomial:

$$P_2 = \frac{1}{2} (3\cos^2 \phi - 1).$$
 [9]

 ϕ is the angle between the ionization radiation and trajectory on the emitted electron, and β is the asymmetry parameter. β is a constant for a given molecule at fixed ionization energy, and depends on the type of orbital from which the electron is ejected. β can vary from -1 to 2, but a value of 0 implies an isotropic distribution of electrons.

In the case of an isotropic distribution of electrons ejected from an unpolarized light source, the fraction of electrons collected, fr, can be reduced to:

$$fr = \frac{1 - \cos\theta}{2}.$$
 [10]

Typical experimental geometries (13) utilize flight paths varying from 50 centimeters to one meter, and detector diameters of 2.5 centimeters (12), which corresponds to a fr = .005%. This does represent the lower limit of the collection efficiency, but this is a significant issue that must be addressed. The collection efficiency can be increased in the t.o.f. technique by minimizing the flight distance, but this has the detrimental effect of reducing the resolution, which is considered in the next section.

2.21 Resolution Considerations

The fundamental limit in resolving power of the photoelectron spectrometer is determined by the uncertainty of the energy of the photoionization source. A propagation of uncertainties of equation [4] predicts that the uncertainty in the eKE, Δ eKE, is:

$$\Delta(eKE) = \Delta(h\nu) - \Delta(I.P.), \qquad [11]$$

Traditional photoelectron spectroscopy uses atomic emission lines which have very narrow linewidths, so the experimental resolution is determined by the detection method. This is not true when using femtosecond photoionization sources, because of the Time-Energy Uncertainty Principle (14) which states that the fundamental limit in the ability to measure

the product of uncertainties of energy, ΔE , and the spread in time, Δt , of an ultrashort pulse is Planck's constant, h:

$$\Delta E \Delta t \ge \frac{h}{2\pi}$$
. [12]

Substituting in the definition the energy of a photon, E, in terms of frequency, v:

$$E = hv, [13]$$

the uncertainty relation reduces to:

$$\Delta v \Delta t \ge \frac{1}{2\pi}$$
. [14]

A physical explanation of this is that many wavelengths, or modes, of a laser must be lasing in phase with one another to form a femtosecond pulse. Typical femtosecond pulses in this work were centered at 3.204 eV, with a full-width at half-height (FWHM) of .042 eV. This would result in a resolution of:

$$\frac{\Delta E}{E} = .013. \tag{15}$$

For multiple photon transitions, in general, the signal in the time domain, S(t) is (15):

$$S(t) = E_1(t) \otimes E_2(t) \otimes E_3(t) \text{ etc.},$$
 [16]

where $E_i(t)$ are the different electric fields. In the frequency domain, this is transformed to:

$$S(\omega) = E_1(\omega) \times E_2(\omega) \times E_3(\omega) \text{ etc.}, \qquad [17]$$

which means that the frequency resolution is worse in multiple transitions than in single photon transitions. The photoelectron experiments involved in this work use typically three photon transitions, so the fundamental limit of the photoelectron resolution is:

$$3\left[\frac{\Delta E}{E}\right] = .039.$$
 [18]

This is quite large when compared to typical high resolution photoelectron experiments that are able to obtain $\Delta E = .011$ at 1 eV energy (16), but this is enough to resolve the

vibrational energies of most small polyatomic ions, which are on the order of a .100 eV. Rotational energy resolution is not possible, but the main flow of energy in the reactions (i.e. the making and breaking of chemical bonds) would be witnessed in the change of vibrational energies of the ions. This fundamental limit in the resolution can be advantageous in designing the experiment. A short flight path can be used to maximize the collection efficiency of the photoelectrons without degrading the experimental resolution, which is limited by the laser. In determining the best flight path distance, calculations were performed to estimate the collection efficiency and resolution obtained of a given geometry.

The resolution of the t.o.f. spectrometer can be considered as a propagation of the uncertainties of equation [6], where Δ eKE is a function of the uncertainties in d and t:

$$\frac{\Delta(eKE)}{eKE} = \left(\left(\frac{2\Delta d}{d} \right)^2 + \left(\frac{2\Delta t}{t} \right)^2 \right)^{1/2}.$$
 [19]

The uncertainty in distance, d, is Δd and the uncertainty in time, t, is Δt . In general, an increase in d would decrease the $\frac{\Delta d}{d}$ term and increase t, which decreases the $\frac{\Delta (eKE)}{eKE}$ term, but would unfortunately decrease the solid angle subtended by the detector.

The Δd term depends on the size of the focal volume of the ionization region, estimated to be .100 mm in diameter. Another uncertainty is due to the differences of flight paths to the detector, depending on the emission angle. If an 18 mm diameter detector is used, the maximum of Δd can be determined by calculating a tangential trajectory to the detector. The uncertainties in time arise from the timing resolution of the detection electronics, which can be conservatively estimated to be 3 ns. The time of the ionization process itself is determined by the time resolution of the laser (on the order of 125 fs) which is insignificant when compared to the resolution of the detection electronics.

The resolution of the spectrometer can be calculated by assuming that the spectrometer will be used to measure energies from a few meV to 2 eV. The flight times of a 2 eV electron and a .200 eV electron traveling flight distances of 10, 15, and 20 cm were calculated using equations [5] and [6]. The fraction of electrons collected was calculated by equation [10], and the resolution was calculated by equation [19]. The results are listed in Table 2.1.

Table 2.1

	2 eV electron .200 eV	v = 8.387 m/s v = 2.652 m/s		
	flight path	10 cm	15 cm	20 cm
2 eV	$\frac{\Delta(eKE)}{eKE} =$.051	.037	.020
.200 eV	$\frac{\Delta(eKE)}{eKE} =$.017	.016	.008
fract	tion collected =	.20%	.090%	.051%

A 15 cm flight path was chosen to maximize the collection efficiency without significantly affecting the resolution. As mentioned previously, typical high resolution instruments have .50 m or 1 m flight paths that yield a Δ eKE = .011 at eKE = 1 eV energy, and have collection efficiencies of .005%. This instrument would have 3.5 times worse resolution, but would have an 18 times better collection efficiency.

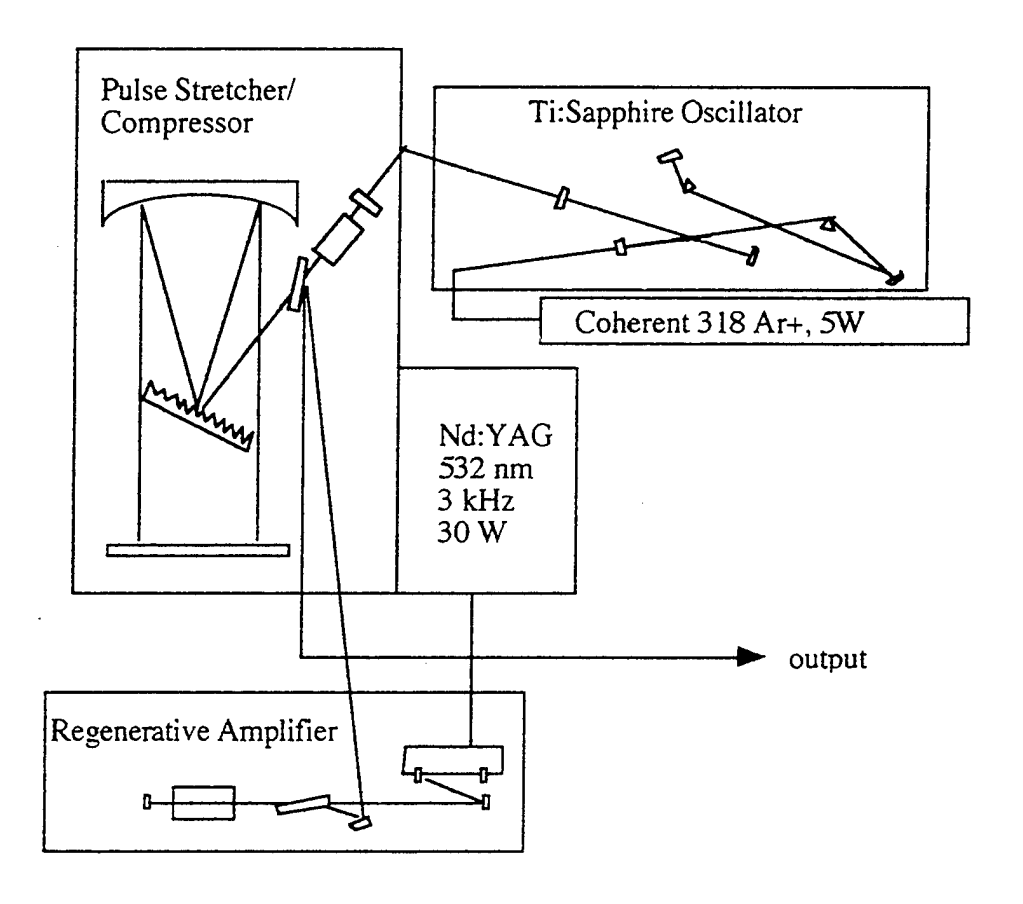
A short flight path would also be detrimental to the resolution of the mass measurements. As previously mentioned, Wiley and McLaren described a thorough procedure to determine the best electric fields to maximize resolution of a given configuration (7). Similar calculations were done to estimate the mass resolution of such a short d. In this geometry, $E_{ex} = 1500 \text{ V/cm}$, and $E_{ac} = 800 \text{ V/cm}$, would be appropriate to

achieve a mass resolution $\frac{\Delta m}{m}$ = .0067. This is more than five times worse than can be obtained by modern mass t.o.f. configurations, but it is enough to distinguish the masses of the small molecules studied in this work (less than 100 amu).

2.3 Femtosecond laser system

The ability to study reaction dynamics in the femtosecond regime requires an expensive and elaborate laser system that has very specific design features. A femtosecond Titanium:sapphire oscillator and chirped pulse amplification scheme were chosen because of their proven ability to generate sub-100 fs pulses in the near millijoule pulse energy regime. A schematic of the complete system is shown in figure 2.2. Chirped pulse amplification involves a pulse stretcher, Nd:YAG pumped regenerative amplifier, and pulse compressor. The oscillator, pulse stretcher, Nd:YAG pumped regenerative amplifier, and pulse compressor were built in the laboratory, based on the work of L. Hunziker (17). Each component will be discussed in detail.

Figure 2.2 Femtosecond Laser System



2.31 Femtosecond Oscillator

The home-built oscillator is a modelocked Titanium:sapphire laser following the design of Asaki and Huang (18), and a schematic is listed in figure 2.3. All lines of a Coherent 318 Argon Ion Laser pump a 150 cm cavity containing a 4 mm long Titanium:sapphire crystal. Fluorescence is collected by two 10 cm focal length (f.l.) concave mirrors. One arm of the laser contains a 10% transmittant output coupler, and the other arm contains two BK-7 60 degree-apex prisms, a folding mirror, a razor blade aperture, and a 2.5% transmittant end mirror. Stable TEM₀₀ continuous output of 250 mW at approximately 4 W pump power is obtained. This design is used for modelocking because it is "self-modelocking," due to the optical Kerr effect in the gain medium causing a higher gain to be achieved in the modelocked mode rather than in the continuous mode.

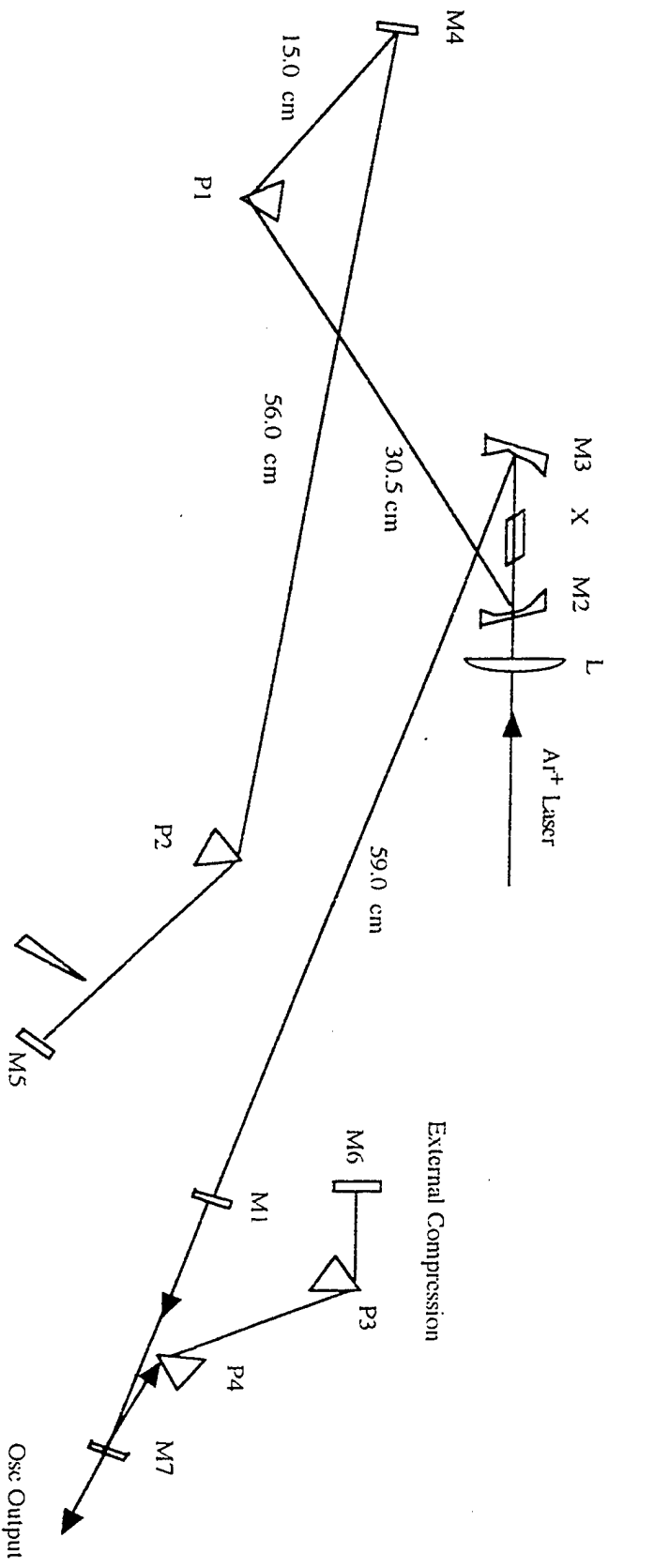


Figure 2.3 Femtosecond Titanium:sapphire Oscillator

M1: 10% Transmittant Output Coupler for 810 nm (CVI)
M2, M3: 10 cm f.l. spherical mirrors, HR at 800 nm, HT 488-514 nm (CVI)

X: 4.75 mm height x 8 mm wide Ti:Sapphire Crystal .015% doped, Brewster angle surfaces (Union Carbide)

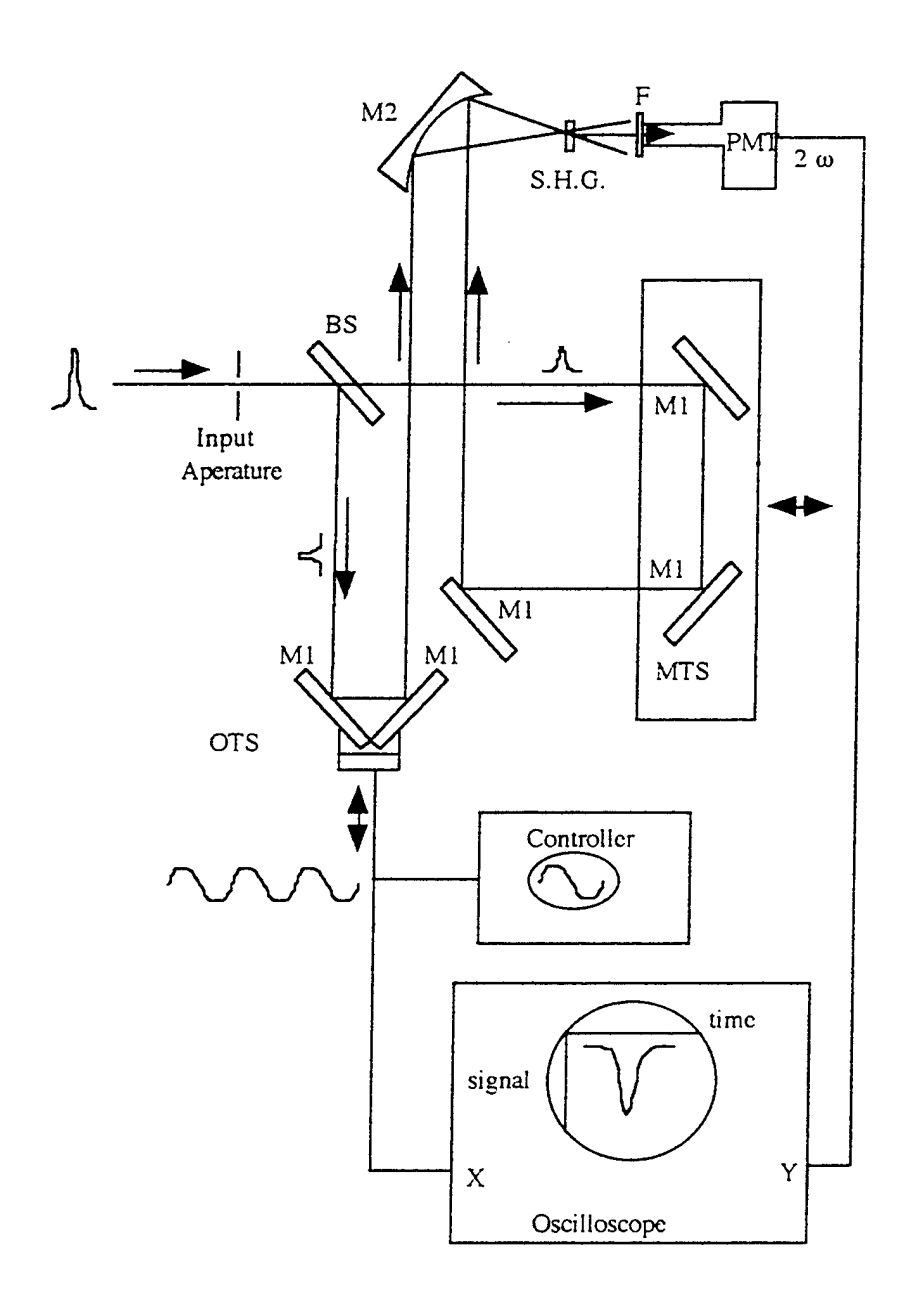
Razor

M4, M5, M5, M7: flat HR at 800 nm (CVI) P1, P2, P3, P4: fused silca prisms, apex 69.06 degrees (R. Matthews Optics Works) L: 12.5 cm f.l. plano-convex lens (Newport Corp.)

Upon start up, lasing begins in a continuous mode, but the modelocking can be initiated by knocking the output coupler or one of the prisms, which "pops" the laser into the modelocked mode. Stable modelocked operation is subsequently achieved by optimizing the output power via adjusting the end mirror. Stable sub-50 femtosecond (fs) pulses at 80 MHz repetition rate with an average power of 250 mW is obtained, and can be optimized to less than 30 fs by optimizing the external pulse compression two prisms and a retroreflector (19). The wavelength is centered at 800 nm, which is near the gain maximum of the Titanium:sapphire gain medium. The laser can be tuned to as far as 740 nm by inserting the razor aperture into the dispersed beam before the end mirror. Stable output of 30 fs pulses with an average output of 220 mW can be obtained by optimizing the prism pair compression at this wavelength.

The measurements of the pulse widths are done by a home-built continuous autocorrelator, designed on the design of Weber (20). A schematic of the device is shown in figure 2.4. The input beam is split into two pieces by a 50/50 beam splitter. The transmitted beam travels through a fixed-delay retroreflector, then reflected another 90 degrees towards a concave mirror, which focuses the beam into a KDP nonlinear doubling crystal optimized for second harmonic generation (21). The reflected beam from the beam splitter is sent to a second retroreflector that is mounted on the cone of a 4 inch diameter audio speaker, which is driven by a 15 hertz sine wave produced from a home-built driver circuit. The retroreflected beam is sent to the concave mirror and crossed with the beam from the static delay arm in the doubling crystal. Each beam has frequency doubled component (2ω) that is collinear with each input arm, but are blocked by an aperture in front of a photomultiplier tube detector. The second harmonic beam generated from the summation of the input beams of the crystal is the only beam allowed to reach the detector. A short-pass filter is used to suppress any scattered fundamental light hitting the detector. The signal is sent to an oscilloscope which is set in the x-y mode.

Figure 2.4 Continuous Autocorrelator



BS: 50% Beam Splitter, Edmund Scientific

M1: IR-enhanced Ag flat mirror, JML

M2: 2" c.c. Au mirror, Edmund Scientific SHG: KDP type I nonlinear crystal, .100 mm thick, CSK

OTS: Oscillating Translation Stage, 4" speaker, Radio Shack MTS: Manual Translation Stage, Newport

F: Short-pass color filter, Corning 4-54

PMT: Photomultiplier tube, RCA IP-28, -1000 V

The x-wave input is the driver signal of the speaker, and the y-wave is the detector signal. Thus, as the speaker is translated, the entire autocorrelation signal is detected at the oscilloscope. The autocorrelation trace is Gaussian in shape, and is calibrated by translating the micrometer on the fixed delay arm, and measuring the distance the trace moves on the oscilloscope display. Deconvolution of the autocorrelation width leads to the pulse widths of approximately 30 fs (22).

The advantages of this design is that the trace is acquired in real-time, and is background free; only the UV output of the doubling crystal formed by summation of the two input beams is detected. The autocorrelator can be easily changed for different wavelengths by optimizing the phase matching angle of the KDP crystal. This instrument is a convenient monitor of the performance of the oscillator, as it provides a real-time monitor of the laser output.

The output of the oscillator is an 80 MHz pulse train with an average power of 250 mW, which corresponds to a single pulse energy of 3 nJ/pulse. This is too weak of a power required for the experiment, so an appropriate amplification system is needed. Three different schemes are traditionally used: a high repetition rate system (250 kHz), with a low energy per pulse (1 µJ/pulse), a low repetition rate (30 Hz), with a high energy/pulse (1 mJ), or an intermediate repetition rate (2 kHz), with an intermediate energy (500 µJ/pulse). High peak powers were needed for nonlinear generation of the pump and probe pulses, as well as in the multi-photon processes needed to photoionize the molecules of interest. Yet, a high repetition rate was desirable from the point of view of photoelectron spectroscopy, where the expected signal level necessitates particle counting. This is based on the fact that less than one electron is detected for every shot, and hundreds of thousands of laser shots are needed to acquire a statistically valid energy spectrum. Thus, the intermediate amplification scheme was chosen, utilizing a Nd:YAG pumped regenerative amplifier.

The intracavity power of these amplifiers tends to be high, and if a fs pulse is directly injected into the cavity, the peak power would exceed the damage threshold of the optical components in a matter of a few round trips. This has been solved by the use of Chirped Pulse Amplification (23), in which the fs pulse is first "stretched" in time to approximately 500 ps before it is injected into the amplifier. This reduces the peak pulse power by a factor of 10000, so amplification can be done safely. After the amplification is completed, a pulse compressor is used to reduce the pulse widths to less than 100 fs, which can subsequently be used for the experiment.

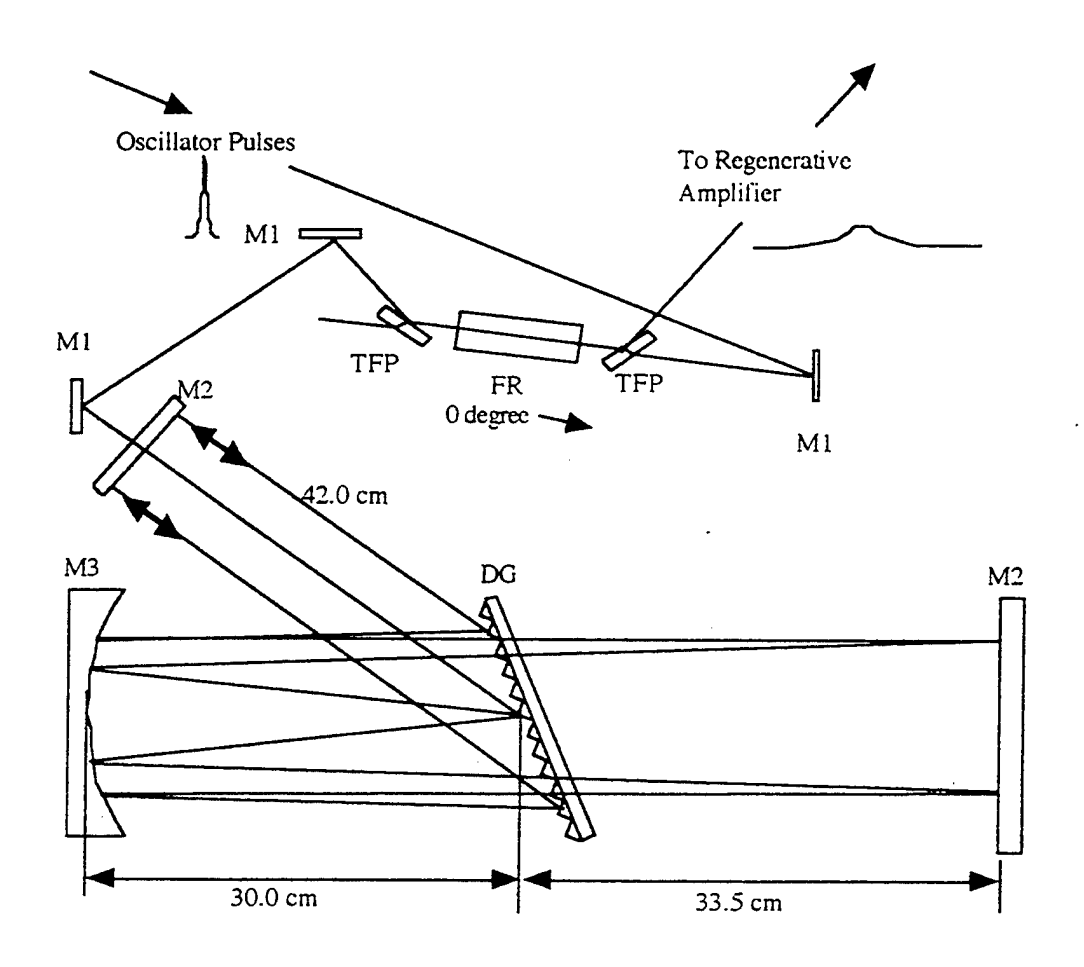
2.32 Stretcher

The pulse stretcher followed the design of Martinez (23), with a few modifications by Hunziker (17), and is shown in figures 2.5a and 2.5b. These figures show the pulse stretcher from a top view and side view for clarity. The use of a 1x telescope in a matched grating pair induces a positive chirp (frequency gradient across the duration of the pulse), via positive group dispersion that stretches the pulse envelope in time. A polarization switching technique is used to ensure injection of the stretched pulses to the amplifier. This involves a Faraday Rotator and a pair of thin-film polarizers (t.f.p.). The t.f.p.'s, mounted at Brewster's angle, reflect vertically polarized light, and transmit horizontally polarized light. A horizontally polarized pulse from the oscillator is transmitted through the first t.f.p., and then forward through the Isolator. The pulses are switched to vertical polarization, are reflected off of the second t.f.p., and are sent into the stretcher.

In the stretcher, the pulse is diffracted off of a 1200 grooves/mm grating. The output is focused by a gold coated parabolic mirror, retroreflected by a flat gold mirror, which is then reflected off of the concave mirror and grating a second time. The output hits a second pass mirror near the input point, and retraces its path once more. The second pass output is directed backwards through the Faraday Isolator.

Figure 2.5a Pulse Stretcher and Polarization Switcher

Top View



TFP: Thin Film Polarizer, 800 nm, CSK

FR; Faraday Rotator, Electro-Optics Technology

DG: 1200 grooves/mm Au coated diffraction grating, blazed at 750 nm, Milton-Roy

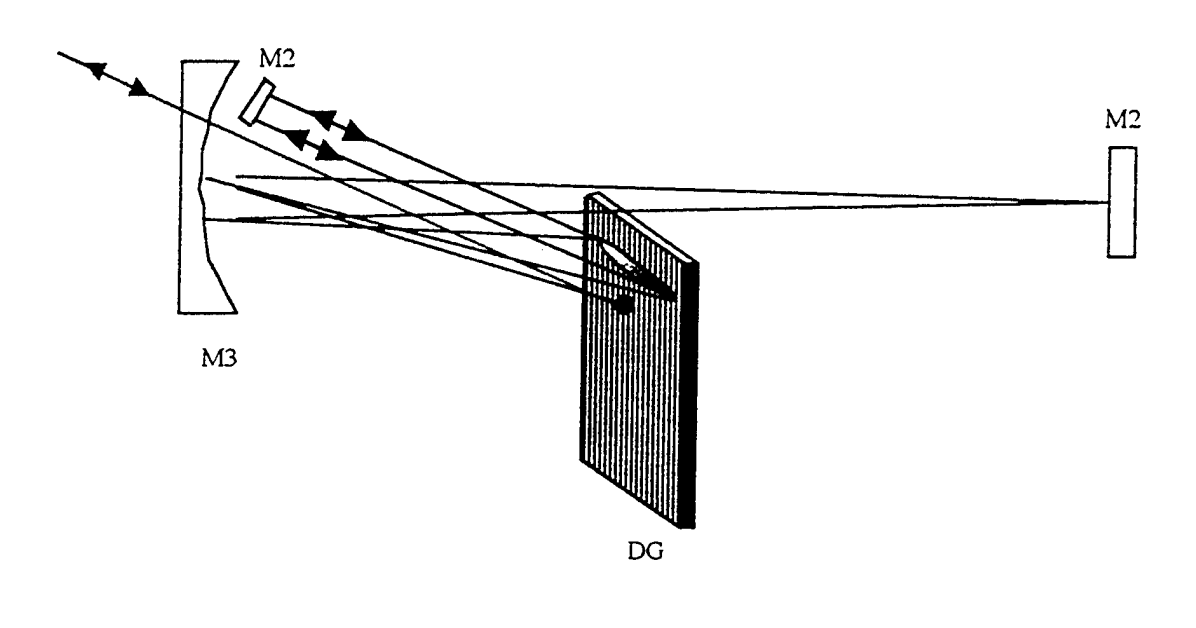
M1: IR-enhanced Ag flat mirror, JML

M2: Au coated flat mirror, Edmund Scientific

M3: 4" dia, 25" c.c. Au coated parabolic mirror, Edmund Scientific

Figure 2.5b Pulse Stretcher

Side View



---- input and output

DG: 1200 grooves/mm Au coated diffraction grating, blazed at 750 nm, Milton-Roy

M2: Au coated flat mirror, Edmund Scientific

M3: 4" dia, 25" c.c. Au coated parabolic mirror, Edmund Scientific

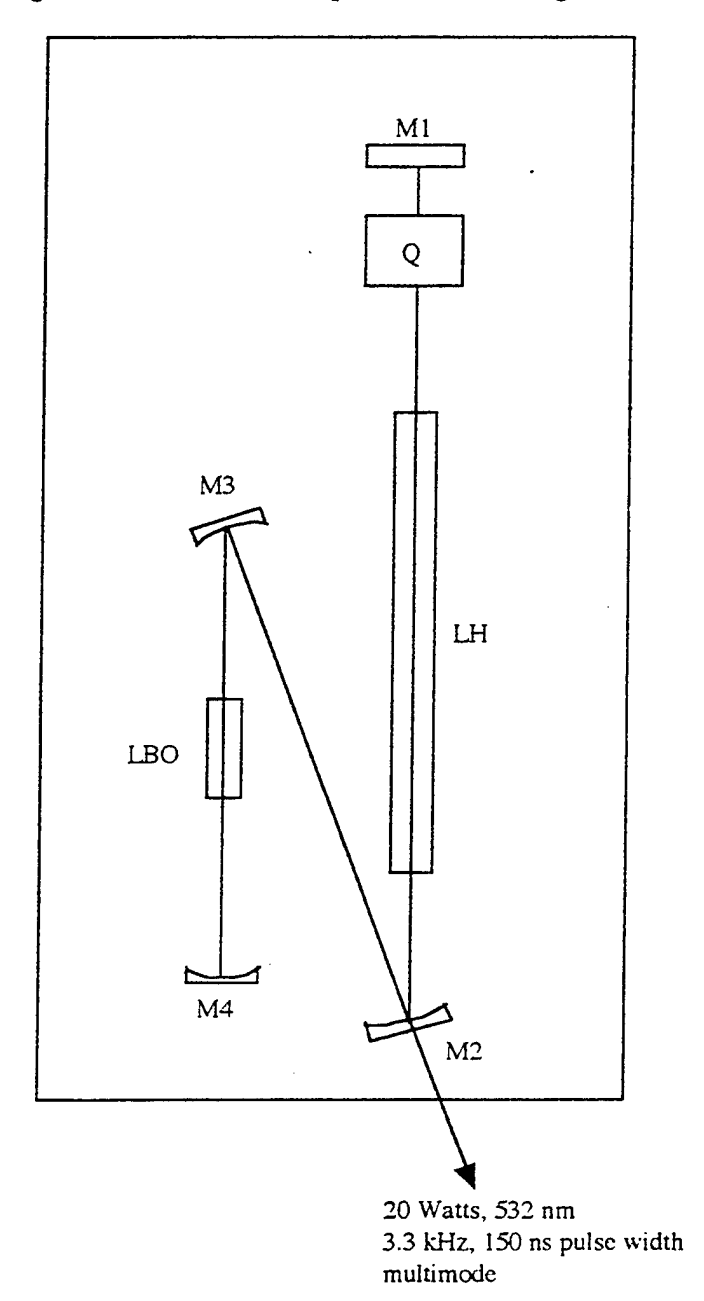
The pulse is reflected off of the second t.f.p. and through the Isolator O degree direction, which does not change the vertical polarization. Upon hitting the first t.f.p., is reflected to the regenerative amplifier. The main difference between this design and the one of Martinez, et al., is the use of a retroreflector and a single grating, as opposed to a matched grating pair.

2.33 kHz Regenerative Amplifier

A Nd:YAG laser was constructed to pump the regenerative amplifier, which is based on the design of Hunziker, and is shown in figure 2.6a. Briefly, a Spectron Laser commercial laser head is placed in a z-cavity configuration containing an LBO type II frequency doubling crystal and an acousto-optical Q-switch. This type of intra-cavity design has been known to be unstable, but this was minimized by imaging the fluorescence of the Nd:YAG rod onto the face of the front surface of the LBO crystal. The output is approximately 20 Watts, and a variable repetition rate of 3 to 3.5 kHz.

The home-built regenerative amplifier is based upon the design of Hunziker (17), and is shown in Figure 2.6b. Both sides of a 25 mm long Ti:sapphire crystal is pumped by the output of the Nd:YAG laser. The z-cavity configuration was done to optimize space, and a 3 mm diameter is inserted to emphasize the TEM₀₀ mode of the cavity. High damage threshold optics (1 TW/cm) are used for the cavity mirrors. A thin film polarizer and Pockels Cell are used to ensure lasing of the seed pulse from the oscillator only. The timing diagram for the pulse switching is also shown in figure 2.6b. Briefly, the normally high voltage (3 kVolts) is switched to low when a seed pulse is injected. The pulse is trapped between the end mirror, M1, and the Pockels cell, and the pulse begins to be amplified. Saturation occurs after approximately 15 round trips, and the pulse is dumped out by switching the voltage back on in the Pockels cell, which ejects the pulse out with a vertical polarization.

Figure 2.6a Nd: YAG Pump Laser for the Regenerative Amplifier



LH: Spectron Laser Head

Q: Q-Switch, Crystal Technology

M1: 1064 nm flat high reflector

M2: 50 cm c.c. 532 nm HT, 1064 HR

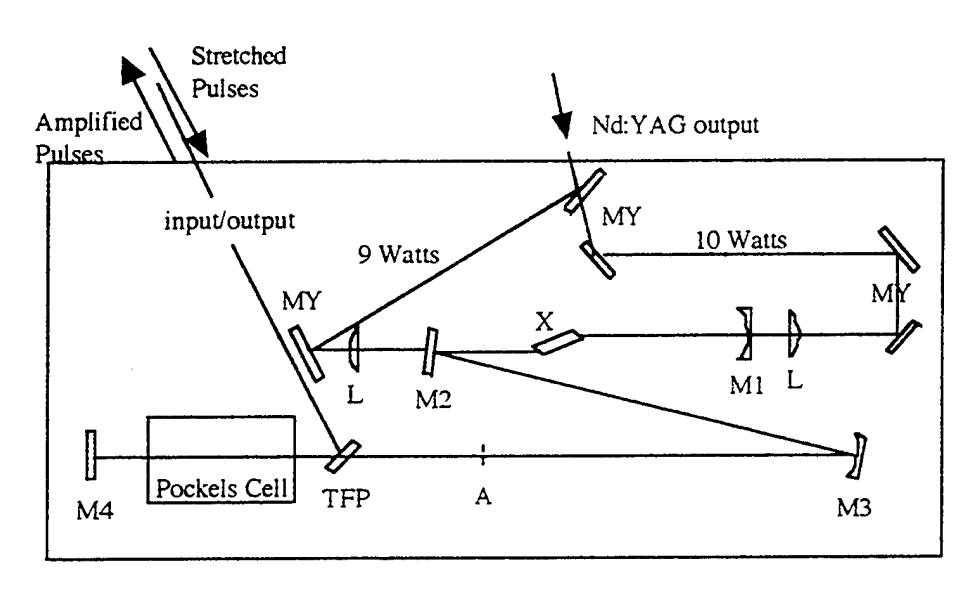
M3: 20 cm c.c. 532 nm, 1064 nm HR

M4: 10 cm 532 nm, 1064 nm HR

LBO: LBO type II 2ω crystal, 3x3x5 mm, CSK

All optics supplied by Alpine Research Optics unless otherwise specified

Figure 2.6b Regenerative Amplifier



X: 25 mm Ti:sapphire crystal, .1% doping, Brewster Angle Surfaces, Union Carbide

MY: 532 nm HR

M1: 50 cm c.c. 780 nm HR, 532 nm HT

M2: 780 nm flat HR M3: 100 cm c.c. 780 nm HR

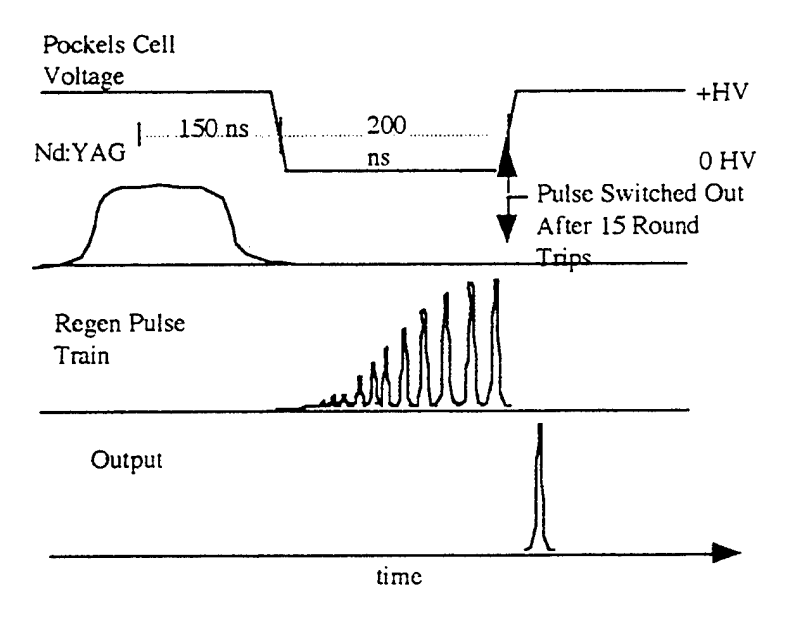
M4: 400 cm c.c. 780 nm HR

TFP: thin film polarizer, CSK

A: 3 mm dia. aperture L: 12.5 cm fl fused silica lens

All optics supplied by Alpine Research Optics unless otherwise specified





The alignment of the cavity is adjusted by inserting a $\lambda/4$ plate into the beam path, allowing cw lasing to happen when there was no voltage supplied to the Pockels cell. Typical continuous output is 2.5 watts average power of approximately 150 ns pulses. The output of the amplified fs pulse is approximately 2 Watts average power. The output is sent to the Faraday Rotator a third time to be switched into the pulse compressor.

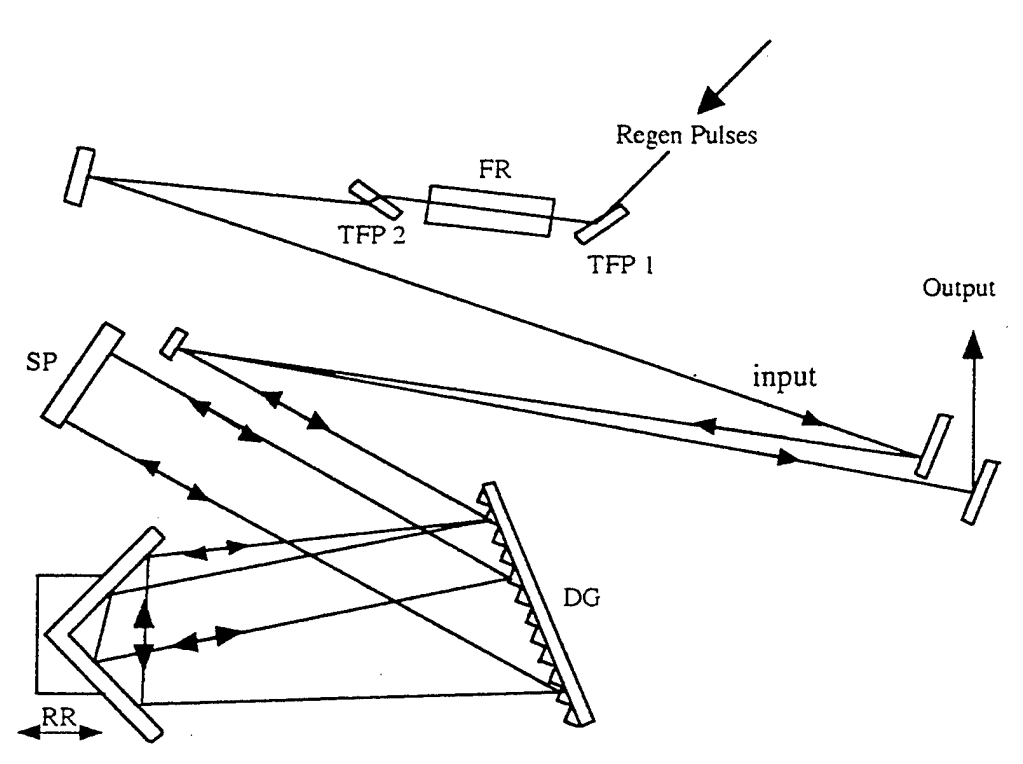
The pulse is reflected by the input t.f.p. of the Isolator, switched to a horizontal polarization, and transmitted through the second t.f.p., and injected to the pulse compressor. In this configuration, only stretched pulses are injected to the amplifier, and only stretched, amplified pulses are injected to the compressor.

2.34 Compressor

The compressor uses the same grating as the stretcher to compress the amplified pulse. This is done in a similar manner to that of the stretcher, except of the absence of the 1x telescope, which results in a negative dispersion that compresses the pulse in time (23). A schematic of the pulse compressor is shown in figure 2.7a and 2.7b. The input beam is directed to a lower portion of the grating, is retroreflected off of two 90 degree gold-coated mirrors, hits the grating a second time, and is sent to a second pass mirror. The second pass mirror retraces the path through the compressor, except is slightly misaligned to miss the input mirror, where the beam is reflected out by an output mirror. The output power is reduced to approximately 1.2 Watts, mainly due to the higher orders of dispersion off of the grating, but the pulse width has been reduced from 500 ps to less than 100 fs. The optical design allows easy compression, by adjusting the distance of the retroreflector and grating angle. A few minutes of adjustment is needed to optimize a pulse to approximately 50 fs, which is less than a factor of two greater than the oscillator pulses of 30 fs. A portion of the output pulse is sent to the continuous autocorrelator (section 2.1.1), which allows a real-time feedback to optimize the compression.

Figure 2.7a Pulse Compressor

Top View:



TFP: thin film polarizers FR: Faraday Rotator DG: Milton-Roy Diffraction Grating

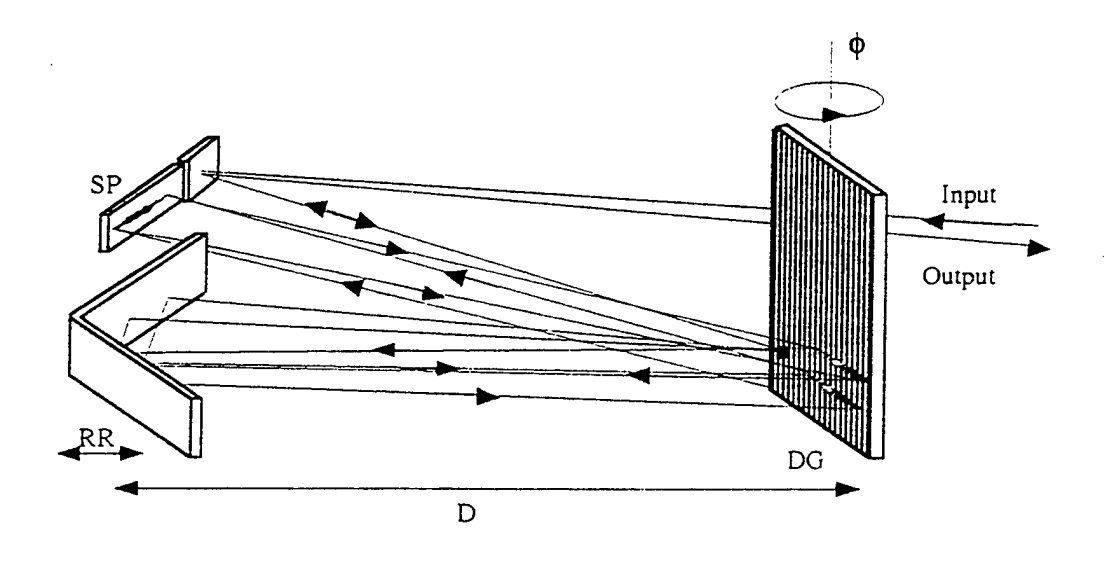
SP: Second pass flat mirror, Au-coated, Edmund Scientific

RR: 90 degree retroreflector, two Au-coated flat mirrors

Figure 2.7b Pulse Compressor

Side View:

The compression is optimized by adjusting distance, D, and grating angle, ϕ .



TFP: thin film polarizers FR: Faraday Rotator DG: Milton-Roy Diffraction Grating

SP: Second pass flat mirror, Au-coated, Edmund Scientific

 $RR\colon 90$ degree retroreflector, two Au-coated flat mirrors

2.35 Pump and Probe Generation

The high peak power of the compressed output allows efficient means of generating different wavelengths, via harmonic generation, white light generation, or by the optical parametric effect (15, 21). Second harmonic generation and sum frequency generation was chosen for the pump and probe, respectively, due to its simplicity and high power output. Tunability of the laser system is done by tuning the oscillator to the appropriate wavelength, and optimizing the pulse compression. This worked well for wavelengths ranging from 758 nm to 780 nm, which is limited by the optics in the amplifier. A different set of optics can be used to tune the laser output from 785 nm to 808 nm. The second harmonic and sum frequency output is simply optimized by tuning the wavelength-dependent phase matching angle of the crystals.

A schematic of the pump and probe generation is drawn in figure 2.8. The fs laser output is sent unfocussed into a .300 mm thick BBO crystal (CSK) optimized for second harmonic generation (21). The crystal is resistibly heated to approximately 80 degrees Celsius by a 15 ac voltage across a 1/2-Watt resistor in an aluminum block that supports the crystal. This is used to keep the hydroscopic crystal from absorbing water vapor from the atmosphere. No windows were placed over the crystal because of the dispersive effects of such materials. A dichroic mirror reflected the frequency doubled output at 385 nm, 2ω , and transmitted the fundamental frequency, ω . Fifty percent of the 2ω output is sent into a retroreflector mounted on an automated delay stage and acted as the pump. The pump beam is sent to the molecular beam chamber and is mildly focused into the interaction area of the time-of-flight chamber. Typical pump energies are about 50 μ Joules per pulse, but can be attenuated by insertion of a neutral density filter into the beam path.

ω From MI ω, 2ω Compressor BBO 1 2ω M2 BS M2 Ll BBO₂ 2ω 3ω **₩** M2 Μl М3 L2 PROBE MTS **PUMP** To t.o.f. D2 M2 chamber L3

Figure 2.8 Pump and Probe Generation

BBO 1: BBO type I frequency doubling crystal, .300 mm thick, 20 degree cut, CSK

BBO 2: BBO type I frequency tripling crystal, .300 mm thick, 50 degree cut, CSK

D1: 770 nm HT, 380 nm HR, CSK

D2: 385 nm HT, 257 nm, HR, CSK

M1: IR-enhanced Ag mirror, JML

M2: 350-500 nm HR, CSK

L1, L2, L3: 20 cm, 50 cm, 10 cm f.l. fused silica lenses, Esco

ATS: Aerotech Unidex 100 controller, Accudex 5066B delay stage

MTS: 4 cm manual delay stage, Newport

The remaining fifty percent of the 2 ω beam and the residual fundamental are noncollineary focused by another lens into a second BBO crystal that is optimized for sum frequency generation. An aperture blocks the transmitted fundamental and second harmonic beams, but the third harmonic is collected by a third lens, combined with the pump collinearly by a dichroic mirror, and is directed into the chamber. Typical probe output is $15 \,\mu$ J/pulse at $257 \,\mathrm{nm}$, but $3 \,\mu$ J/pulse are typically used to avoid high power effects (24). This is done by attenuating the fundamental and second harmonic beams separately by the use of neutral density filters. This allows separate optimization of the pump and probe beams as they enter the chamber.

The optical design emphasized easy adjustment and a minimal amount of dispersive optics to ensure a short time response of the laser system. The time response is measured by the cross correlation of the pump and probe beams performed after the exit window of the chamber, as shown in figure 2.9. The collinear beams are focused in a KDP frequency doubling crystal by a spherical mirror. The crystal is optimized to generate the fundamental frequency by difference frequency generation. The residual pump and probe beams are removed by a long pass glass filter. The signal is detected by a fast photodiode and is acquired by the data acquisition system, which will discussed in section 2.4. The cross correlation trace is obtained by stepping the delay stage while monitoring the photodiode signal. Typical traces are fit to a nonlinear least squares routine assuming a Gaussian profile. Pulse widths are deconvoluted to be approximately 125 fs full-width at half peak height (FWHM). This is limited by the pulse width of the probe. If cross correlation widths are larger than 140 fs, the probe generation is optimized until an appropriate fit is measured. The use of the thin neutral density filters in the pump and probe did not significantly lengthen the measured cross correlations.

The probe is vertically polarized to be parallel to the t.o.f. flight, which maximizes the second Legendre polynomial term of the angular distribution of the photoelectric effect

(equation [8]). The difference frequency mixing of the cross-correlation measurements requires orthogonal polarization of the input waves. Therefore, the polarization of the pump laser is fixed to be horizontal.

colinear pump and probe

M1

Figure 2.9 Cross-correlation Apparatus

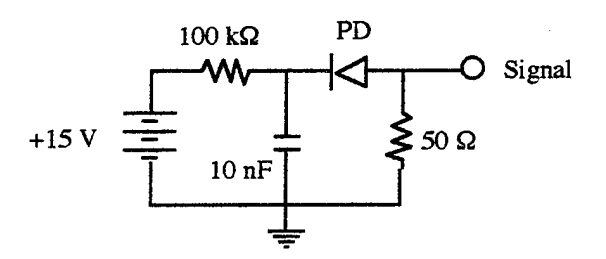
M1: UV-enhanced Ag mirror, 10 cm f.l., Edmund Scientific

KDP: .300 mm KDP crystal, CSK

F: 2-64 Color glass filter, Corning

PD: fast photodiode, Motorola MRD-510

Circuit Diagram for Fast Photodiode



2.4 Molecular Beam Apparatus

The mass and photoelectron experiments are done in a molecular beam for a number of reasons. First, the time-of-flight technique implies a high vacuum environment due to the necessity of a large mean free path of the detected species. Second, the choice of the detector is a dual microchannel plate detector, which requires an operating pressure less than 5×10^{-6} Torr. Furthermore, a molecular beam provides a very intense source of molecules, typically 1×10^{13} molecules/cm³, which is more than two orders of magnitude grater than the number density of the background pressure (3.2 $\times 10^{10}$ molecules/cm³). A discussion of the theory of the formation of a molecular beam as well as a description of the design and construction of the chamber will follow.

2.41 Free jet Expansion

The free jet expansion is a means to produce an intense, collimated source of molecules in a well defined energy state (25). A gas sample at near atmospheric pressure is expanded through a small aperture into a vacuum. If the pressure behind the aperture is increased to the point in which the mean free path of the expanding gas is smaller than the aperture size, then the random motion of the gas is converted to the kinetic energy of the molecules expanding into the vacuum. The translational temperature, defined as the spread of velocities, decreases, as the internal vibrational and rotational energies are converted to the translational energy of the bulk flow. A shockwave is formed by the interaction of the expanding gas with the background gas. The boundary, l, is defined as (25):

$$1 = .67 \, d \left(\frac{P_0}{P_b} \right)^{1/2}, \qquad [20]$$

with aperture diameter, d, in cm, pressure behind the aperture, P_0 , and pressure of the vacuum, P_b . In this regime, the gas behind the shockwave is not affected by the background. At the boundary, the collisions of the background gas destroy the collimated properties of the bulk flow, and the beam begins to become incoherent. A second aperture

can be placed downstream from the expansion orifice, but within the distance l. This selects the coldest, most intense, and most collimated part of the expanding gas. This 'skimmed beam', will retain its properties if it expands into another chamber with a low enough pressure to ensure that the mean free path of the molecules is much larger than the dimensions of the chamber. The molecules enter a 'collisionless environment' in which there are no interactions between the gas molecules with themselves or the walls of the chamber. At this point, the beam has a well formed set of conditions: the translational temperature, or spread of velocities, is very low, and only a few rotational and vibrational states are populated. Rotational temperatures of 10 K and vibrational temperatures of less than 50 K are easily obtained (25). This is quite different from a gas bulb sample, in which the translational motion is random, and the internal energy states are determined by the Boltzmann distribution.

A disadvantage of using molecular beams is the necessity of relatively large vacuum equipment to ensure adequate pumping for proper jet formation. Most of the gas used in the formation of a jet is pumped away in the source chamber, and ample forethought is needed to design an appropriate system to handle the large gas load. The important parameters in designing a molecular beam chamber are thoroughly discussed in a number of references (25), and are only briefly mentioned here. The pressure of a vacuum system, in the absence of leaks, is dependent upon the pumping speed, S, which is the volume rate of flow. The conductance, C, is the ability of an object to transmit a volume flow. Both S and C have units of liters/second. The throughput, or mass rate of flow, is denoted as Q, and is the product of pressure, P, and speed, S, and has units of Torr-liters/second:

$$Q = PS. [21]$$

Q can be estimated by the pressure drop across a pipe with a conductance C:

$$Q = (P_1 - P_2)C.$$
 [22]

The entire vacuum system can be broken down to a master equation of a single conductance leading from the source to the pump, which has a conserved throughput. The

different pieces of the chamber will have different throughputs, but the master equation determines the base pressure of the system:

$$\frac{1}{S_{\text{net}}} = \frac{1}{S_{\text{pump}}} + \frac{1}{C}.$$
 [23]

The final pressure of the system can be determined by:

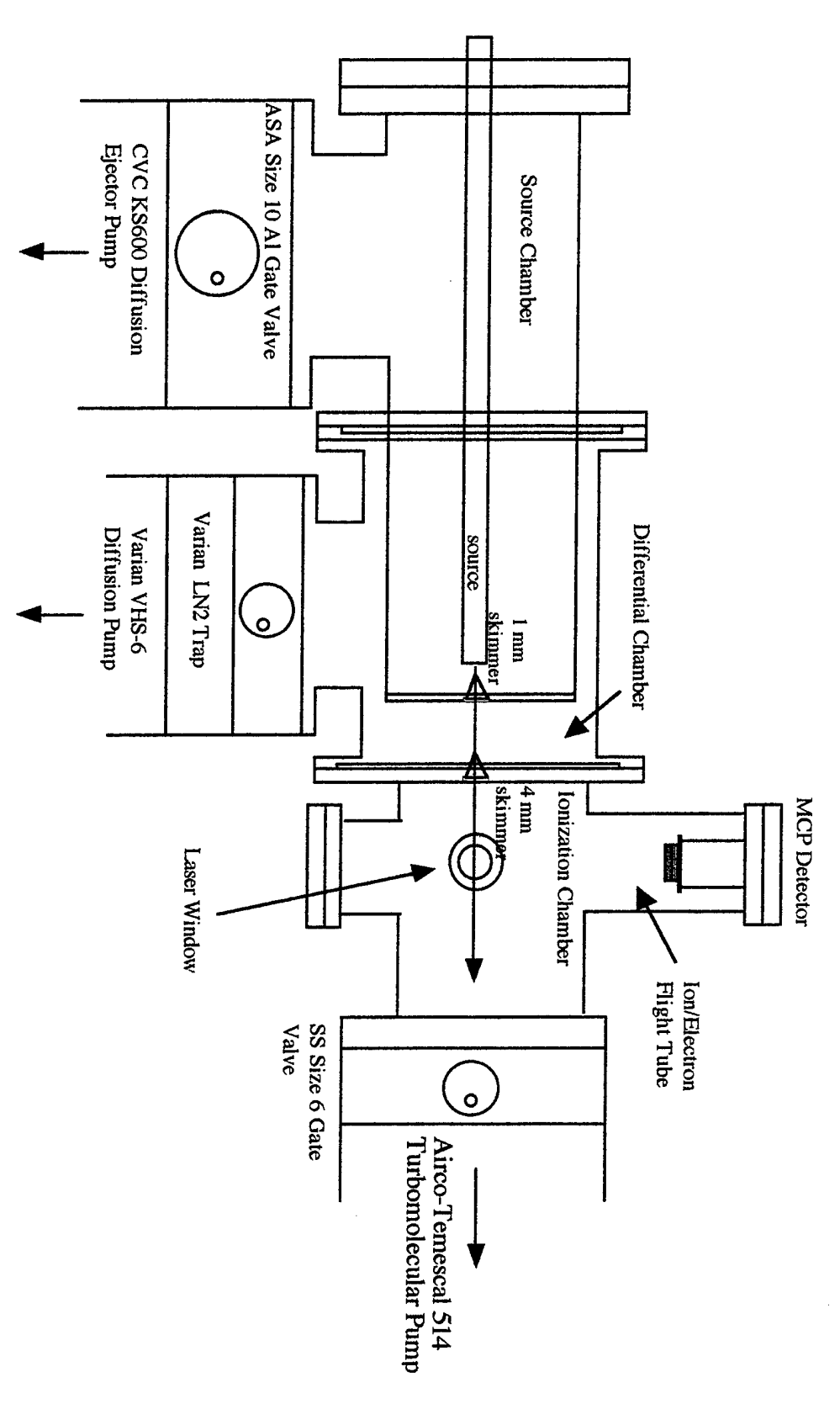
$$P = \frac{Q}{S_{net}}.$$
 [24]

Thus, large chamber diameters are needed to maximize S_{net} . If source pressures of a few atmospheres are used, shock front boundaries, I, of a few cm can be obtained by a pumping speed of a few thousand liters/second. Yet, the background pressure would be on the order of a few mTorr, which is too high for the experiment. Therefore, a differential pumping scheme (25) is used to reduce the base pressure to a safe value in the detection chamber, while forming adequate beam formation in the source chamber. This is a design in which two or three vacuum chambers are in series separated by small apertures. The apertures allow for passage of the beam into the chambers, but limits the conductance so the background pressures of the adjoining chambers can be lowered many orders of magnitude.

2.42 Molecular Beam chamber

The molecular beam chamber is shown in figure 2.10. Differential pumping with three separate chambers is sufficient to form a continuous beam and have a background pressure of $\sim 10^{-6}$ Torr. Typical operation parameters was that 1-2 atmospheres of gas is expanded through a .100 mm diameter source orifice. The expanding gas is skimmed by a 2 mm diameter skimmer 5 mm downstream from the source as it enters the differential chamber.

Figure 2.10 Molecular Beam Chamber



40

Assuming a pumping speed of 1000 l/s in the source chamber, and that the conductance is large compared to the pumping speed, the background pressure solved by equation [20] is predicted to be $3x10^{-3}$, and the shockwave front, l, to be 2 cm. The first aperture is well within the shock boundary. The beam travels approximately 5 cm before it is skimmed a second time by a 4 mm skimmer, and enters the ionization chamber. The beam travels a few more cm before being intersected by the laser beams. The total distance from source to interaction area is 18 cm, and the diameter of the beam is approximately 5 mm. The number density of a beam can be estimated as (26):

$$N(x) = N_0 \frac{d^2}{x^2},$$
 [25]

with N(x), and N_0 are the number densities at distance x from the source a and at the source, respectively, and aperture diameter, d. Under normal operating parameters, the number density of the beam in the interaction area is $7x10^{12}$ molecules/cm³, which is more than 100 times the number density of the background pressure ($7x10^{10}$ molecules/cm³). Each chamber and its pumping scheme will be discussed.

2.421 Source chamber

The source chamber contained the source inlet tube and the beam's first collimating aperture, a 2 mm diameter skimmer (Molecular Beam Dynamics). A skimmer is used to minimize the turbulence of the aperture while selecting the most intense part of the beam. The source is a 1 m long, 1" diameter stainless steel tube with a detachable end cap that contains the .100 mm diameter source aperture. The tube protrudes 63 cm into the chamber. It was supported by a homemade x-y-z translator on the end flange. The source to skimmer distance was approximately 5 mm, and was optimized for maximum signal intensity, which was well within the estimated shock front of 2 cm. The chamber material was 20 cm O.D. 304 stainless steel with viton o-ring seals. A commercial Pirani gauge (Kurt Lesker) is attached at a port to measure the pressure.

The pumping requirements for this chamber are determined by the high throughput of the continuous source. At 1 atmosphere source pressure, the throughput would be 1.1 Torr-l/s. A 1000 l/s diffusion pump would pump this to a base pressure of 10⁻⁴ Torr, which is very close to the quitting pressure of common diffusion pumps. Use of any higher backing pressures would not be safe. A kind loan of a CVC KS600 diffusion ejector pump from Prof. Saykally, an antiquated yet durable high throughput diffusion pump alleviated this problem. This was especially designed to work at high input pressures (up to 500 mTorr), and had the capability of handling a 15 Torr-1/s throughput, even though its maximum pumping speed was 700 l/s. This pump has a 2 gallon oil reserve of the hydrocarbon fluid, Convoil-20 (especially designed for high throughput diffusion pumps) and a water cooled cold cap. Initial experiments determined that a significant amount of pump fluid backstreams into the chamber that can lead to an undesirable hydrocarbon background signal. A homemade copper coil cold cap was installed in the inlet of the pump which significantly decreased this hydrocarbon background. House cooling water or liquid nitrogen could be circulated, but water does an adequate job without the constant hassle of filling the liquid nitrogen reservoir. An aluminum gate (MDC) valve installed between the chamber and pump is used to isolate the chamber from the pumping system. A large Alcatel 80 c.f.m. mechanical pump is used to back the ejector pump. A 25 foot long PVC foreline was constructed to allow the placement of the pump in a large hood isolated from the lab space. A 20 cm O.D. PVC pipe is used to maximize the conductance of such a long foreline. The estimated pumping speed of the foreline system at the outlet of the ejector pump is 75 c.f.m., which is within the proper specifications of the ejector pump. A liquid nitrogen trap is inserted between the foreline and mechanical pump to avoid the mechanical pump oil backstreaming into the ejector pump, but is not used in the OCIO experiments, due to the explosive nature of the liquefied gas (27). The base pressure of this chamber is 2x10⁻⁴ Torr, which is limited by the vapor pressure of the Convoil-20 diffusion

pump fluid. Typical operating pressure is less than $5x10^{-3}$ Torr, which is well within the safe operating pressure of the diffusion pump.

2.422 Differential chamber

The differential chamber is a 304 stainless steel chamber with Viton o-ring seals. Its dimensions along the molecular beam path were minimized to achieve the highest number density in the interaction region of the ionization chamber. Therefore, the beam travels only about 5 cm before it enters the ionization chamber. An o-ring sealed roughing valve is installed for an adequate means of venting and roughing the chambers, and an ionization gauge is used to monitor the pressure.

The pumping scheme for this chamber consists of a 1000 l/s Varian VHS-6 diffusion pump with an aluminum gate valve (Varian), and a liquid nitrogen trap, (Varian). The diffusion pump was charged with 500 ml of polyphenyl ether fluid, (Santovac-5, Monsanto), due to its excellent vacuum and electrical properties. The diffusion pump is backed by a 35 c.f.m. mechanical pump (Duo-Seal 1397), with a microsieve filter (Kurt Lesker) installed in the foreline to minimize the backstreaming of oil into the diffusion pump. The typical operation pressure in this chamber is 1×10^{-5} , which is low enough to ensure a mean free path that is larger than the size of the chamber (mean free path = 5×10^{-5} cm). The base pressure of this chamber is 5×10^{-7} Torr, which is limited by the viton o-ring seals.

2.423 Ionization chamber

The third chamber is the most critical, and received the most design considerations. To achieve the best vacuum, 304 stainless steel was used for the chamber material and Conflat type flanges with OFHC copper gaskets were used as the seals. Two views of this chamber are shown in figures 2.11a and 2.11b.

Figure 2.11a Ionization Chamber

Side View

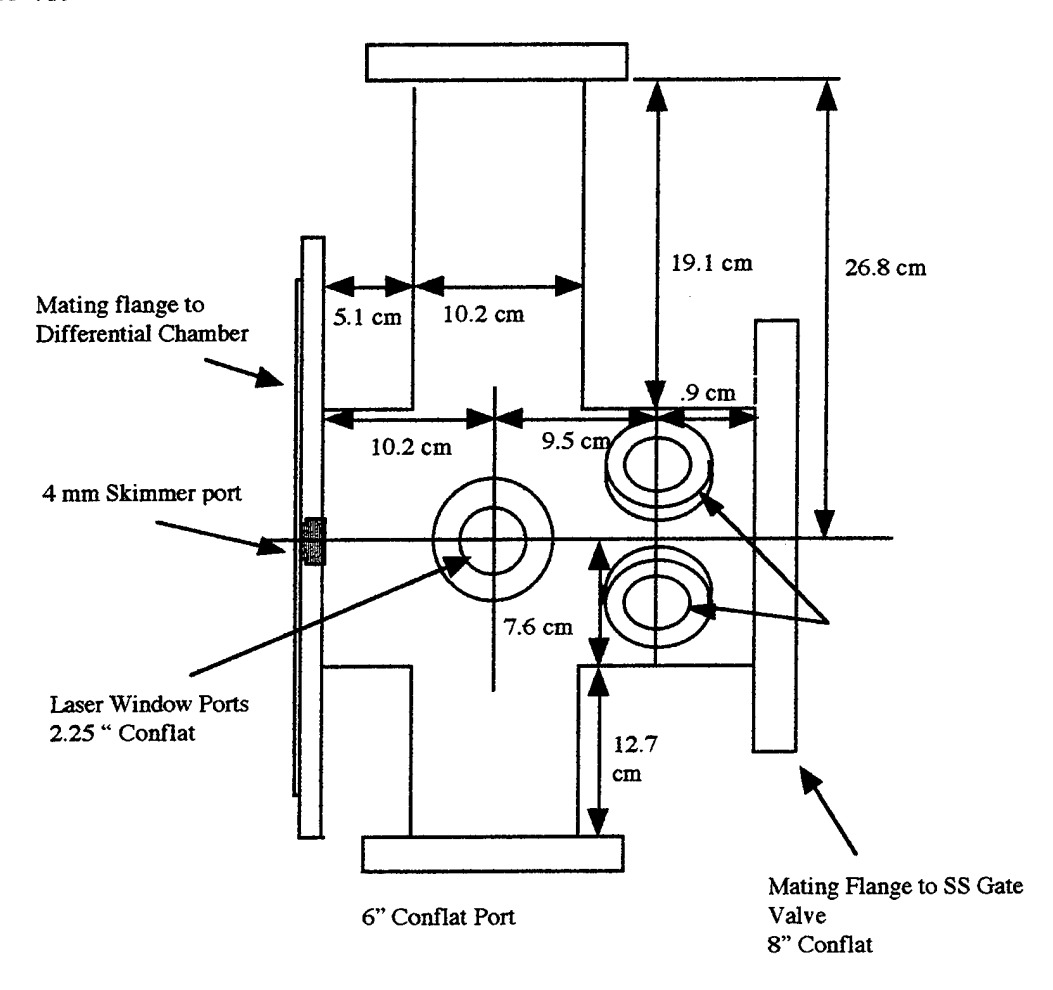
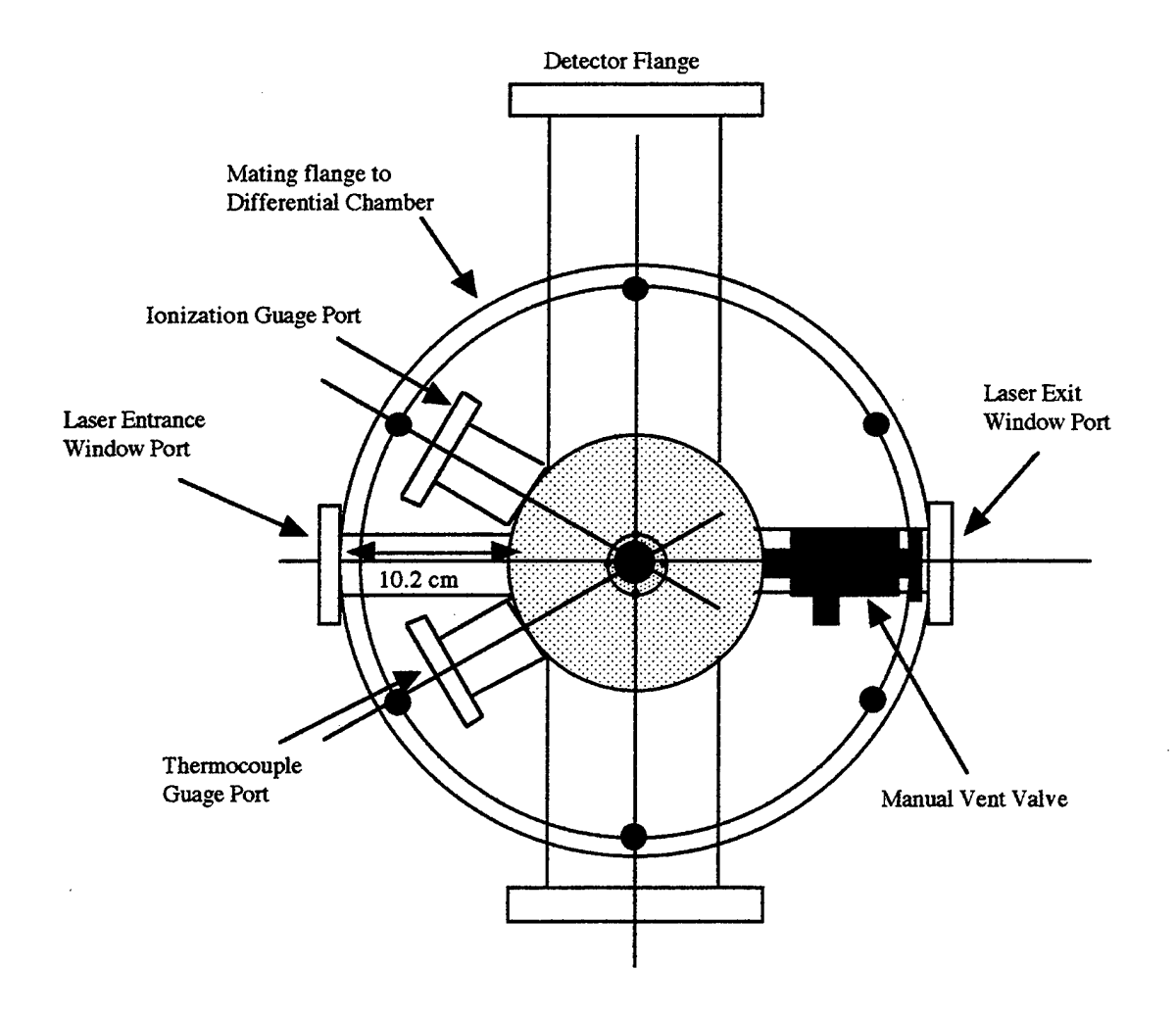


Figure 2.11 b

End View



Laser window ports and a ion/electron flight tube are mounted orthogonal to each other and to the molecular beam direction. A microchannel plate detector is mounted on a flange in the flight tube. An empty port opposite the flight tube is sealed with a blank flange. The fused silica windows are glued into place with an excellent high vacuum epoxy, Torr-Seal (Varian), which has a vapor pressure of 10⁻¹⁰ Torr. Rough and high vacuum pressures are monitored by a thermocouple (Varian 301) and ionization gauge (Granville-Phillips controller and MDC tube), respectively.

This chamber is pumped by a 500 l/s turbomolecular pump, (Airco-Temescal 514), with a metal-bonnet sealed stainless steel gate valve (Airco-Temescal). The turbomolecular pump is backed by a double stage mechanical pump (Edwards E2M-18, 12 C.F.M.) with a molecular sieve trap to keep mechanical pump oil from backstreaming into the turbo pump. Typical operating pressure is less than 3x10⁻⁶ Torr, which is well within the operating range of the detector. The base pressure of this chamber is 2x10⁻⁸ Torr. A mild vacuum bake is needed to drive off water and other species adsorbed onto the inside of the chamber. Bake-outs are done by wrapping the differential and ionization chambers with fiberglass-matted heating tape and aluminum foil. The heating tapes are powered by a number of Variacs, which were adjusted to reach an equilibrium temperature of 80 degrees C. Care is taken to keep the chambers as clean as possible, and to always vent with dry argon, instead of room air. This helped keep the base pressure low without baking after each vent.

An attempt was made to use a Varian 4 inch diffusion pump with a liquid nitrogen trap to pump an ionization chamber that was sealed with Viton O-ring instead of the Conflat type. This was found inappropriate, due to the fact that the base pressure was only $5x10^{-7}$ Torr, and a background mass spectrum showed an appreciable amount of hydrocarbons indicative of the cracking pattern of photoionized Santovac-5, the fluid used in the pump. This background was too large for the photoelectron experiments. The use of the turbo-

pump and a chamber fitted with Conflat-type seals lowered the base pressure by a factor of 25, and reduced the background to a nondetectable level.

2.424 Fight tube

The flight tube consists of many features worth noting, and is shown in figure 2.12. First is the magnetic shielding. This is constructed of two concentric tubes of a nickel alloy mu metal that extend from the detector flange to 5 cm below the interaction area. Four 1 cm diameter holes drilled into the shield allow passage of the molecular and laser beams. The shield was degaussed with a Helmholtz coil to value of 10 milligauss measured by a gauss meter. This tube was designed to attenuate the Earth's magnetic field by a factor of 10000. Otherwise, photoelectrons would exhibit an acceleration due to the Lorentz Force, **F** (28):

$$\mathbf{F} = \mathbf{q} \mathbf{v} \times \mathbf{B} \tag{26}$$

where is the initial electron velocity, q is charge, and **B** is the earth's magnetic field vector.

This acceleration would keep the electrons from hitting the detector.

The magnetic shield has a second purpose of supporting the ion optic and baffle assembly. The ion optics are only used for the mass experiments, which extract and accelerate the ion to a field free drift region. The optics consist of 304 stainless steel disks of 10 cm O.D., 9 cm I.D. covered with a 90% transmittant stainless steel mesh (12 lines/cm, 90% transmittant, Buckbee-Mears). The mesh is spot-welded around the circumference to ensure good electrical contact. The optics are parallel to one another, as shown in figure 2.13, and electrically insulated from one another by ceramic spacers of 5 mm height. The high voltage for each optic is supplied by a stainless steel piano wire connected to a MHV electrical feedthrough on the detector flange. Each wire runs down to the bottom of the tube and outside the shield to the flange. These wires are electrically insulated from each other and the shield by silica beads and tubes. A second ground ion optic is located just in front of the detector.

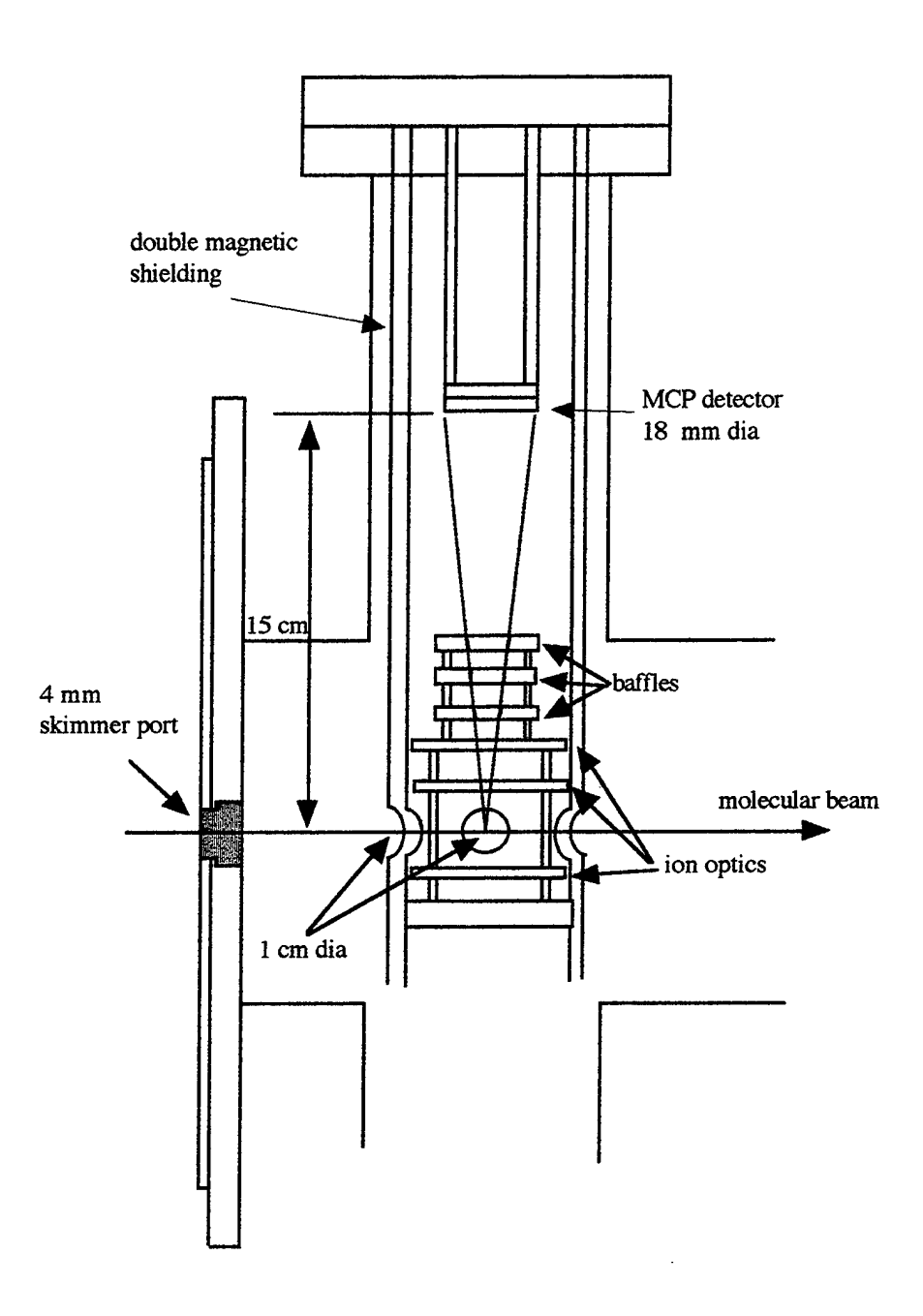
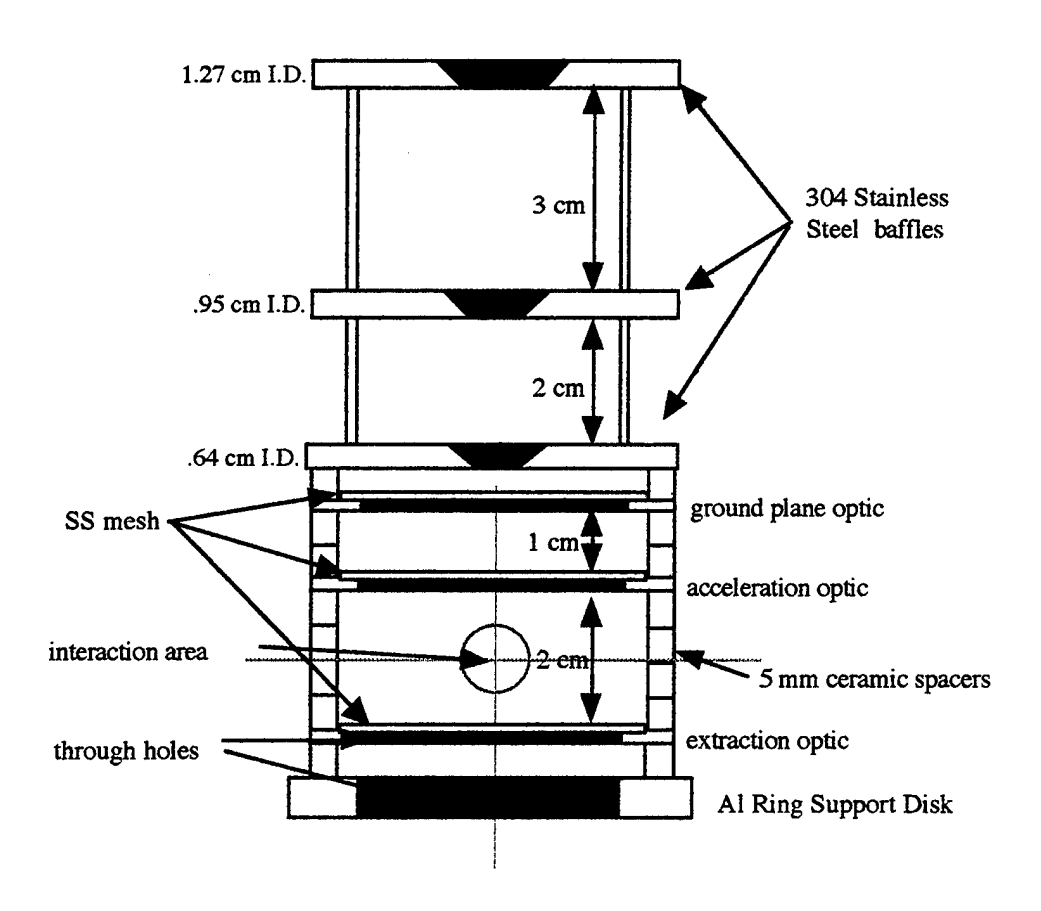
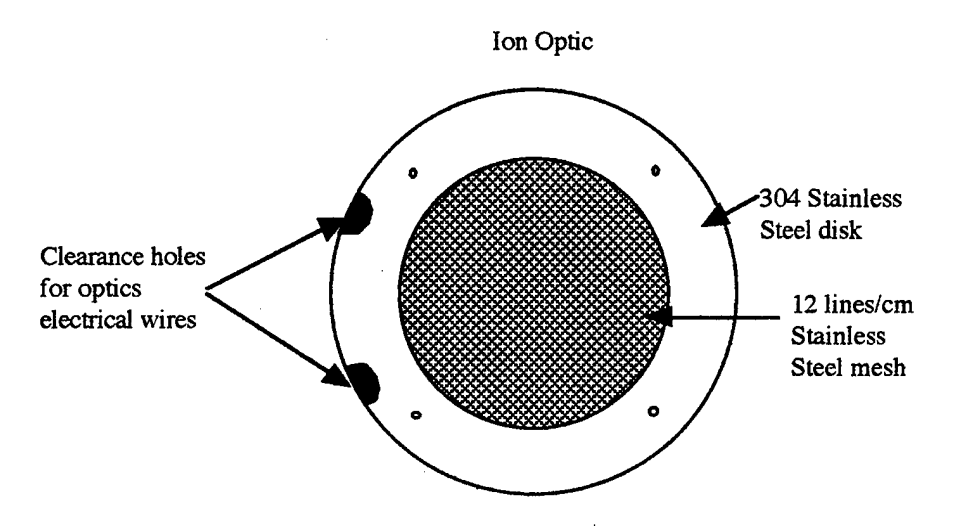


Figure 2.12 Ionization Chamber Flight Tube

Figure 2.13 Ion Optic and Baffle Assembly





The ground optics are connected to the shield, chamber, and the true ground outside of the chamber to ensure field free conditions inside the flight tube.

The voltages applied to the acceleration and extraction optics are supplied by a single dc high voltage power supply (Fluke 410B) divided by a homemade circuit shown in figure 2.14.

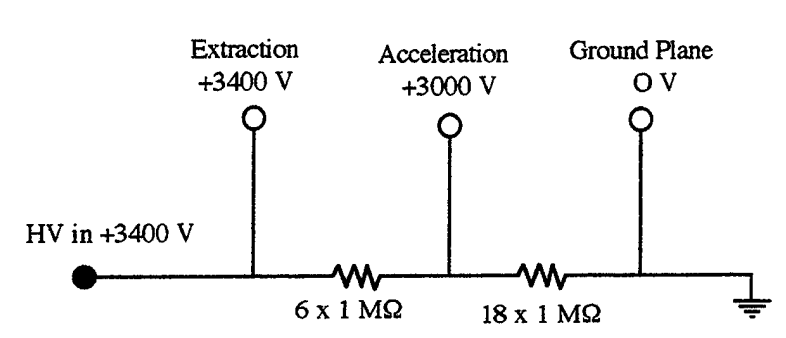


Figure 2.14 Ion Optics Divider Circuit

The divider is kept outside of vacuum for two reasons- convenience in optimizing or changing the voltages to the plates, and to alleviate outgassing problems of the divider components. A series of one $M\Omega$ resistors are used in each stage.

An increase of resolution in both the mass and photoelectron data is obtained by adding a series of baffles to the flight tube. These are three stainless steel plates, approximately .3 cm thick, with a center hole of diameters of .64 cm, .95 cm, and 1.27 cm on the plates moving toward the detector. The configuration of these optics is shown in Figure 2.13. These ensured a point source of electrons or ions that are formed within a 1 mm³ sphere in the interaction area.

Attempts were made to acquire photoelectron data with the ion optics in place, each held at a good electrical ground. Yet, there was always a stray potential of approximately 1 Volt that would accelerate the electrons, and this potential had a tendency to drift over time. Reliable data could only be taken without the ion optics in place. Therefore all the reported photoelectron data has the optics removed and the baffles in place. The inside of the flight tube and baffle assembly was coated with a thin layer of colloidal graphite (Aerodag-G).

This graphite removes patch potentials between the different materials which was proven to be essential in the photoelectron experiments.

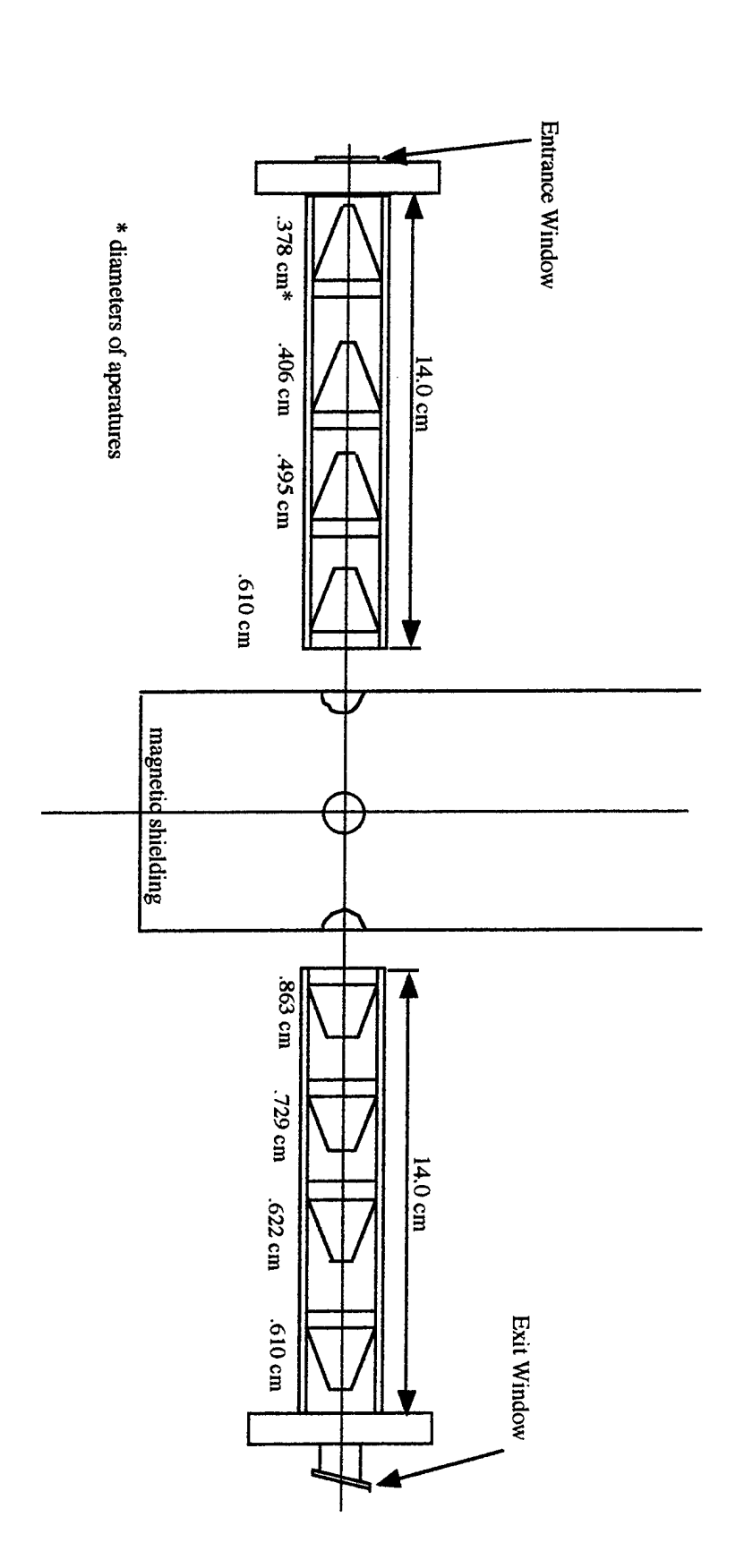
2.425 Light baffles

One problem of using the magnetic shield in the photoelectron experiment was the ejection of stray photoelectrons of the scattered probe beam. This was a significant problem, due to the fact that the energy of a single probe photon of 4.9 eV is close to the ionization potential of the metals used in the chamber and shield. The baffle assembly in the flight tube helped dramatically (a factor of 10), but the background was reduced by another factor of ten by the use of light baffles in the laser port. The schematic of the baffle assemblies are shown in figure 2.15. Fourteen cm long tubes were attached to a nipple on the laser window ports via a set screw. Each tube contained four conical baffles, of increasing diameter. The baffles were made out of brass because of its ease of machining. The inside tapers are 20 degrees, and the outside tapers are 25 degress. The input apertures were polished to a fine edge by a fine grit sand paper on the lathe. Stray reflections were minimized by the very sharp input apertures and by coating each of the baffles and the inside of the baffle tubes with colloidal graphite. Upon assembly and installation onto the chamber, it is no longer possible for the input laser beams to strike the shield. The exit window was set at a 15 degree angle from an orthogonal orientation of the laser beam path to avoid back reflections of the exiting laser beams from being sent back towards the shield.

2.426 Detector

A detector was designed and constructed that could be used to detect ions or photoelectrons. Microchannel plates were chosen because of their durability, fast time response, and versatility. These are thin plates, approximately 1/2 mm thick, of thousands of glass capillaries fused together.

Figure 2.13 Light Baffle Assemblies



A kVolt potential is held across the input and output face of the plate. An input particle of at least a few hundred eV kinetic energy strikes the wall of a capillary which emits a shower of electrons that are accelerated down the capillaries. Amplification occurs as the electrons strike the capillary walls many more times, which causes more electrons to be emitted. The cascading electrons strike an anode, where the signal can be obtained. Two microchannel plates in series have a gain of about 10⁷, which is sufficient for ion and electron detection in this application. Two matched Galileo microchannel plates, mounted in a Chevron configuration (opposite bias angles to ensure a high gain), 18 mm diameter, are used. The assembly is on a platform inside of the flight tube whose height could be adjusted to change the length of the field free region, but is set to 15 cm. As discussed in section 2.0.2, this allowed for the maximum collection efficiency of photoelectrons without sacrificing resolution. The expected photoelectron resolution is $\frac{\Delta(eKE)}{eKE} = .039$, which is limited by the laser, while maintaining a mass resolution of $\frac{\Delta m}{m}$ = .0067 which was sufficient for the size of molecules of interest in this work ($\frac{\Delta m}{m}$ = .0067 corresponds Δm =1 amu at m = 150 amu).

A configuration of the detector assembly is shown in figure 2.16a. The detector ground optic ensured that the drift region was field free. The sandwich of microchannel plates and anode are held together by springs held in place with threaded rods and nuts. Stainless steel rings placed over the input plate, in between the plates, and under the output plate supply the high voltages via piano wires connected to separate MHV feedthroughs on the detector flange. Ceramic spacers insulated the stainless steel rings from each other and the anode. The signal is a decoupled voltage measured from a 1 nF capacitor connected to the anode. The capacitor is placed inside the chamber to minimize the distance between the anode and capacitor which helped reduced ringing of single detector pulses. The capacitor is coated with Torr-seal vacuum epoxy to reduce the outgassing of the capacitor materials.

Figure 2.16a Microchannel Plate Detector Assembly

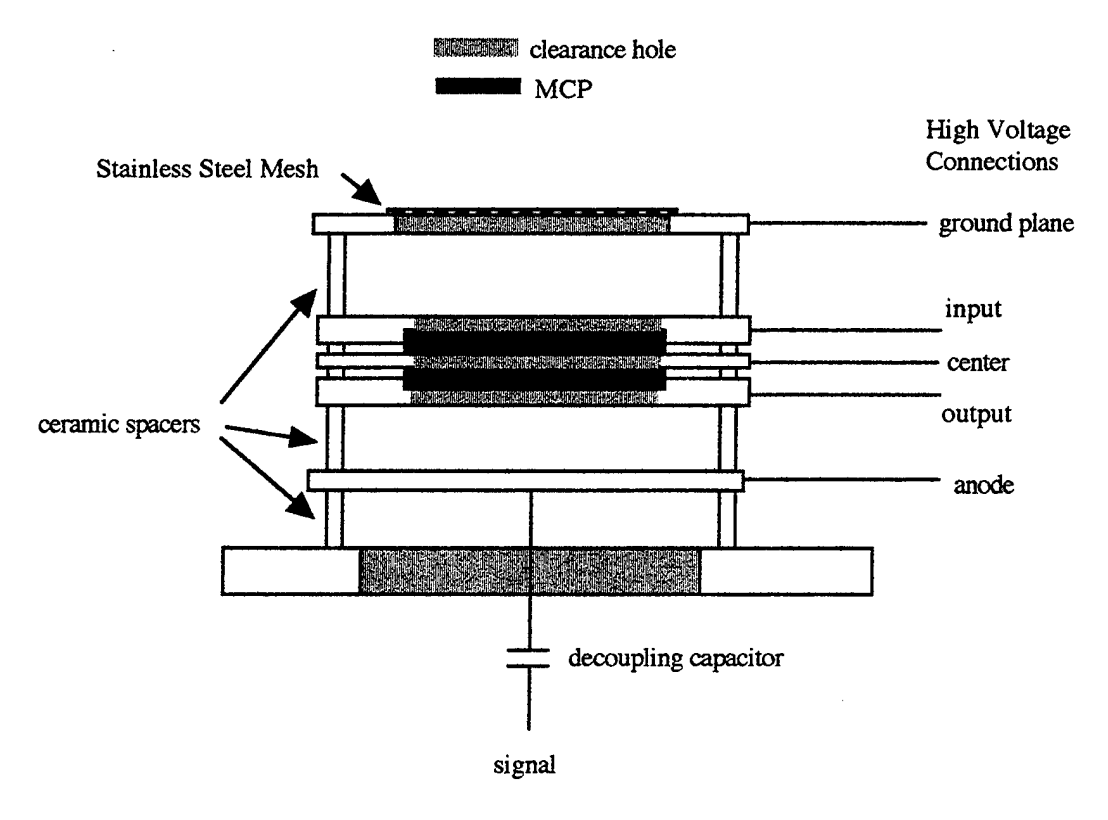
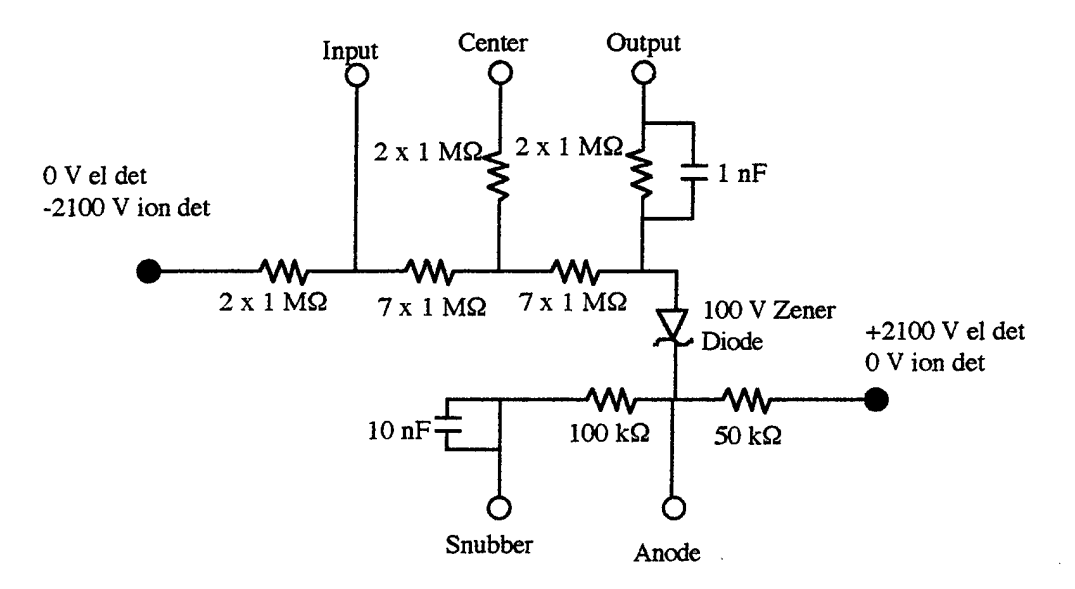


Figure 2.16b Microchannel Detector Divider Circuit



The output of a high voltage power supply (Fluke 412B) is supplied to the MHV connectors through a home made divider box. The circuit is kept outside of vacuum to minimize outgassing problems of the circuit components and for ease of maintenance. The circuit diagram is shown in figure 2.16b. The capacitors and snubber were added to minimize the amount of ringing of the MCP pulses. This is essential because the t.o.f. technique needs excellent pulse characteristics to ensure the best time resolution of the flight time. Positive ion detection is done by applying a negative polarity to the input face, and leaving the anode at ground. The ions are accelerated from the ground plane to the input, and the electrons produced in the microchannel plates are be accelerated to the output face. The Zener diode in the circuit allows a 100 Volt difference between the output face and anode, which is at ground. Photoelectron detection is done by applying a positive high voltage to the anode, and the input face held at +250 V. This accelerates the photoelectrons in the fight tube onto the input face, and accelerates the electrons produced in the microchannel plates towards the anode. Changing from positive ion to photoelectron detection is as trivial as changing the polarity of the high voltage power supply and reversing the ground at input leads in the divider circuit. For clarity, the voltage distributions used in the positive ion and electron detection is shown in figures 2.17a and 2.17b.

Figure 2.17a Detector Voltage Distribution for Positive Ion Detection

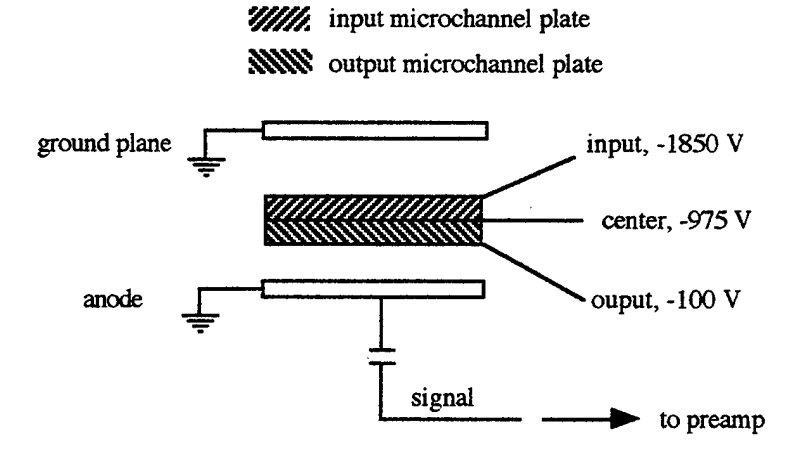
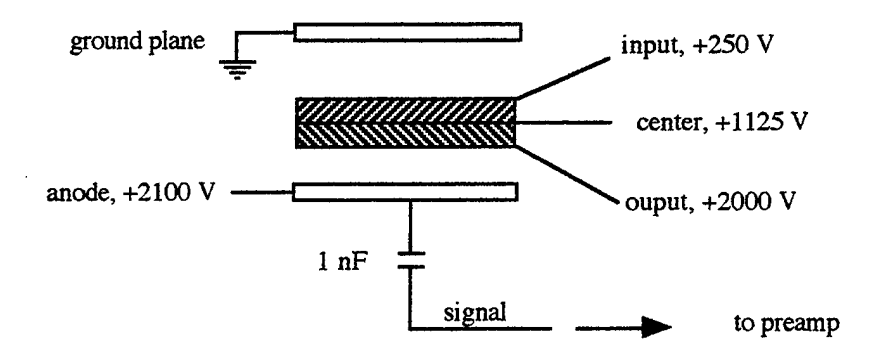


Figure 2.17b Detector Voltage Distribution for Photoelectron Detection



2.5 Data Acquisition System

A schematic of the data acquisition system is shown in figure 2.18. A synchronization circuit receives photodiode signals from the Ti:sapphire oscillator and Nd:YAG lasers. The synchronization circuit sends a trigger the Pockels cell in the regenerative amplifier. The trigger is simultaneously sent to a the Sonix STR81G 12 bit analog to digital converter (A/D) and digital signal processor (DSP), which digitizes the time-of-flight signal. This A/D board and DSP are able to digitize a 1000 point waveform with 1 ns time resolution at a repetition rate of 3.5 kHz, which is about ten times faster than most commercially available.

Sometime after the Pockels Cell switches the laser pulse out of the amplifier, the pump and probe laser pulses enter the t.o.f. chamber and ionize a sample. The ions are accelerated (or photoelectrons ejected) into the flight tube and hit the detector at a later time. The detector sends the signal to a 10x preamplifier, which is subsequently sent to the A/D board. Each mass spectrum is the voltage of an ion acquired at a certain flight time. Each photoelectron spectrum is a voltage corresponding to an electron of a certain kinetic energy arriving at the detector at a certain flight time. The data acquisition system and the automated Aerotech delay stage in the pump beam are controlled by a 66 MHz computer,

which also stores the data. The data is transferred at a later time to a 166 MHz Pentium computer for analysis.

Regen Pockels Cell

Synch Box

preamp signal

osc in YAG in

10x

Figure 2.18 Data Acquisition System

MCP: Microchannel plates signal

10x: LeCroy Fast Preamplifier, 1 ns time resolution, 10x output

Sonix A/D: Sonix STR 81G 12 bit analog-digital converter, 1 ns time resolution

DSP: Sonix digital signal processor

OSC in and YAG in: Fast photodiode signals from Ti:sapphire and Nd:YAG lasers

The main purpose of the data analysis is to convert the data from a time dependence to a mass or electron kinetic energy dependence. In both cases, the arrival time of a particle was measured, but the signal has a t² dependence, as shown in equations [3] and [6]:

$$KE = \frac{1}{2} m \frac{d^2}{t^2}.$$
 [3]

A Jacobian transformation is needed to convert the signal as function of time to a signal as function of energy (photoelectrons), or mass (29). If, for example, a signal, S, is acquired as a function of time, t, but is desired to be expressed in terms of energy, E, the factor $\frac{dt}{dE}$ must be determined:

$$\frac{dS}{dE} = \left(\frac{dS}{dt}\right) \left(\frac{dt}{dE}\right)$$
 [27]

This can be determined explicitly by rewriting equation [3]:

$$E = A t^{-2}$$
, [28]

in which the kinetic energy, E, is a function of constant A and variable t. Rearranging equation [28] and differentiating t as a function of E:

$$t \propto E^{-1/2}$$
 [29]

$$\left(\frac{\mathrm{dt}}{\mathrm{dE}}\right) \propto \mathrm{E}^{-3/2} \tag{30}$$

$$\left(\frac{dt}{dE}\right) \propto t^3$$
. [31]

Therefore, the data needs to be multiplied a factor of t³ to be converted from the time domain to the kinetic energy domain. The data analysis also included averaging of the raw scans and background subtracting, if necessary. Integrations over mass or eKE peaks would be done to present the delay scans in a more convenient format.

An optical chopper is used in some experiments to automatically subtract the pumponly or probe-only background. In this case, a Stanford Research Systems SRS540 chopper with a 32 blade wheel is placed in either the pump beam or probe beam, depending on which was to be subtracted. The chopper controller would send a frequency x 2 trigger pulse to the Nd:YAG pump laser, ensuring a synchronization of laser with the chopper. Every other laser shot, consisting of pump- only or probe only signal, would be automatically subtracted from the pump/probe signal in the data acquisition program controlling the experiment.

Two types of data acquisition programs are used, depending on the type of particles detected. The ion optics would extract and accelerate a 4 pi steradian solid angle collection, resulting in a large enough mass signal to perform a normal average over a set number of laser shots acquire a spectrum of an adequate signal/noise ratio. Typical mass data of the pump only or probe only were the average of 5 to 50 sets of scans of 10000 laser shots each. A 50 frame spectrum acquired at the repetition rate of 3.2 kHz would require only 2.5 minutes. Pump/Probe delay scans were taken by averaging 5000 or 10000 shots at a pump/probe delay, and then moving to another delay. Typically, 200 delay steps would be scanned 3 to 10 times repeatedly as a check for consistency.

A normal average cannot be used for photoelectron detection, because the signal is expected to be much smaller. In contrast to the mass data, only a small percentage of the electrons ejected are detected (section 2.0.2). A manifestation of this is that less than 1 electron per shot would be detected. If 1 electron is detected per shot, an average would result in 60 mVolts of signal (the size of a single electron peak after 10x amplification) Yet, electron is dispersed over the allowable electron kinetic energy spectrum. The great number of laser shots in which an electron is not detected at a certain energy would become buried in the noise of the baseline. A solution to this is the use discrimination and single particle counting (30), which is a way to accumulate the energy spectrum of only the laser shots that produce photoelectrons. Essentially, this removes the baseline from the digitization range. Any electron peak detected is counted as one significant event, which is added to the next significant event that eventually adds to a spectrum. A spectrum is the summation of the counts to the point that any more summation would not be statistically different from

the previous sum. In practice, an acquisition of 50 frames 32700 laser shots are sufficient, which corresponds to 8.5 minutes per photoelectron spectra. Pump/Probe delay scans are collected in the same manner as in the mass experiments, except that the same amount of averaging is done at each delay.

This has the disadvantage of not utilizing every laser shot, but a high repetition rate system can acquire enough laser shots to trace a spectrum in a matter of minutes. One must be careful to ensure that the count rate is low enough to ensure that only one electron would appear at one time in one laser shot. Experimentally this was checked by reducing the signal level (by reducing the laser power or source pressure), and observing any significant changes to the observed eKE spectrum.

Great care is taken to ensure proper discrimination of the baseline. If the discrimination is set too low, ringing from the detector pulses can be digitized, leading to secondary "false" counts. If the discrimination is set too high, too many of the pulses electron pulses are discriminated, due to the statistical distribution of the detector pulse heights, causing poor count rates. The proper discrimination level is determined by adjusting the level and observing a minimum change in the eKE spectrum taken under the same signal conditions.

2.6 Calibration of the spectrometer

The t.o.f. technique measures the flight time of a particle over a known distance.

The measured flight times, however, included the delay of the synchronization box and in the electronics used to acquire and process the signal. The time delay of the synchronization box was determined by acquiring a fast photodiode signal of a laser pulse at the exit window of the chamber. The delay time of the electronics was determined by removing the light baffles and misaligning the probe laser at the input window to cause a portion of the beam to scatter off of the shield and onto the detector. The microchannel plates are sensitive to ultraviolet light, and a scattered light peak is observed. The measured

delay of 9 ns between a photodiode trigger signal at the exit window and the microchannel plate signal corresponds to the transit time of the signal through the electronics. The raw data is corrected in the analysis programs of the 166 MHz computer.

2.61 Nd:YAG 355 nm Calibration

The true distance is very hard to determine a priori, and was determined by calibrating the spectrometer with the well-known photoelectron spectra of xenon (11.b, 31, 32) and nitric oxide (32, 33). Due to the laser bandwidth of the fs laser system, a single frequency 30 Hz Nd:YAG laser, Spectra-Physics GCR-4, at 355 nm was used. Four photons of 355 nm would ionize Xe to the first and second electronic states of Xe⁺, via a non-resonant process:

$$Xe + 4 hv_{385nm} \rightarrow Xe^{+} (^{2}P_{3/2,1/2}) + e^{-}$$

The multi-photon ionization, MPI, signal of NO would yield peaks from $v^+ = 0$ to $v^+ = 3$. The vibrational progression is expected to be different from the HeI radiation because of the autoionization of super-excited valence states populated by a 3 photon absorption:

NO (X
$$^2\Pi$$
) + 3 hv_{355nm} \rightarrow NO* \rightarrow NO⁺ (X $^1\Sigma^+_g$) +e⁻

This has been well studied at ionization wavelengths near 355 nm (33). The ionization potentials and expected eKE's are listed in Table 2.2. The fast photodiode signal of the laser beam transmitted through the exit window of the chamber was used to trigger the A/D board, which acquired the signal. The acquired signal was fit to the equation [6]:

K.E. =
$$\frac{1}{2}$$
m_e $\frac{d^2}{t^2}$ [6]

by fixing t, the corrected flight time, and floating flight distance, d, until the eKE matched the expected values for the two species. The best fit was 15.9 +/- .1 cm.

Typical spectra acquired are shown in figures 2.19a and 2.19b. Note that the signal/noise ratio of the Xe data is not especially good, due to the low repetition rate of the

30 Hz laser used. This spectrum was acquired in one hour, and since the signal/noise, S/N, ratio is related to Poisson statistics (34), which states:

$$\frac{S}{N} \propto (\text{number of events})^{1/2}$$
. [32]

The S/N can be improved by a factor of two if this spectrum is taken over four hours.

Table 2.2 Calibration Data for 355 nm PES

Ionization Potentials of Xe (31, 32)

12.130 eV
$$Xe^{+2}P_{3/2}$$

Expected eKE's with 355 nm

$$1.854 \text{ eV}$$
 $^{2}P_{3/2}$

.544 eV
$${}^{2}P_{1/2}$$
.

Ionization Potentials of NO (32, 33, 35)

$$v^{+}=1$$
 9.5544 eV

$$v^+=2$$
 9.8414 eV

Expected eKE's with 355 nm

$$v^{+}=0$$
 1.226 eV

$$v^{+}=1$$
 .937 eV

$$v^{+}=2$$
 .650 eV

$$v^{+}=3$$
 .367 eV

Figure 2.19a 355 nm Nd:YAG PES Spectrum of Xenon

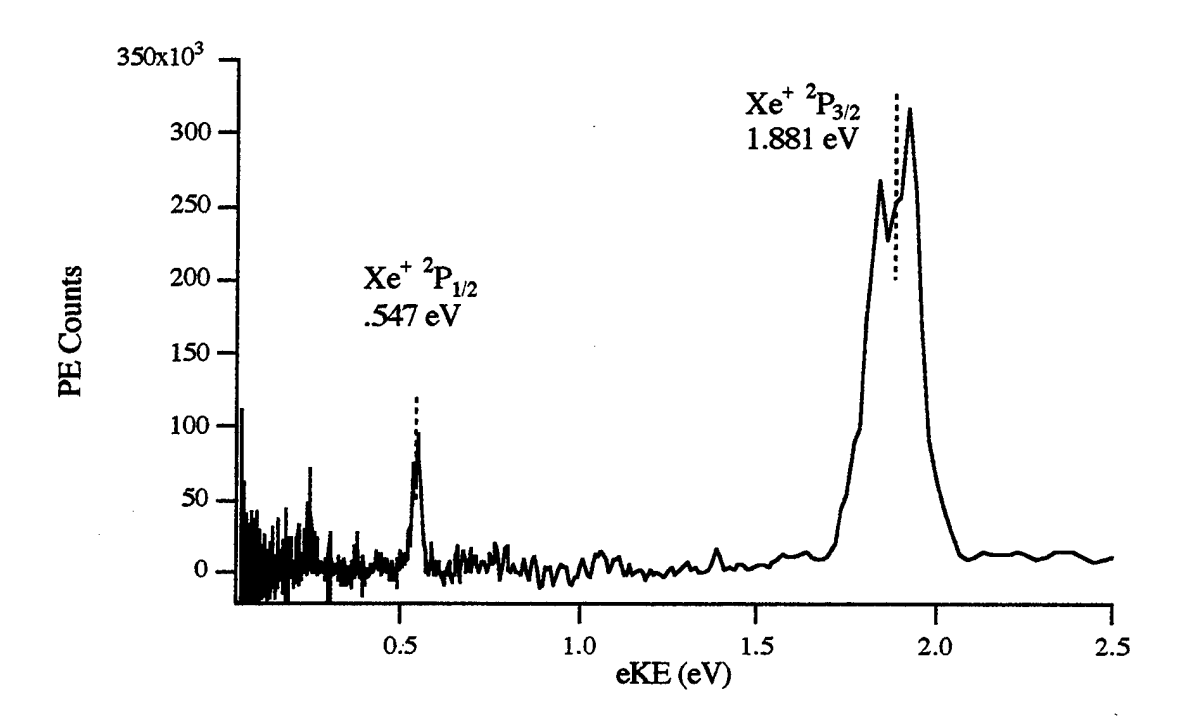
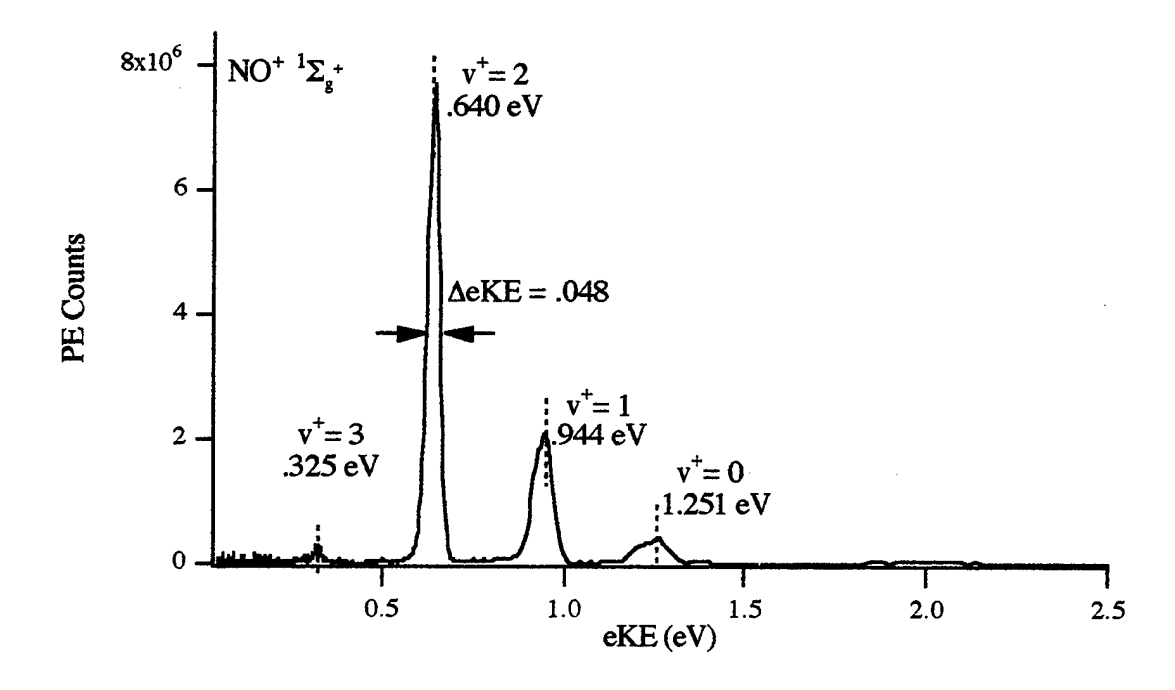


Figure 2.19b 355 nm Nd:YAG PES Spectrum on NO



The flight time of a 600 meV electron is approximately 500 ns, resulting in $\frac{\Delta t}{t}$ =.028, which becomes the dominant uncertainty. This data was useful in determining the flight distance, d. The uncertainty of d was not significant in the femtosecond data because of the resolution of the laser bandwidth. A comparison of the expected eKE values and the experimental eKE values are within an average error of 1%, which is limited by the resolution of the data.

2.7 Time-resolved Photoelectron Spectra of NO

A more appropriate example of the performance of the spectrometer can been seen in the time-resolved photoelectron spectroscopy (time-resolved PES) of nitric oxide. Nitric oxide, NO, is an extremely well-studied diatomic in which nearly all of the ground and excited states of the neutral and singly-charged ion are known (35, 36). It also has a low ionization potential (9.26 eV) which makes it useful in characterizing the spectrometer. The procedure for obtaining the time-resolved PES have been described in sections 2.3 and 2.4. Briefly, 1 atmosphere of pure NO (99%, Matheson) is expanded through the continuous .100 mm diameter source aperture into the molecular beam spectrometer. The expanding gas is skimmed twice before entering the ionization chamber where the sample interacts with the pump and probe pulses. The typical operation pressure was less than $2x10^{-6}$ Torr. Under these conditions, mass spectra have shown the contribution of (NO)₂ and larger clusters were less than 5% the size of the parent signal. All spectra were taken with the ion optics absent to ensure a field-free photoelectron drift region. The laser polarization for the probe was vertically polarized, and horizontally polarized for the pump.

A typical probe only spectrum is shown in figure 2.20. At an photoionization wavelength of 253 nm, ionization occurs by a two photon nonresonant direct ionization process:

$$NO(X^2\Pi) + 2h\nu_{probe} \rightarrow NO^+(X^1\Sigma^+) + e^-$$

At this wavelength, only the $v^+ = 0$ and $v^+ = 1$ vibrational levels can be accessed. An assignment of the data is listed in Table 2.3.

 $v^{+} = 1$ 0.251 eV $v^{+} = 0$ 0.549 eV 0.6 0.2 0.2 0.4 0.2 0.6 0.6 0.8 0.6 0.8 0.6 0.8 0.8 0.8 0.8 0.8 0.8 0.9

Figure 2.20 Probe-only PES of NO at 253 nm

Table 2.3 Assignment of Probe-only PES of NO

eKE =	$2hv_{probe}$	-	I.P.	(v_i)
-------	---------------	---	------	---------

ion vibrational state	observed eKE	expected eKE	absolute error
$v^+ = 0$	0.549 eV	0.541 eV	.008 eV
1	0.251 eV	0.251 eV	.000 eV

The observed transitions are within an 8 meV error. The difference between the two peaks (.298 eV) is very close to the determined vibrational frequency of .290 eV for the NO⁺ X $^{1}\Sigma^{+}$ state (35). The ratio of the two peaks in figure 2.20 is due to the different Franck-Condon factors between the X $^{2}\Pi$, v=0 neutral state and the $v^{+}=0$ and $v^{+}=1$ states of the ion. The observed ratio is in excellent agreement with previously published 2 photon ionization spectra near 255 nm (37).

The pump-only spectra shows dramatically different behavior because of resonances of nearby Rydberg states. By definition, a Rydberg state is an excited electronic state in which the electron is far away from an ionic core (35). Therefore, the geometry change between the Rydberg state and the ion is very small. The corresponding Franck-Condon factors will be essentially unity for the $\Delta v = 0$ transition and zero for all other transitions. This has been described as a resonance enhanced ionization process, and has been observed in a variety of Rydberg states of NO (33, 38). For example, excitation near $\lambda_{nump} = 390$ nm will access the A $^2\Sigma^+$, v = 3 state by a two photon absorption:

NO
$$(X^{2}\Pi) + 2hv_{pump} \rightarrow NO* (A^{2}\Sigma^{+}, v = 3) + 2hv_{pump} \rightarrow NO^{+} (X^{1}\Sigma^{+}, v^{+} = 3) + e^{-}$$

A competing process is autoionization, which has been known to occur in NO (33, 38, 39). In this case, a multi-photon transition excites a super-excited valence state which is above the ionization threshold. The molecule crosses from the valence state to the ion state ejecting an electron in the process. The ordinary Franck-Condon rules do not apply, and all vibrational levels accessed by the photon energy can be observed. The process can be described as:

NO
$$(X^{2}\Pi) + 4h\nu_{\text{pump}} \rightarrow NO^{**} \rightarrow (X^{1}\Sigma^{+}, v_{i}^{+}) + e^{-}$$

A typical 4 photon pump only spectrum is shown in figure 2.21, which shows a combination of the resonance-enhanced and autoionization processes. In this example, the

strong $v^+ = 3$ peak is indicative of the direct ionization process enhanced by the A $^2\Sigma^+$ $v^+ = 3$ state, and the $v^+ = 0$, 1, 2, 4, and 5 are indicative of the autoionization process. The observed spectrum is very similar to the previously published multiphoton ionization PES of NO (39).

This spectrum does show the resolution obtainable by the spectrometer. The measured full-width at half peak height (FWHM) of the $v^+ = 3$ peak is .088 eV. The corresponding photoelectron resolution $\frac{\Delta(eKE)}{eKE} = .032$, which is close to the expected value of .039 (equation [16]). The best that the observed peaks match the expected values is due to the error in the calibration, which has an average error of +/- .014 eV.

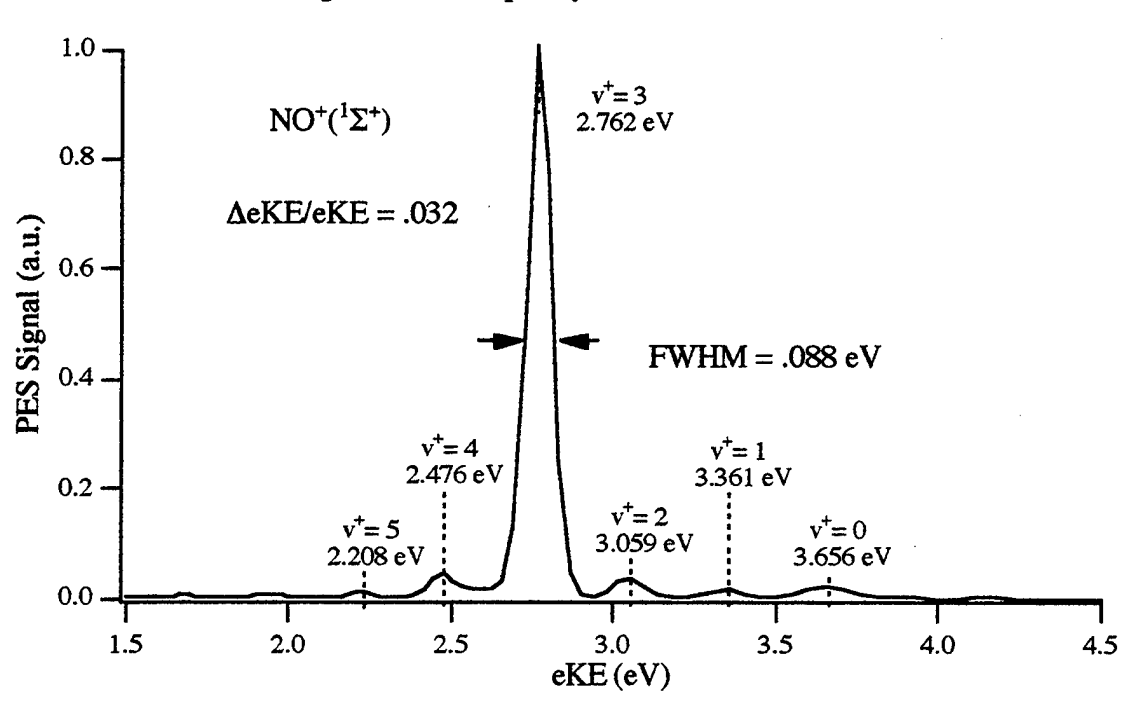


Figure 2.21 Pump-only PES of NO at 388 nm

Table 2.4 Assignment of Pump-only PES of NO

ion vibrational state	observed eKE	expected eKE	absolute error
$v^+ = 0$	3.656 eV	3.639 eV	+.017 eV
1	3.361	3.349	+.012
2	3.059	3.062	003
3	2.762	2.779	017
4	2.476	2.499	023
_			244
5	2.208	2.219	011

The Rydberg nature of the excited states of NO can be investigated by pump/probe time-resolved PES. Specifically, the pump excites a discrete vibrational level of an excited electronic by a two photon transition, which is subsequently ionized by the probe. The PES taken as a function of pump/probe delay time should be indicative of a population formed in the Rydberg state. In this case of a pump excitation near the $A^2\Sigma^+$, v=3 state, at a positive delay, one ion peak is expected from a direct ionization mechanism:

NO (X
$$^2\Pi$$
) + 2 hv_{pump} \rightarrow NO* (A $^2\Sigma^+$, v = 3) + 1 hv_{probe} \rightarrow NO $^+$ (X $^1\Sigma^+$, v = 3)

Figure 2.22a and figure 2.22b shows three different photoelectron spectra taken at different pump/probe delays. At negative delay, there is no signal. There is a large increase in the signal at zero delay, which is the point when the pump and probe pulses are superimposed in time. The $v^+=0$, 1, 2, and 3 are easily seen. At a positive delay, one dominant $v^+=3$ peak is observed with a small amount of the $v^+=2$, 4, and 5 peaks. An electron integrated scan is shown in figure 2.22c. The transient nature of the $v^+=1$ state is evident, while there is a gradual rise of the long-lived $v^+=3$ state. The time width of the transient peaks

are approximately the same as the cross-correlation of the pump and probe pulses measured experimentally, as described in section 2.2.

Figure 2.22a Time-resolved PES of NO at $\lambda_{pump} = 390 \text{ nm}$

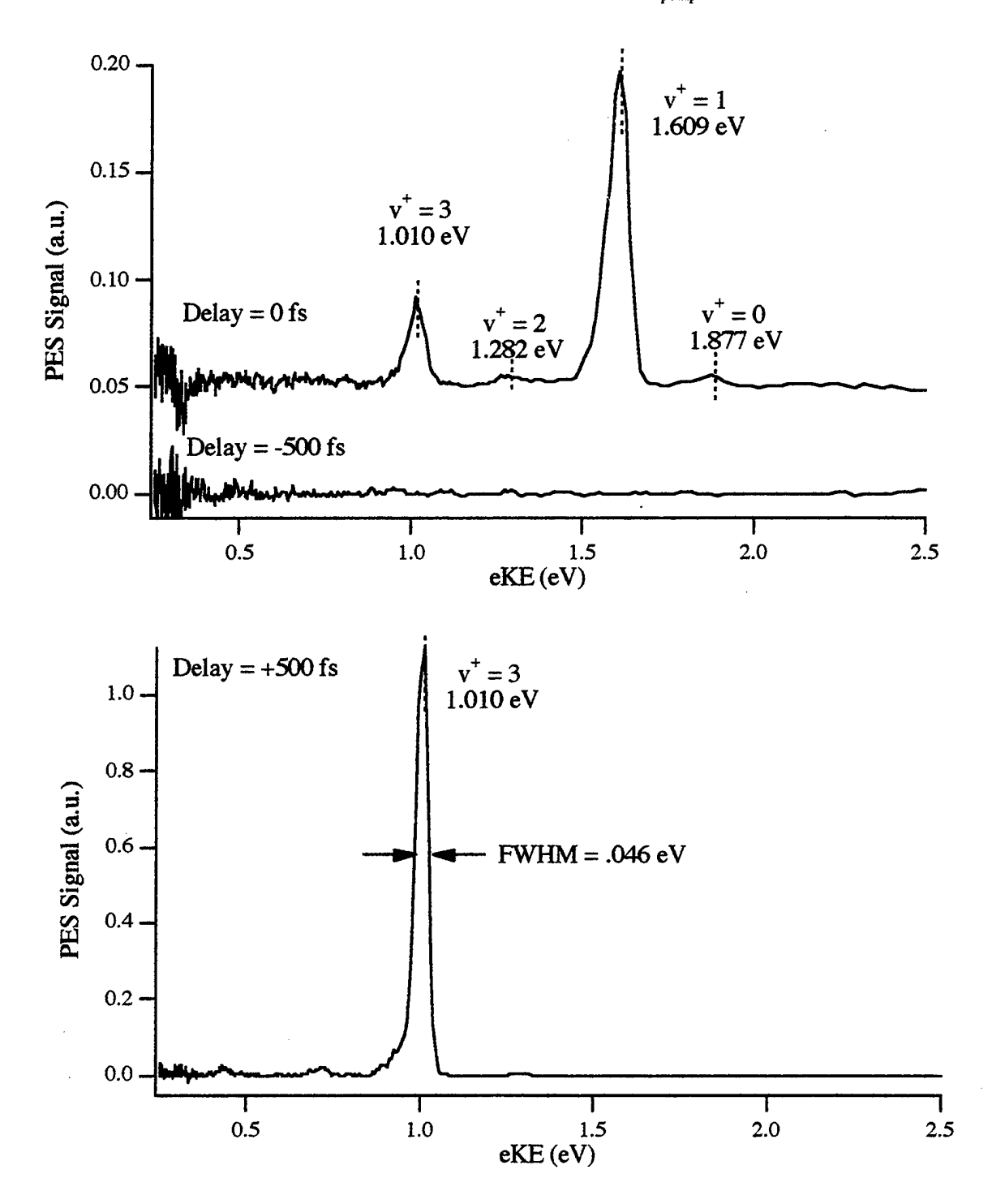
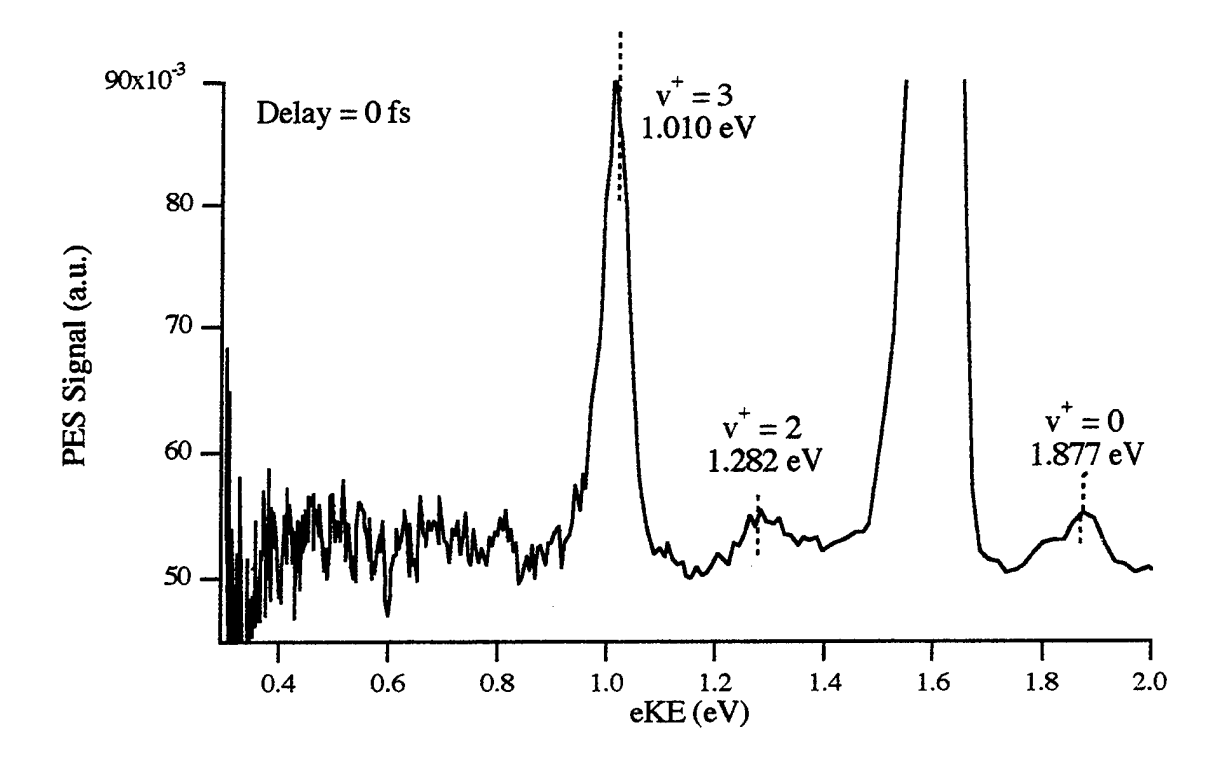
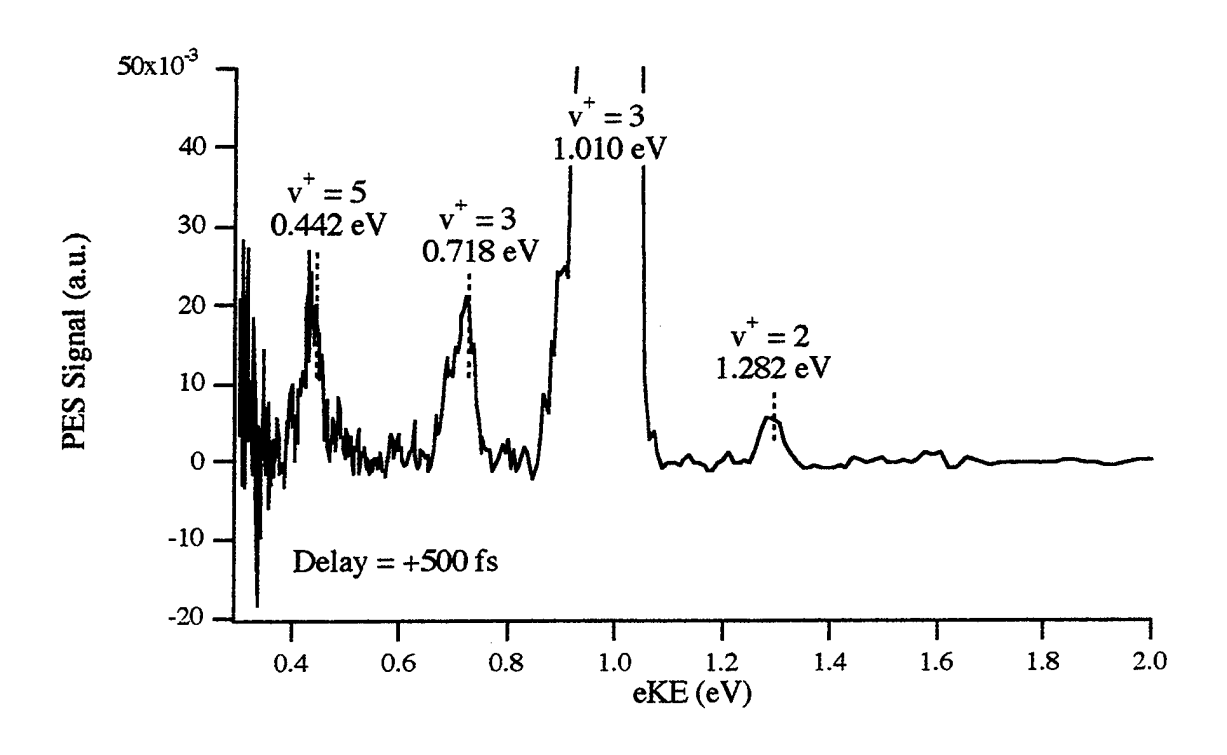


Figure 2.22b Time-resolved PES of NO at $\lambda_{\text{pump}}\!=\!390\;\text{nm}$





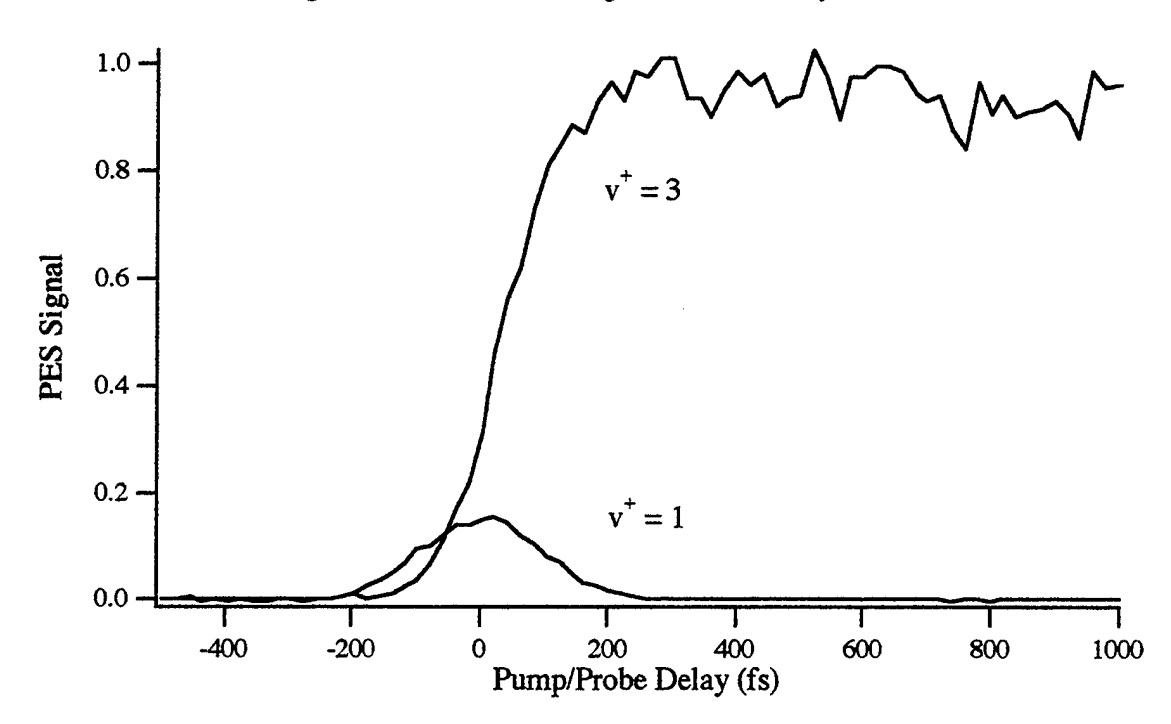


Figure 2.22c Electron Integrated Time Delay Scan

Clearly, the spectra represent the pump exciting the A $^2\Sigma^+$, v=3 state, which is long lived. The probe ionizes this state, but since the pump-prepared state is Rydberg nature, the $\Delta v=0$ transition rule dominates. The spectrum at zero delay can be assigned from a direct ionization from the sum of the 2 pump and 1 probe pulses, in which hv_{total} is the sum of 2 pump photons and 1 probe photon:

$$eKE=hv_{total}-I.P.,$$
 [33]

There is an accidental 1 pump + 1 probe accidental resonance of a higher lying F, v=1 Rydberg state, which causes a large $v^+=1$ peak in the spectra (40). Table 2.5 lists the assignment of the peaks. The experimentally determined average vibrational frequency is .287 eV, which is very close to the predicted value. The measured resolution of the $v^+=3$

peak is $\Delta eKE/eKE = .046$, and the average error is +/- .014 eV, which are very close to the values measured from the pump only 4 photon PES data.

Table 2.5 Assignment of Time-resolved PES of NO at λ_{pump} = 390 nm $delay = 0 \ fs$

$$eKE = 2hv_{pump} + 1 hv_{probe} - I.P.$$

$$2hv_{pump} = 6.358 \text{ eV } 1 \text{ h}v_{probe} = 4.769 \text{ eV}$$

NO (X
$$^2\Pi$$
, v = 0) \rightarrow NO* (A $^2\Sigma^+$, v = 3) 6.340 eV (Hertzberg)

ion vibrational state	observed eKE	expected eKE	absolute error
$\mathbf{v}^{+} = 0$	1.877 eV	1.866 eV	+.011 eV
1	1.609	1.576	+.033
2	1.282	1.289	007
3	1.010	1.006	+.004

$$delay = +500 \text{ fs}$$

eKE =
$$(A^2\Sigma^+, v = 3 + 1 hv_{probe})$$
 - I.P.

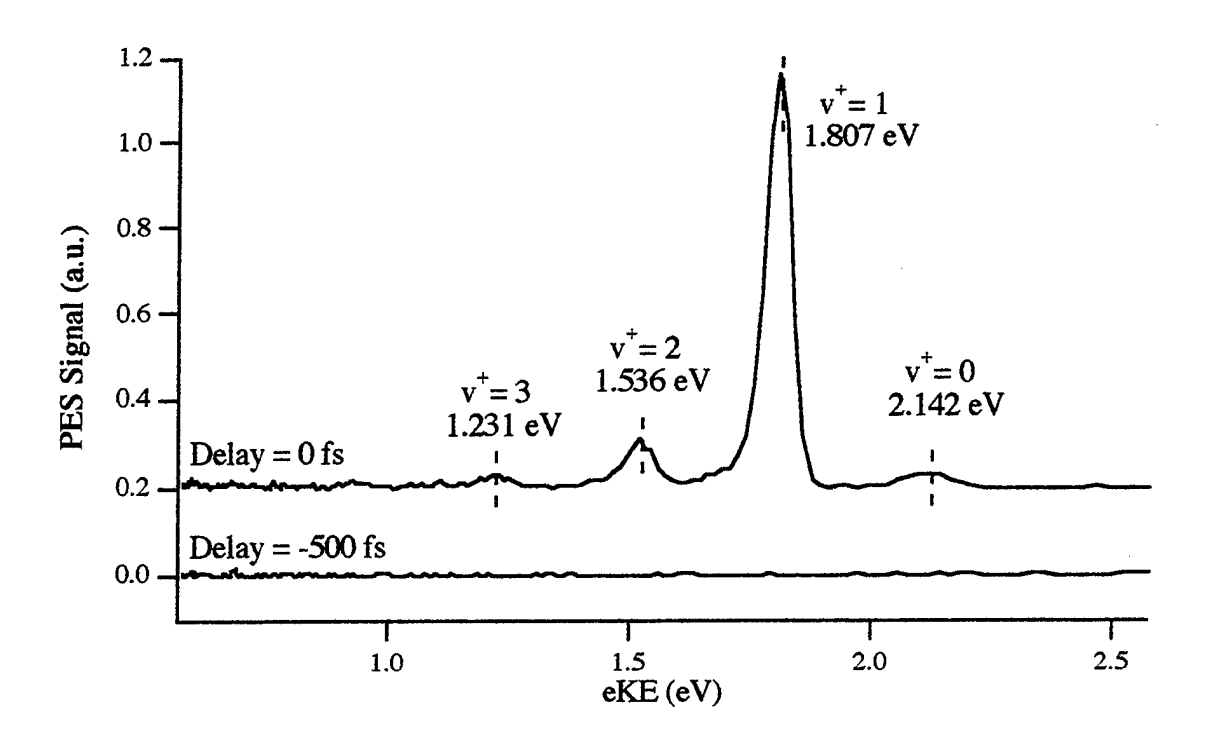
ion vibrational state	observed eKE	expected eKE	absolute error
$v^+ = 2$	1.282 eV	1.289 eV	007 eV
3	1.010	1.006	+.004
4	0.718	0.726	008
5	0.442	0.463	021

If the laser system is tuned to shorter wavelength, a different Rydberg state is tuned into resonance. The C $^2\Pi$, v=0 state can be reached by a two photon absorption at 382 nm. The resulting pump/probe PES at finite delay can be described as:

NO
$$(X^2\Pi) + 2hv_{pump} \rightarrow NO*$$
 $(C^2\Pi, v = 0) + 1hv_{probe} \rightarrow NO^+$ $(X^1\Sigma^+, v^+ = 0) + e^-$
Since the C state is also Rydberg-like in nature, the probe will promote $\Delta v = 0$ transitions to the ion, even though many vibrational levels are accessible. The time-resolved PES of this state is shown in figures 2.23a and 2.23b, and table 2.6 displays the assignment. The signal at zero delay is dominated by the transient $v^+ = 1$ peak, again due to an accidental 1 pump + 1 probe resonance of higher Rydberg state, and the long-lived peak is the $v^+ = 0$. In this case the higher Rydberg state is the H, $v = 1$ state(38.b). The resolution of the $v^+ = 0$ peak is nearly the same as measured in the 4 photon pump only PES.

The dynamics of this system is quite straight forward, but the probe-only, pump-only, and pump/probe spectra shows that a variety of peaks can be obtained easily from the two wavelengths of the pump and probe pulses. This has the advantage of acquiring an excellent calibrating molecule for the time-resolved PES of chlorine dioxide studied in chapter 4.

Figure 2.23a Time -resolved PES of NO λ_{pump} = 382 nm



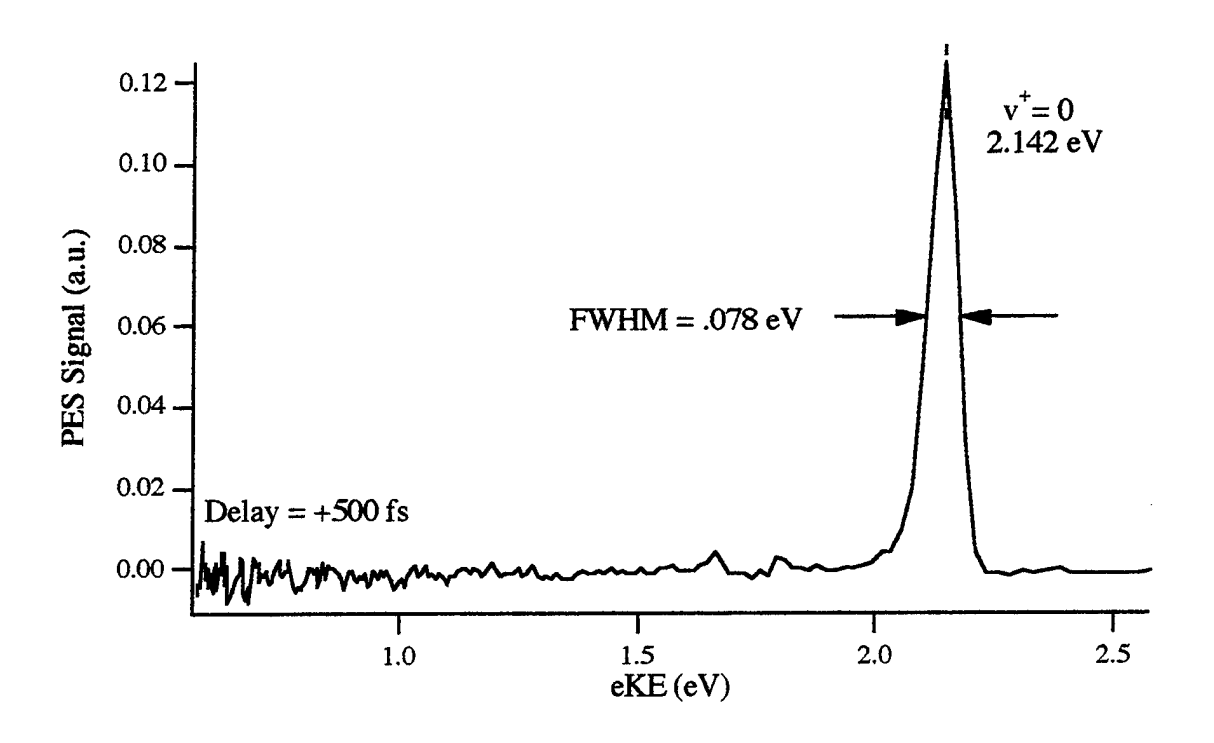


Figure 2.23b Electron Integrated Delay Scan at $\lambda_{\text{pump}} = 382 \text{ nm}$

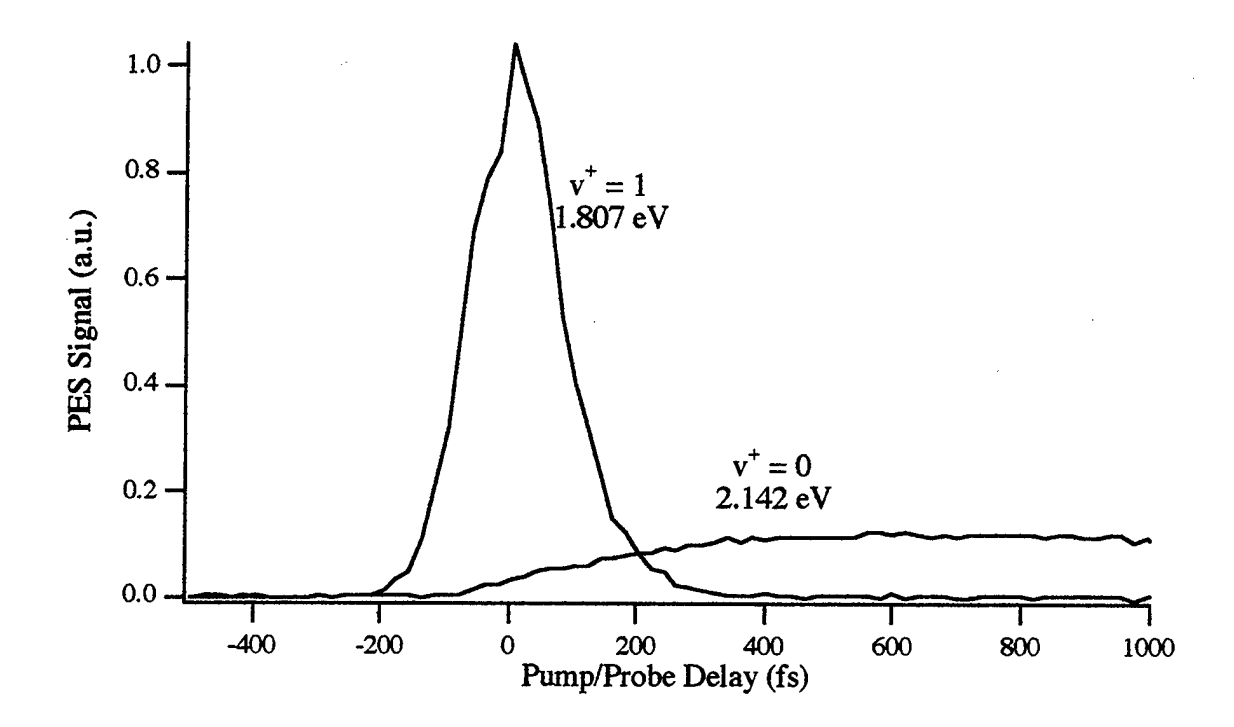


Table 2.6 Assignment of Time-resolved PES of NO at $\lambda_{pump} = 382 \text{ nm}$

delay = 0 fs
$$eKE = 2hv_{pump} + 1 hv_{probe} - I.P$$

$$2hv_{pump} = 6.492 eV \qquad 1 hv_{probe} = 4.869 eV$$

NO (X $^2\Pi$, v = 0) \rightarrow NO* (C $^2\Pi$, v = 0) 6.497 eV (Hertzberg)

ion vibrational state	observed eKE	expected eKE	absolute error
$\mathbf{v}^{+} = 0$	2.142 eV	2.097 eV	+.045 eV
1	1.807	1.807	+.000
2	1.536	1.520	+.016
3	1.231	1.237	006

2.8 Mass Calibration

The calibration of the mass data was done by fixing the flight distance to 15.9 cm, and using the kinetic energy of the ions as a parameter to fit known samples of xenon, argon, krypton, and nitric oxide masses:

$$K.E = \frac{1}{2}m\left(\frac{d}{t}\right)^2,$$
 [3]

where m_i correspond to the masses of xenon, krypton, argon, and nitric oxide, d is the 15.9 cm flight path, and t is the corrected flight time. The best fit of the KE is 1725 eV. Unknown masses are found by calculating mass, m, from the known parameters and corrected flight time:

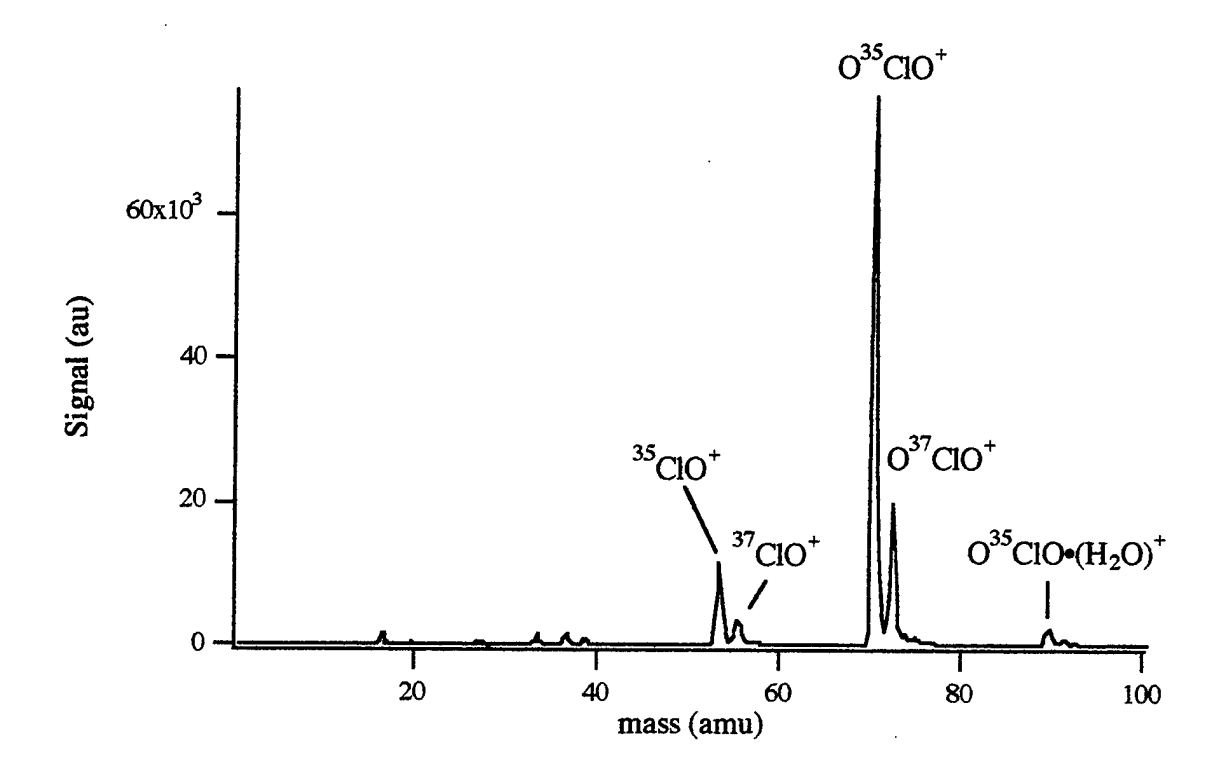
$$m = 2K.E.\frac{t^2}{d^2}.$$
 [34]

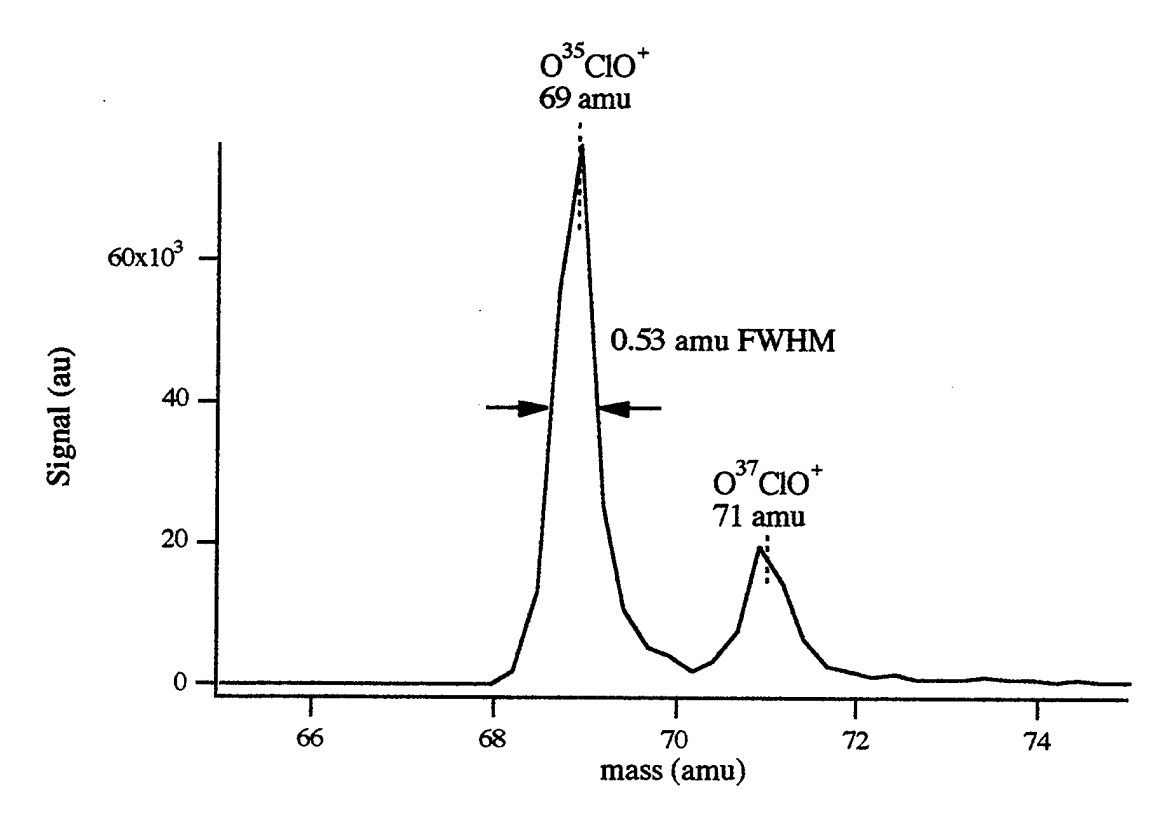
This is not rigorous, because of the two stages of acceleration, but was adequate to fit the data to within the instrumental resolution. A typical mass spectrum of the chlorine dioxide mass experiments is presented in figure 2.24. This is a pump-only spectrum, which requires a 1+3 resonance enhanced multiphoton ionization (REMPI):

OCIO (X
$${}^{2}B_{1}$$
) + $hv_{385nm} \rightarrow OCIO^{*}$ (A ${}^{2}A_{2}$) + $3hv_{385nm} \rightarrow OCIO^{+}$.

The ionization potential of OCIO is 10.348 eV, and the threshold for fragmentation of the OCIO⁺ ion is at 13.5 eV (36). Five photons are needed at this wavelength to reach the fragmentation threshold, which results in a total ionization energy of 16.02 eV. This is in agreement with the experimental spectrum, as there is an appreciable amount of CIO⁺ observed. The experimental resolution of the chlorine dioxide ion is $\frac{\Delta m}{m} = 0.53/69 = .00768$, which is close to the expected value of 0.0067. The resolution is also good enough to resolve the isotopes of the OCIO·H₂O cluster. The measured resolution is appropriate for determining all the dissociation products, namely CIO, CI, O, and O₂.

Figure 2.24 fs Mass Spectra of OClO





Chapter 2 References

- R. E. Walkup, J. A. Misewich, J. H. Glownia, and P. P. Sorokin, Phys. Rev. Lett.
 65, 2366 (1990).
 J. H. Glownia, J. A. Misewich, and P. P. Sorokin, J. Chem.
 Phy. 92, 3335 (1990).
- 2. A. H. Zewail, J. Phys. Chem. 100, 12701 (1996) and references therein.
- 3.a. F. Lindenberger, C. Rausha, H. G. Purucker, and A. Laubereau, J. Raman Spec.
 26, 835 (1995). b. V. F. Kamalov, and Y. P. Svirko, Chem. Phys. Lett. 194, 13 (1992).
- 4.a. M. Motzkus, S. Pedersen, and A. H. Zewail, J. Phys. Chem 100, 5620 (1996).
 b. E. T. J. Nibbering, D. A. Wiersma, and K. Duppen, Chem. Phys. 183, 167 (1994).
- M. Dantus, M. H. M. Janssen, A. H. Zewail, Chem. Phys. Lett. 181, 281 (1991).
 S. A. Trushia, W. Fuss, T. Schikarskirt, W. E. Scmid, et al, J. Chem. Phys. 106, 9386, (1997).
 C. D. R. Cyr and C. C. Hayden, J. Chem. Phys. 104, 771 (1996).
 B. J. Greenblatt, M. T. Zanni, and D. M. Neumark, Science 276, 1675 (1997).
 I. Fischer, M. J. J. Vrakking, D. M. Villeneuve, and A. Stolow, Chem. Phys. 207, 331 (1996).
 F. V. Engel, T. Baumert, Ch. Meier, and G. Gerber, Z. Phys. D 28, 37 (1993).
- 6. J. Blambert, H. F. Shurvell, D. Lightner, R. G. Cooks, <u>Introduction to Modern</u>

 Organic Spectroscopy, New York, John Wiley and Sons, 1978.
- 7. W. C. Wiley and I.H. McLaren, Rev. Sci. Inst. 26, 1150 (1955).
- 8. D. M. Lubman and R. M. Jordan, Rev. Sci. Inst. 56, 373 (1985).
- 9. J. Berkowitz, <u>Photoabsorption</u>, <u>Photoionization</u>, and <u>Photoelectron Spectroscopy</u>, New York, Academic Press, 1979.
- 10.a. J. H. D. Eland, <u>Photoelectron Spectroscopy: an Introduction to Ultraviolet</u>

 <u>Photoelectron Spectroscopy in the Gas Phase</u>, London, Butterworths, 1984.

- b. J. H. D. Eland, J. Phys. E: Sci. Instrum. 11, 969 (1978), and references therein.
- S. L. Anderson, D. M. Rider, and R. N. Zare, Chem. Phys. Lett. 93, 11 (1982).
 M. G. White, R. A. Rosenburg, G. Gabor, E.D. Poliakoff, G. Thompson, S. H. Southworth, and D. A. Shirley, Rev. Sci. Inst. 50, 1268 (1979).
- 12. R. E. Ballard, <u>Photoelectron Spectroscopy and Molecular Orbital Theory</u>, New York, John Wiley and Sons, 1978.
- S. W. Allendorf, D. J. Leahy, D. C. Jacobs, and R. N. Zare, J. Chem. Phys. 91, 2216 (1989).
 - b.R. B. Metz, A. Weaver, S. E. Bradforth, T. N. Kitsopoulos, and D. M. Neumark, J. Phys. Chem. 94, 1377 (1990).
- 14. J. J. Sakurai, <u>Modern Quantum Mechanics</u>, Redwood City, CA, Addison-Wesley 1985.
- 15. W. Demtroder, <u>Laser Spectroscopy: Basic Concepts and Instrumentation</u>, 3rd ed, Berlin, Springer-Verlag, 1988.
- J. E. Pollard, D. J. Trevor, Y. T. Lee, and D. A. Shirley, Rev Sci. Instrum. 52, 1837 (1981).
- 17. L. Hunziker, Ph. D. Thesis, University of California, Berkeley, 1997.
- M. M. Murnane and H. C. Kapteyn, <u>Mode-Locked Ti:Sapphire Laser Rev 1.6</u>,
 Pullman, WA, Washington State University, 1992.
- 19. R. L. Fork, O.E. Martinez, and J.P. Gordon, Opt. Lett. 9, 150 (1984).
- 20. H. P. Weber, J. Appl. Phys. 38, 2231 (1967).
- 21. Y. R. Shen, <u>The Principles of Nonlinear Optics</u>, New York, John Wiley and Sons, 1984.
- 22. D. J. Bradley and G. H. C. New, Proceed. IEEE 62, 313 (1974).
- P. Maine, D. Strickland, P. Babo, M. Pessot, and G. Mourou, IEEE J. Quan. Elec.
 398 (1988).

- 24.a. A. Zavriyev, I. Fischer, D. M. Villeneuve, and A. Stolow, Chem. Phys. Lett. 234, 281 (1995). b. P.Ludowise, M. Blackwell, and Y. Chen, Chem. Phys. Lett. 258, 530 (1996). c. M. Blackwell, P. Ludowise, and Y. Chen, J. Chem. Phys. 107, 283 (1997).
- 25.a. J. H. Moore, C. C. Davis, M. H. Coplan, <u>Building Scientific Apparatus</u>, Redwood City, CA, Addison-Wesley, 1989.
- 26. C. Longfellow, private communication.
- 27. H. F. Davis, Ph. D. thesis, University of California, Berkeley, 1992.
- 28. R. Serway, <u>Physics for Engineers and Scientists 2nd ed.</u>, Philadelphia, Saunders, 1986.
- 29. R. E. Kennerly and R. A. Bonham, Chem. Phys. Lett. 43, 245 (1976).
- 30.a. C. Lewis, W. R. Ware, L. J. Doemeny, and T. L. Nemzek, Rev. Sci. Instrum. 44, 107 (1973). b. S. A. Nowak and F. E. Lytle, Appl. Spec. 45, 728 (1991).
- R. N. M. Compton, J. C. Miller, A. E. Carter, and P. Kruit, Chem. Phys. Lett. 71, 87 (1980).
- 32. J. L. Franklin and J. G. Dillard, Nat. Stand, Ref. Data Ser. NBS26, 1969.
- 33. J. C. Miller and R. N. Compton, J. Chem. Phys. 84, 675 (1986).
- 34. H. A. Strobel, and W. R. Heineman, <u>Chemical Instrumentation: A Systematic</u>

 Approach, 3rd ed., New York, John Wiley and Sons, 1986.
- 35. G. Hertzberg, Spectra of Diatomic Molecules, New York, New York, Van Nostrand Reinhold, 1950.
- 36. G. W. Bethke, J. Chem. Phys. 31, 662 (1959).
- 37. S. T. Pratt, P. M. Dehmer, and J. L. Dehmer, J. Chem. Phy. 85, 5535 (1986).
- 38.a. J. C. Miller, and R. N. Compton, J. Chem. Phys. 75, 22, (1981).b. M. Blackwell, Ph. D. Thesis, University of California, Berkeley, 1997.
- 39.a. J. Kinmann, P. Kruit, and M. J. Van der Wiel, Chem Phys. Lett. 88, 580 (1982).b. Y. Achiba, K. Sato, and K. Kimura, J. Chem. Phys. 82, 3959 (1985).

Chapter 3

The Photodissociation Dynamics of Chlorine Dioxide Studied by Time-resolved Mass Spectrometry

3.1 Introduction

There has been great deal of interest in atmospheric ozone chemistry ever since Molina and co-workers predicted the catastrophic loss of ozone in the stratosphere, mainly due to reactions with free radicals generated from man-made sources (1). The first evidence was found by Farman et al., who measured a 50% drop in the ozone concentration above Antarctica in September, 1980, which was anticorrelated to the concentration of chlorine oxide, ClO, a product of ozone loss (2). Over the next 10 years two major catalytic mechanisms were established to explain the ozone loss (3). Both cycles involve the chlorine atom is a product of the ultraviolet photolysis of chlorofluorocarbons (CFC's), which are common refrigerants are used throughout the world.

Mechanism I:

i.
$$2(Cl + O_3 \rightarrow ClO + O_2)$$

ii. $ClO + ClO + M \rightarrow (ClO)_2 + M$
iii. $(ClO)_2 + hv \rightarrow ClOO + Cl$
iv. $ClOO \rightarrow Cl + O_2$
net: $2 O_3 + hv \rightarrow 3 O_2$

M is a collision partner that does not undergo any chemical changes in the cycle. The rate limiting step of the cycle is determined by the formation of the chlorine monoxide dimer, $(ClO)_2$, in step ii. The dimer decomposes upon ultraviolet photolysis to an asymmetric form of chlorine dioxide, ClOO. This form of chlorine dioxide is kinetically unstable and spontaneously decomposes to Cl and O_2 . The net of this cycle is the conversion of two ozone molecules to three oxygen molecules. The free Cl is recovered can initiate the process again.

The second mechanism involves the identical initial step, but step ii involves free bromine, Br, which is generated by ultraviolet photolysis of halons (bromofluorocarbons). Halons are synthesized widely for use in chemical fire extinguishers. Br reacts with ozone to form the bromine oxide radical, BrO. The rate limiting step iii involves the production of ClOO from the two halogen monoxides. The ClOO subsequently decomposes in the same manner as in Mechanism I. The net is the conversion of two ozone molecules to three oxygen molecules. Br and Cl are recovered to be used in the chain cycle.

Mechanism II:

i.
$$Cl + O_3 \rightarrow ClO + O_2$$

ii. $Br + O_3 \rightarrow BrO + O_2$
iii. $BrO + ClO \rightarrow Br + ClOO$
iv. $ClOO + M \rightarrow Cl + O_2 + M$
net: $2 O_3 \rightarrow 3 O_2$

In the late 1980's, a variety of condensed phase experiments found a second reaction in step iii, where the symmetric isomer of chlorine dioxide is formed with a 50% branching ratio (4):

$$BrO + ClO \rightarrow Br + OClO$$
.

This isomer is thermodynamically less stable than ClOO, but is kinetically stable, and has been isolated and studied under laboratory conditions (4). The relevance of OClO to the stratospheric ozone depletion was first measured by the ground based OClO concentrations above Antarctica of Soloman (5) and the aircraft measurements of Wahner (6), who found the OClO concentration to be 100 times of that of other latitudes, and spring time concentrations that were anticorrelated with ozone. This suggested that the photochemistry of OClO may be linked to ozone loss chemistry.

The photochemistry of OCIO has only been recently considered to be important. Historically it was thought to rapidly decompose upon ultraviolet light photolysis to chlorine monoxide and an oxygen atom (7). The quantum yield for dissociation was determined to be unity:

OClO (X
$${}^{2}B_{1}$$
)+ hv \rightarrow OClO* (A ${}^{2}A_{2}$) \rightarrow ClO (${}^{2}\Pi$) + O (${}^{3}P$)

This would be unimportant in the ozone loss mechanisms, because the oxygen atom would quickly react with an oxygen molecule to from an ozone molecule, leading to null in the destruction mechanisms:

$$O + O_2 \rightarrow O_3$$
.

Experiments in the 1990's, however, determined that a second dissociation channel was open that would contribute to ozone loss (8):

OCIO (X
$${}^{2}B_{1}$$
)+ hv \rightarrow OCIO* (A ${}^{2}A_{2}$) \rightarrow CIO (${}^{2}\Pi$) + O (${}^{3}P$) [1]

→ Cl (
$${}^{3}P$$
)+ O₂ (${}^{3}\Sigma_{g}^{-}$, ${}^{1}\Delta$, ${}^{1}\Sigma_{g}^{+}$). [2]

Recent interest has been in determining how important reaction [2] is in the ozone budget. A wide discrepancy of the branching ratio, ranging from <.1% to approximately 15%, have been reported, but a 10% branching ratio would lead to a significant effect on the stratospheric ozone budget (9). Furthermore, calculations modeling the atmospheric ozone loss have assumed that the yield for reaction [1] is 100% (9).

Bishenden and Donaldson determined that reaction [2] is important near 360 nm (10). After photolysis, a probe laser determined the relative amounts of Cl and ClO by resonance enhanced multi-photon ionization (REMPI). The Cl/ClO branching ratio was found to be 15% at 360 nm excitation, but the remaining products were not detected.

In a photofragment translational energy experiment, Davis and Lee measured the ratio to be a maximum of 3.9% at 404 nm, and less than .1% at wavelengths shorter than 370 nm (11). A mode specific behavior, in which 10 times as much Cl and O_2 were produced by exciting the bend of the parent. This was attributed to the nearby 2B_2 state. The equilibrium geometry of this state has a bond angle of 90 degrees, which is quite different from the optically prepared A 2A_2 state, which has a bond angle of 120 degrees. Therefore, bending excitation would aid the coupling to the dissociative 2B_2 state. Theoretical calculations of Gole predict that the oxygen formed in this case would be electronically excited (12). His results estimated that the majority of the O_2 produced is

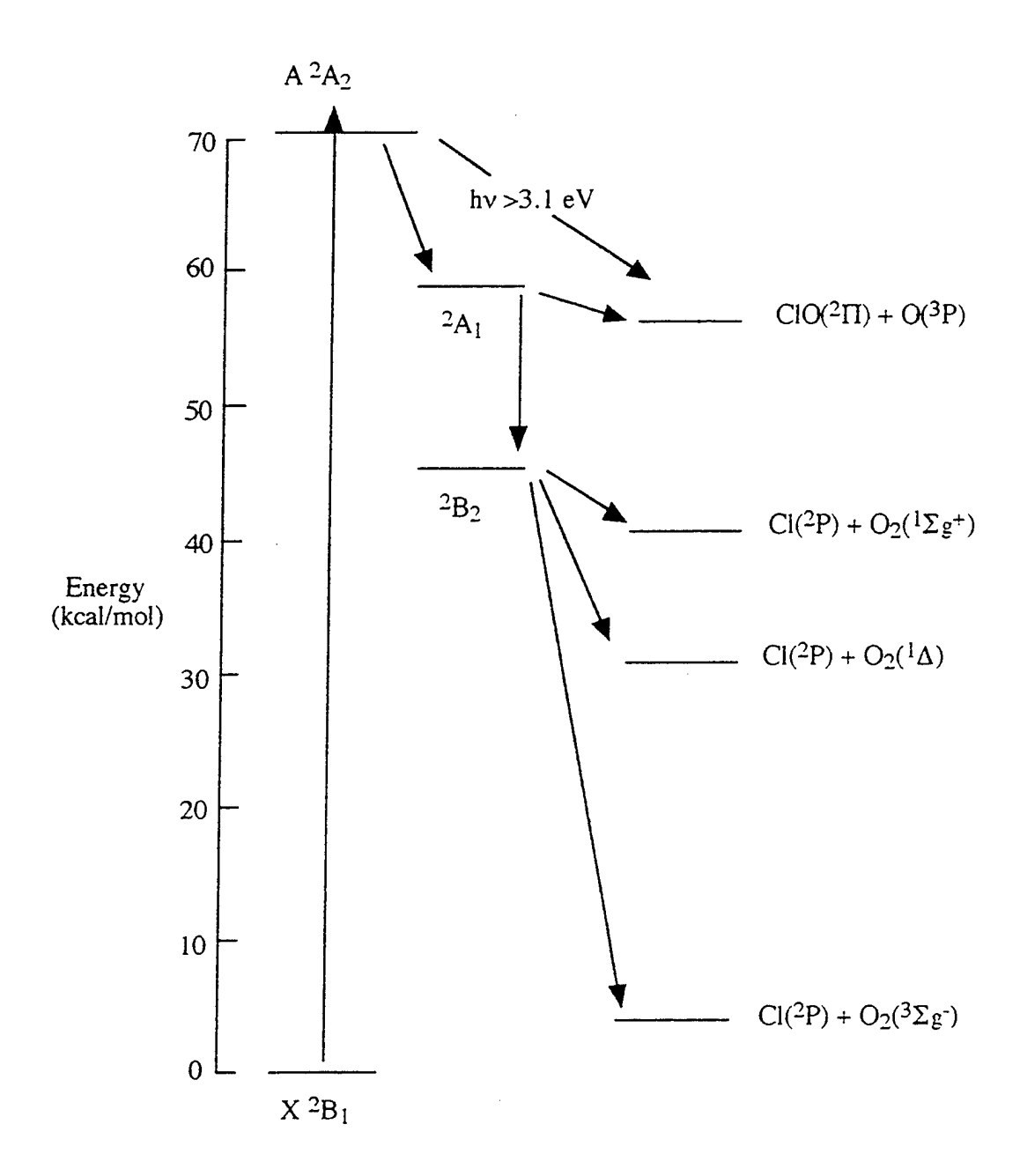
electronically excited, and most likely in the $^{1}\Delta$ state. Davis and Lee estimated that 80% of the molecular oxygen produced is electronically excited.

The angular distribution of the products and large kinetic energy releases of the photofragment experiment seemed to indicate a short lived intermediate state. They estimated the wavelength dependent life time to vary from approximately 10 ps near 400 nm, to a few ps near 350 nm. They estimated the barrier direct dissociation on the A 2 A₂ state to be near 3.1 eV (400 nm), which is agreement with a negligible amount of fluorescence of the excited A 2 A₂ state above 3.1 eV (13).

Vaida studied the photodissociation dynamics of the A ²A₂ state by high resolution absorption spectroscopy in a molecular beam (14). The rotational linewidths were found to be homogeneously broadened by predissociation. The corresponding lifetimes varied from ten picoseconds at 3.1 eV, to approximately 1 picosecond at 3.5 eV. A mode specific behavior was observed, in which significant shorter lifetimes (factor of 2-3) were observed upon excitation of the asymmetric stretch, as opposed to the symmetric stretch, or symmetric stretch and bend. The observed lifetimes were consistently 20% longer than those measured by Davis and Lee.

Recent theoretical calculations by Werner explain the observed predissociation data (15). There is a shallow barrier on the A 2 A₂ near 3.1 eV to dissociation to ClO and O. Below 3.1 eV, the molecule dissociates by two indirect mechanisms. Upon excitation to the A 2 A₂ state, the molecule can cross to a 2 A₁ state by a spin-orbit coupling, where it can dissociate to OCl + O. Once in the 2 A₁ state, the molecule can also vibronically couple to a 2 B₂ state, which subsequently dissociates to Cl + O₂. A summary of the photochemical dynamics can be seen in figure 3.1.

Figure 3.1 OCIO Photodissociation Dynamics of OCIO



The ClO, O, and Cl are produced in their ground electronic states. The three lowest states of the oxygen molecule are energetically accessible, but recent calculations by Werner show that the three step dissociation via the ${}^{2}B_{2}$ state would lead to primarily oxygen in the ${}^{1}\Delta$

state (16). Absorption from the X^2B_1 state to the A^2A_1 state is allowed by dipole selection rules, but has never been observed, and absorption to the 2B_2 state is strictly forbidden.

A direct determination of the lifetime of the A 2A_2 state was measured by Zewail between 3.5 and 4.0 eV excitation, which was well above the predicted A 2A_2 state direct dissociation barrier (17). This was done by time-resolved mass spectrometry. After an excitation of a femtosecond pump pulse, an intense femtosecond probe pulse at 620 nm was used to ionize the transition state by a multi-photon transition. The mass spectra acquired at a short pump/probe delay ionized the A 2A_2 state to OClO⁺, and ionized the products at long delay. The OClO⁺ signal had a sharp rise at a zero delay, followed by a biexponential decay. The only product ion detected was the ClO⁺, which had a biexponential rise after zero delay. The data was explained by a two channel dissociation model: a direct channel with a time constant of 50 fs, and an indirect channel of approximately 500 fs, which is consistent with the model set forth by Werner.

Even though there has been considerable experimental and theoretical work on the photodissociation dynamics of OCIO, there many unanswered questions. The first is a direct measurement of the lifetime of the excited state near the dissociation barrier. The Zewail experiments were done approximately 1 eV above the barrier of the A 2 A $_2$ state, so it should be no surprise that the signal is dominated by the direct dissociation channel. The dynamics near the barrier are expected to be different. The photofragment translational energy anisotropy measurements, absorption linewidth, and laser induced fluorescence measurements are indirect methods of determining the lifetime, and thus do not give definitive measurements of the lifetimes. A more appropriate method would be to observe the transition state directly. There should be an intrinsic difference in the dynamics of the CIO and CI products, because the 2 B2 state is predicted to be responsible for the CI and O2 channel. The identification of all the products should also elucidate how important the 2 A1 and 2 B2 states are in the dissociation, as well as a determination of the branching ratio of the two channels.

Even though the work of Zewail, et al. has been instrumental in studying chlorine dioxide photochemistry, there are some issues that are not resolved in their work. The identity of the ion electronic state is not clear. A strong probe laser was needed for the multi-photon transition to ionize the A 2 A₂ state. It is conceivable that the fragmentation he observed was from an excited electronic state of the OCIO+ ion. In his experimental scheme, four probe photons are needed to ionize the A 2 A₂ state. A more appropriate scheme would be to use a shorter wavelength (260 nm), in which two photons would be sufficient to ionize OCIO in the A 2 A₂ state, and would be less likely to be hampered by intermediate resonances and high power effects, such as ponderomotive effects and above threshold ionization (18).

3.2 Experimental

The time-resolved mass spectrometry experiments were performed with the femtosecond (fs) laser system and molecular beam chamber described in chapter 2. The 50 fs laser operated at a wavelength near 770 nm at 3 kHz. The output was passed through a thin BBO crystal tuned for second harmonic generation. Half of this output at 385 nm was passed through an optical delay stage and used for the pump. The typical pump pulse energy was 40 µJoules/pulse but was attenuated to approximately 5 µJoules/pulse by neutral density filters. The probe was the sum frequency generation of the remaining second harmonic and the residual fundamental mixed in another BBO crystal. The typical output at 257 nm is 15 µJoules/pulse. The probe pulse energy was attenuated to 5 µJoules to avoid excessive probe-only mass signal by attenuating the fundamental and frequency doubled input beams before the mixing crystal. The pump and probe were separately focused and combined by a dichroic mirror before entering the ionization chamber of the molecular beam apparatus. An optical chopper was used to automatically subtract the probe only background, which was significantly larger than the pump-only background. The

instrumental time response was measured by a pump/probe cross correlation in a thin KDP crystal by difference frequency generation after the exit window of the time-of-flight molecular beam spectrometer. Typical cross correlation widths were Gaussian in shape with a FWHM of 120 fs.

The molecular beam spectrometer is described in detail in Chapter 2. A 2% mixture of OCIO in Argon was expanded through a continuous nozzle of .100 mm diameter and skimmed twice before entering the ionization chamber. The time-of-flight detector was operated in the manner to detect ions, and had a mass resolution of 150:1 at 100 amu. The pump/probe scans were obtained by acquiring an entire mass spectrum at a given delay, moving the optical delay stage, and acquiring another spectrum. In this manner, the entire mass spectrum is acquired in one laser shot, as opposed to the time-resolved mass experiments of Zewail, et al (17). Typical scans involved 3000 laser shots for each spectrum and 200 delay steps. Each 200 steps would be scanned three to ten times sequentially for reproducibility, as well as pump-only and probe-only background scans. The data was collected by a 66 MHz 486 computer with a Sonix Str-81G 12 bit analog/digital (A/D) converter and digital signal processor (DSP) that can digitize a 1000 point waveform at a 1 ns resolution and a 3.5 kHz repetition rate. The data was later transferred to a 160 Mhz Pentium PC for analysis.

The OClO was produced in situ following the procedure of Derby and Hutchinson (19). A 2% mixture of Cl₂ in argon (Matheson) was passed through a 1 m glass U-tube containing flaked NaClO₂ packed with glass beads. The chlorine was converted to chlorine dioxide by the oxidation-reduction reaction:

$$Cl_2 + 2 \text{ NaClO}_2 \rightarrow 2 \text{ OClO} + 2 \text{ NaCl}.$$

Complete conversion can be obtained if the column is not too dry, apparently as some water is needed to facilitate the reaction. To ensure this, a water bubbler was added in series prior to the U tube, as well as a cold finger trap afterwards (20). The trap was cooled to -20 degrees C by a NaCl salt/ice bath. This removed all of the water from sample before

entering the source of the molecular beam chamber. A schematic of the synthesis manifold is shown in figure 3.2. Teflon and glass tubing and fittings were used wherever possible to avoid decomposition of the sample. Stainless-steel parts were used everywhere else. Care was taken to ensure the pressure in the manifold to be 20 psi or lower to avoid detonation (20). No experiments of pure OCIO were attempted due to its violent nature. Under the source conditions, no water was detected in the mass spectra, and the concentration of clusters of $(OCIO)_x$ and $(OCIO)_x$ (H₂O)_y were less than 5% the size of the parent OCIO.

source

2% Cl₂
in Ar

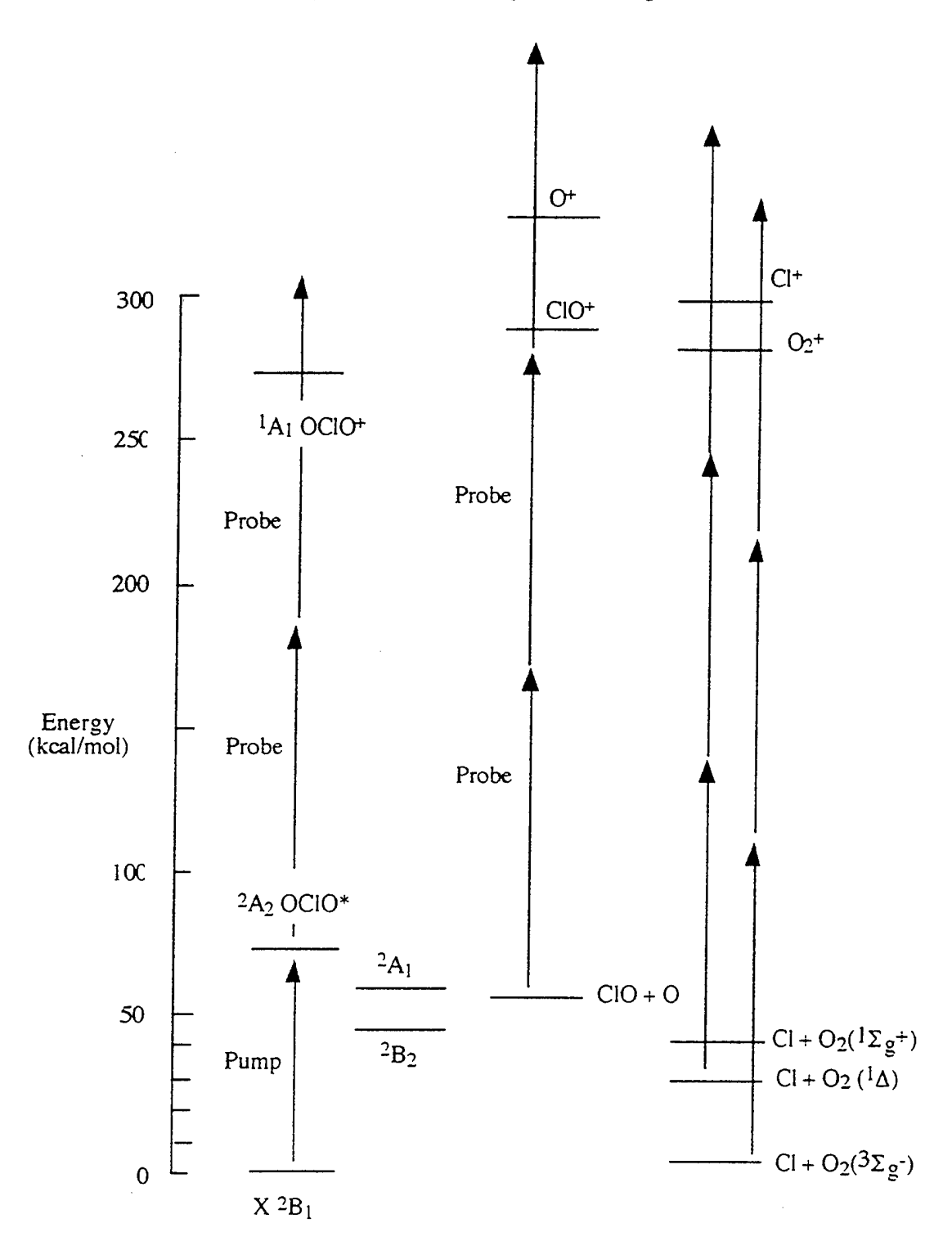
Cold Trap
-20 degree C

Figure 3.2 OCIO Synthesis Manifold

3.3 Results and Discussion

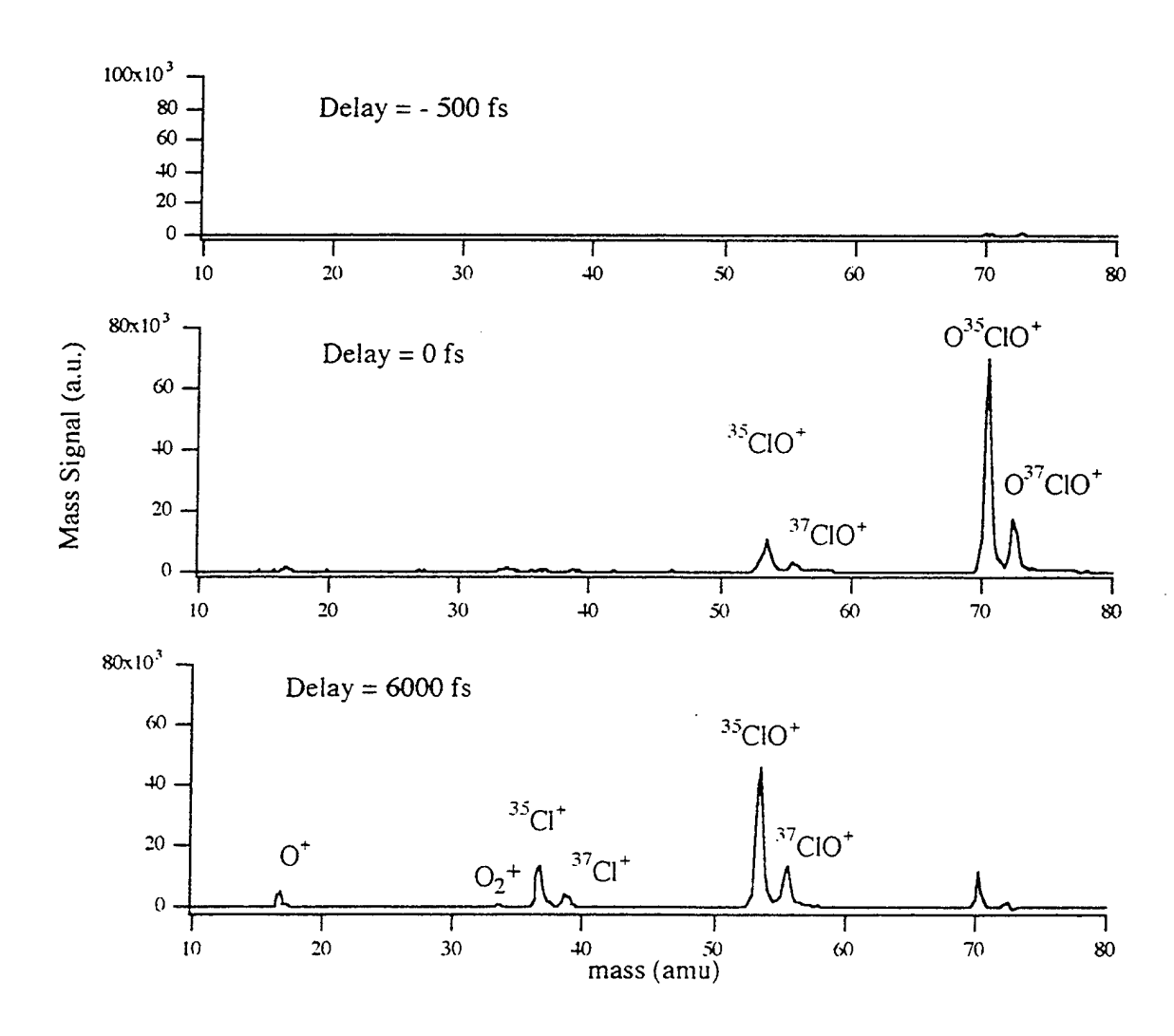
The experimental scheme is that a pump pulse prepares the molecule on the excited A^2A_2 state, where it begins to evolve in time. At a later time, the probe pulse ionizes the parent or products, depending on the pump/probe delay. At the wavelengths used, two probe photons are needed to ionize the parent, and three photons are needed to ionize each of the fragments. This can be seen in figure 4.3, describing the energetics of the reaction, which was constructed from the well-known ionization potentials of each species (21, 22).

Figure 3.3 OCIO Pump/Probe Energetics



Typical pump/probe mass spectra at 385 nm excitation, 257 nm probe (ionization) is shown in figures 3.3. Three pump/probe mass spectra are displayed at three different time delays. At a negative delay time, there is no signal. At zero delay time, there is a sharp increase in the $OClO^+$ signal, with a nonzero value for the ClO^+ , O^+ , Cl^+ , and O_2^+ product ions. At a delay time of 6 ps, the majority of the parent has decayed, and the product species have increased.

Figure 3.3 OCIO Pump/Probe Mass Spectra



A more informative manner displaying the data is the time-dependent integrated mass signal, which is shown in figure 4.4. The delay scans were extended to 30 ps, but only the first 7 ps are shown for clarity.

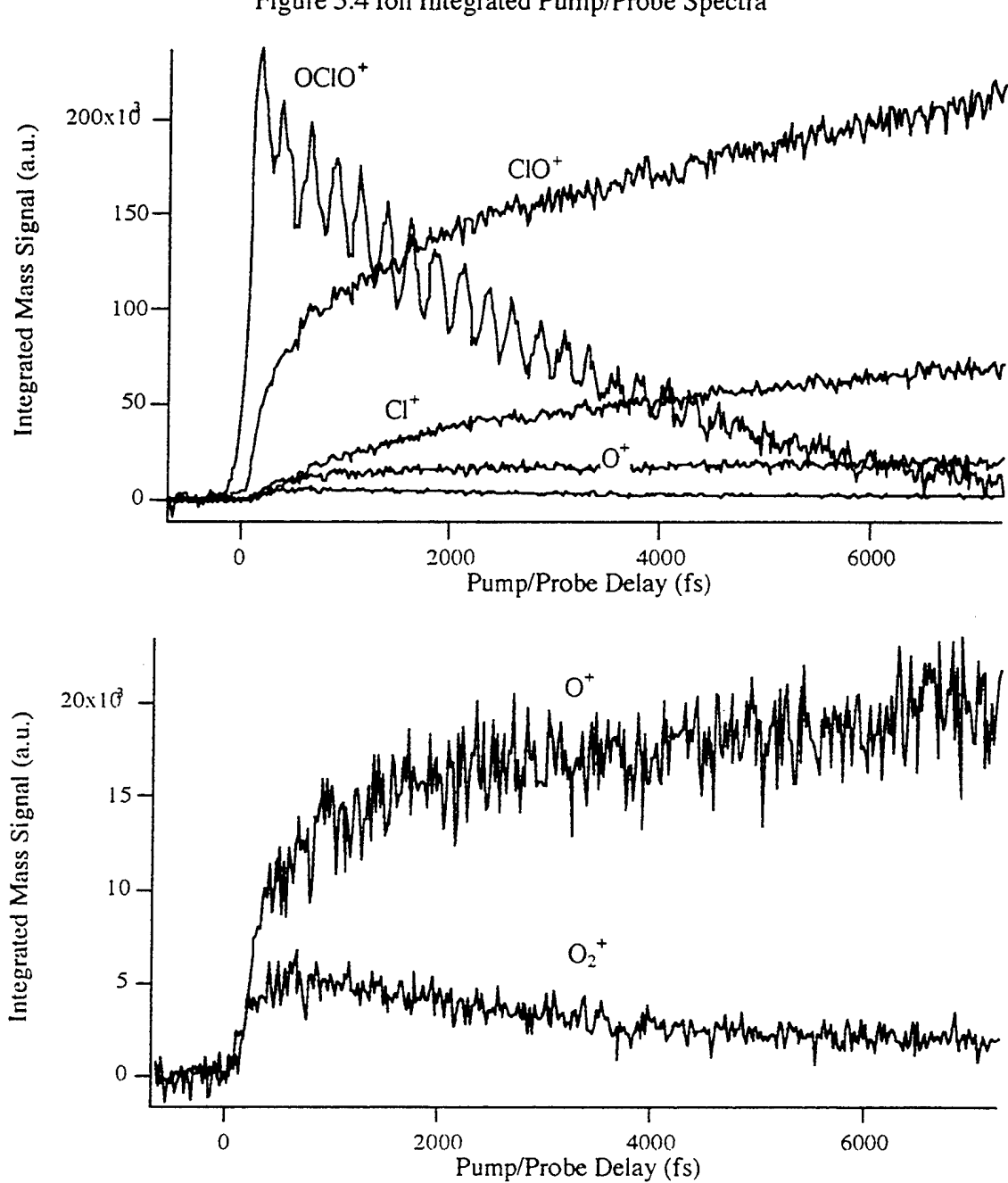
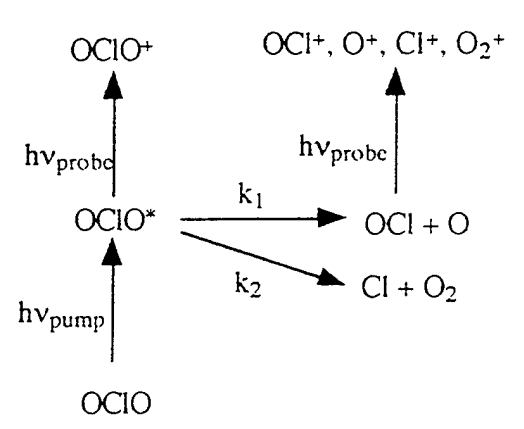


Figure 3.4 Ion Integrated Pump/Probe Spectra

The ion signals are not normalized to their respective ionization cross sections. The lower of the two scans is a zoom of the O^+ and O_2^+ fragments acquired in the top figure. The parent ion shows a sharp rise at zero delay, followed by a coherent oscillation superimposed onto a biexponential decay. The CIO^+ , O^+ , and CI^+ product ions have biexponential rises, but appear to differ from one another. The O_2^+ product has a gradual rise, and then a decay to a nonzero value. A quantum mechanical model must be invoked to explain the coherent behavior of the parent ion, but classical chemical kinetics can be used to explain the photofragments.

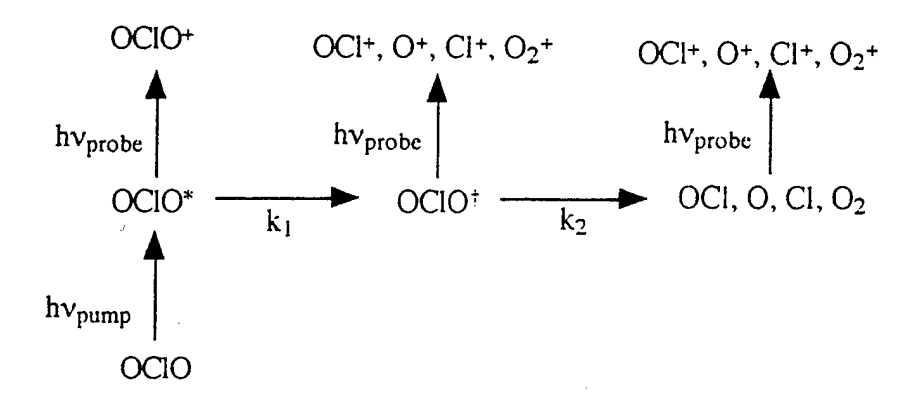
3.31 Product Kinetic Model

The simplest model describing a biexponential rise of the products would be the decay of an excited state by two different means. Such a model would be excitation to the A^2A_2 state by a pump pulse, decay by dissociation to O + ClO with rate constant k_1 , and decay by dissociation to $Cl + O_2$, with rate constant k_2 :



The probe laser subsequently ionizes each of the products. This model would be sufficient only if the time dependence of ClO^+ and O^+ match, and if Cl^+ and O_2^+ match, which is clearly not the case.

A two step model is a more appropriate. After excitation to the A 2A_2 state (OClO*), the molecule evolves to an intermediate state (OClO †) by rate constant k_1 , where it subsequently dissociates to all four products with rate constant k_2 :



A complete derivation of this model is in Appendix 1. An effective rate constant for the two different dissociation channels, k_2 , is used because k_1 is the rate limiting step. Ionization by the probe laser from the OCIO* to the ground state (X 1A_1) of the OCIO*, which is confirmed by the pump/probe PES experiments that is discussed in chapter 4. After the dissociation, the probe ionizes the products to their corresponding ions. All of the ions should have similar time behavior, unless there is a second source of product ions, which is ionization of the OCIO* intermediate state. This state is a mixture of the dark 2A_1 and 2B_2 states. Ionization of the intermediate state leads to an electronically excited OCIO*, which spontaneously dissociates to product ions. The photoelectron and photoionization experiments of Baumgartel, et al., shows that the fragmentation threshold of OCIO* is 13.5 eV (21). The total photon energy of 1 pump + 2 probe is only 12.816 eV, which is below the threshold. Another probe photon would access a higher state of 3B_1 symmetry, which has an adiabatic ionization potential of 16.1 eV (21). The products' time behavior can be explained assuming that the ion dissociation is direct.

One may imagine that the different dynamics of the products may be due to multiphoton effects, such as a two photon absorption to a highly excited state of the neutral, or even a multi-photon transition to an ion state. A subsequent probe absorption would place the molecule on a higher ion state. The dynamics observed would occur on the highly excited neutral or ion state. This is shown not to be the case by a pump power dependence study of the products. The integrated ion signal of each of the photofragments (at a 40 ps delay) taken at different pump powers is shown in figures 3.5.a and 3.5.b. Since one pump photon is needed to excite the molecule to the A 2 A2 state, a linear dependence of pump power is expected (18.a). Figure 3.5.a shows that there is a significant deviation of linearity if a high pump power is used. This is expected due to the femtosecond ponderomotive force, which has been shown to be significant in OCIO photodissociation (18.c). In this experiment, however, only 20 mW of pump power was used, which is well within the linear region of the curve, as shown in figure 3.5.b. The light dashed lines are linear fits of the data to the pump power. Similar experiments have proved that the probe power dependence is quadratic or cubic, depending on the fragment.

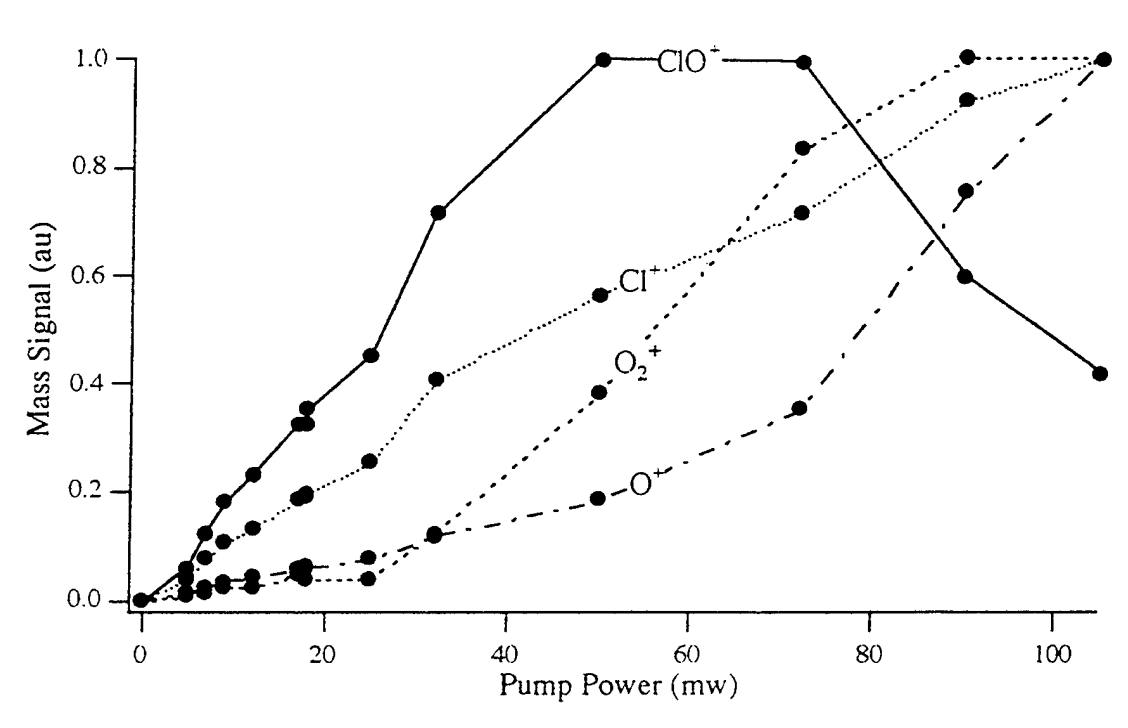


Figure 3.5.a Pump Power Dependence of Product Ions

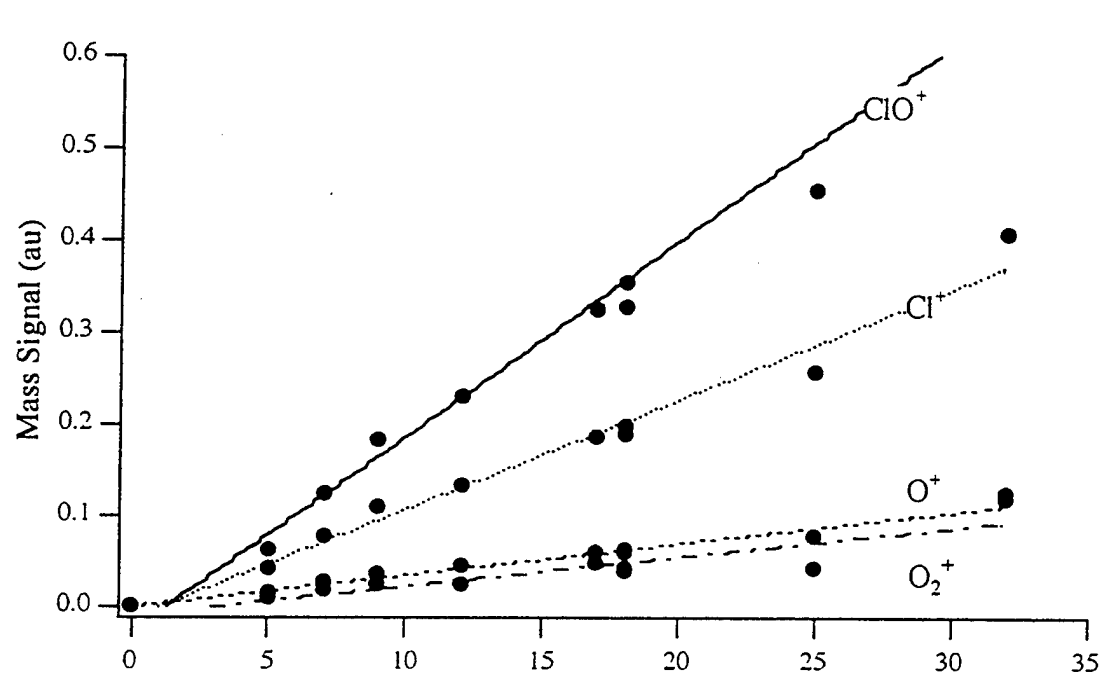


Figure 3.5.b Linear Region of Pump Power Dependence

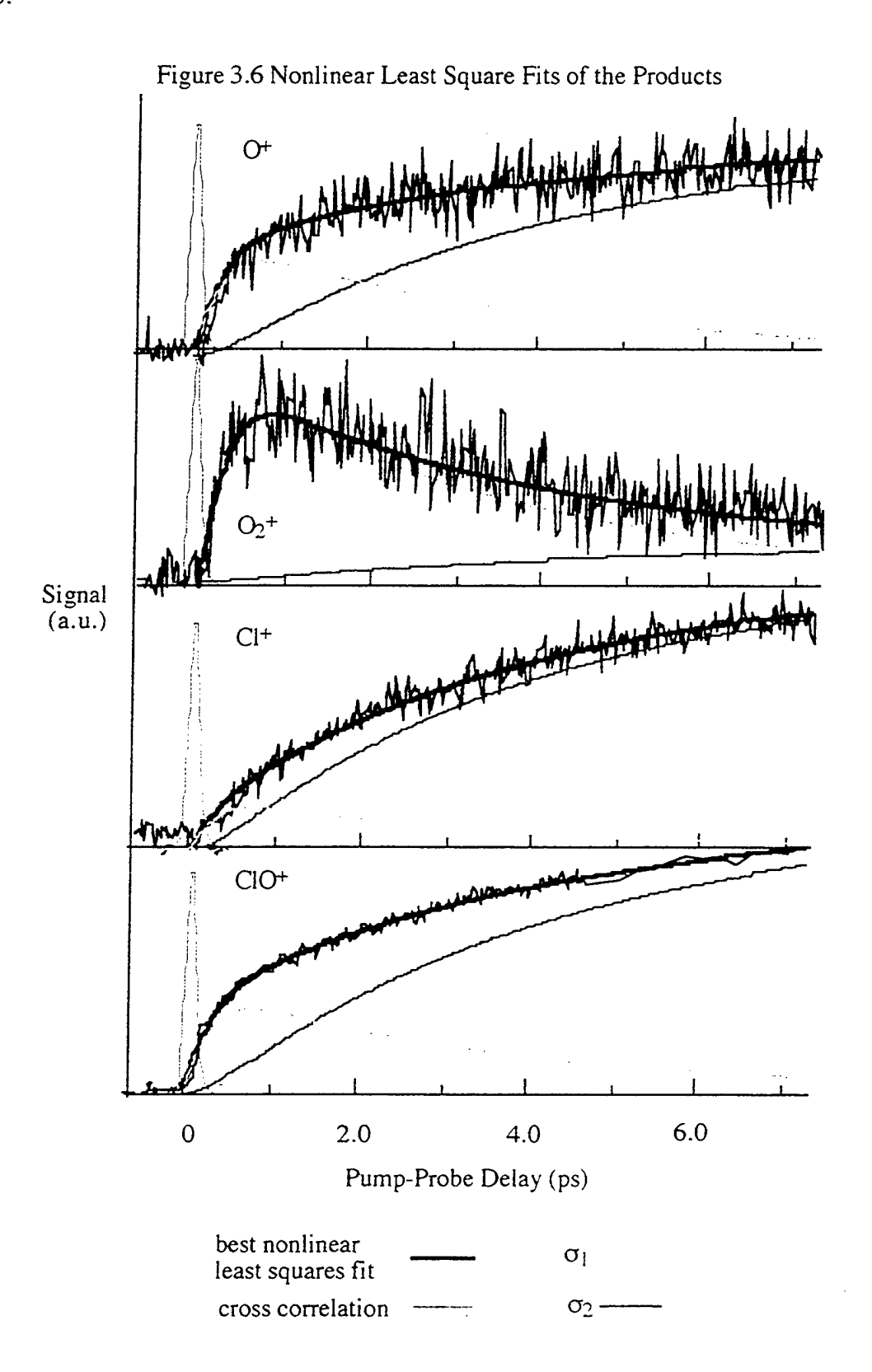
A set of coupled rate equations can be solved to find an analytical function to describe the product ion behavior, which is given in Appendix 1. The time dependence, R(t), of the products is dependent upon k_1 and k_2 by:

Pump Power (mw)

$$R(t) = \sigma_1 \left[\exp(-k_2 t) - \exp(-k_1 t) \right] + \sigma_2 \left[1 - \left(1 - \frac{k_1 + k_2}{k_1 - k_2} \right) \left(\exp(-k_2 t) - \exp(-k_1 t) \right) \right]$$

where k_1 and k_2 are the rate constants from the two step model, σ_1 is the effective cross section for ionization OClO[†] and fragmentation to a product ion, and σ_2 is the effective ionization cross sections for a neutral product ions. In general, the σ_1 and σ_2 will differ from one another, and they will differ from one product ion to another. They are essentially used as scaling factors for the amount of ion that is detected from each source in the model. The time dependence is explicitly in the two rate constants, k_1 and k_2 . Nonlinear least

square fits of each ion's time evolution with identical rate constants are depicted in figure 3.6.



The entire 30 ps of the scan was used to fit the data, but only the first 7 ps are shown for clarity. The Gaussian traces at zero delay time are the measured pump/probe cross correlations. The relative contribution of each ionization pathway (σ_1 and σ_2 terms) are shown as light lines and the dark lines are the fits. The difference from the behavior of the O_2^+ from the other product ions is the majority of it arises from ionization and fragmentation of the OClO[†] as opposed to the ionization of neutral O_2 . Conversely, the ClO⁺ is predominantly from ionization of the neutral ClO. It is important to note that the same k_1 and k_2 constants can fit all of the product ions.

The lifetimes of the OCIO* and OCIO[†] states can be determined because of the rate constants, k_1 and k_2 , are related to time constants, τ_1 and τ_2 , by:

$$\frac{1}{k_1}=\tau_1, \qquad \frac{1}{k_2}=\tau_2.$$

Averages of the experimental k's yield τ_1 = 4.6 ps, and τ_2 = .250 ps. This means that the optically prepared OCIO* (A 2A_2) state survives for 4.6 ps before it crosses to an intermediate state, where it subsequently dissociates in .250 ps. The lifetime of the OCIO* is 30% faster than the lifetime inferred by the high resolution absorption experiments (τ_1 = 6.6 ps at 385 nm excitation), but also explains the short lifetime inferred by the photofragment translational energy angular distribution experiments of Davis and Lee. They observed a large anisotropy of the fragments, and a large kinetic energy release of the CIO and O, which implies that the lifetime in the excited state is short (~1 ps). Yet, both experiments have not captured the full details of the dynamics. The absorption linewidth experiment samples only the early part of the reaction, and the photofragment experiment only samples the latter part of the reaction. The seemingly contradictory results of those experiments can be reconciled upon considering this experiment, which follows the reaction from start to completion.

Another interesting result of the analysis is that there is no direct dissociation channel accessible at 3.2 eV excitation. Theoretical and experimental evidence (12, 13, 15, 16) suggests that the barrier to dissociation is 3.1 eV. If there was a direct dissociation channel open, then the dynamics would be significantly different.

The results show that only one intermediate state, OClO[†], is enough to perturb the OClO* to dissociate. There has been considerable evidence that the dark ²A₁ and ²B₂ states are important. These dark states correlate to ²A' symmetry in C_s geometry, and the ab initio calculations of show that ²A' states have a strong avoided crossing (15, 16). This mixing forms one state with a large dissociation barrier (larger than the A ²A₂ state), and another state with a shallow barrier. Peterson and Werner proposed a three step mechanism, in which the optically prepared A ²A₂ state couples to the ²A₁ state by a spin orbit coupling, which then couples to the ²B₂ state by a vibronic coupling, and finally dissociates to products. The experimental results here show that the mixing is so strong that it merges the last two steps into one.

3.32 OCIO Quantum Mechanical Model

A more elegant model must be incorporated to describe the behavior of the OCIO⁺ time evolution. As shown in figure 4.4, there is a 240 fs quantum beat superimposed on top of a biexponential decay. The origin of this coherent oscillation can be determined from the high resolution absorption data of Vaida, et. al (14). Near 385 nm, there is a vibrational progression of (700), (602), (710), and (612), where $(v_1v_2v_3)$ correspond to the symmetric stretch, bend, and asymmetric stretch vibrational quanta, respectively. As discussed in Section 2.2., the energy bandwidth of the fs pump pulse used in these experiments is $26110 + 170 \text{ cm}^{-1}$, which has enough bandwidth to excite the (700) and (602) modes of the A 2 A₂ state. Both states decay to the intermediate state OCIO⁺ at different rates, but a superposition state of (700) and (602) is formed. This nonstationary states oscillates between the classical turning points on the optically prepared OCIO⁺ state. As the state

oscillates, it changes Franck-Condon factors with the ion state, so the ion signal oscillates at a characteristic frequency of the optically prepared OClO* state. Yet, the molecule has a finite probability of crossing to the intermediate state. There is a decay from each vibrational level excited, so there is a biexponential decay of the population of the OClO* state. On top of the biexponential decay is an oscillation which has an oscillation period, T, that is related to the difference in energy of the two states (in cm⁻¹), ΔE, as:

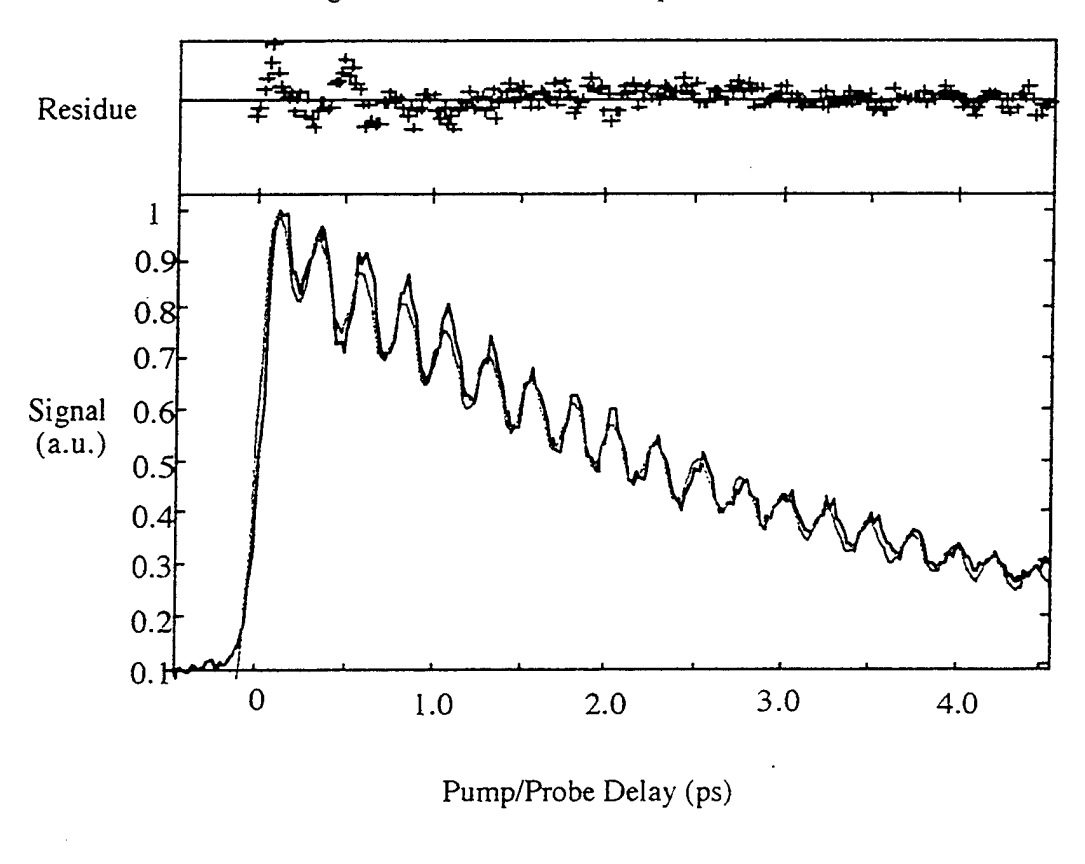
$$T = \frac{1}{\Delta E * c},$$

where c is the speed of light in cm/s. A full quantum mechanical model must be used to precisely fit the time evolution of the parent, but it can be closely modeled by a coherent double exponential decay:

[OCIO](t) = $\sigma_a \exp(-k_a t) + \sigma_b \exp(-k_b t) + 2\sqrt{\sigma_a + \sigma_b} \exp\{-(k_a + k_b)t \cos(\omega t + \phi)\}$, where σ_a and σ_b are the respective effective ionization cross sections for the two vibrational levels, k_a and k_b are the decay rate constants from the optically prepared OCIO* vibrational states, ω is the vibrational coherence frequency, and phase, ϕ .

A nonlinear least squares fit of the model convoluted with a Gaussian pulse of the measured cross correlation width is shown in figure 3.7, as well as the residue. The fit extends to 30 ps, but only the first 8 ps are shown for clarity. The best fit parameters for the O^{35} ClO isotope are $\tau_a = 4.2$ ps, $\tau_b = 2.0$ ps, $\omega = 137.9$ cm⁻¹, and $\phi = 160$ degrees. The measured frequency is very close to the predicted value of 137.6 cm⁻¹ obtained from the high resolution absorption data. Figure 3.8 displays the fit of the O^{37} ClO isotope, which has a slower quantum beat frequency because it is heavier. The agreement between the observed frequency and expected frequency is quite good.

Figure 3.7 Nonlinear least squares fit of O³⁵ClO



experimental data

nonlinear fit ——

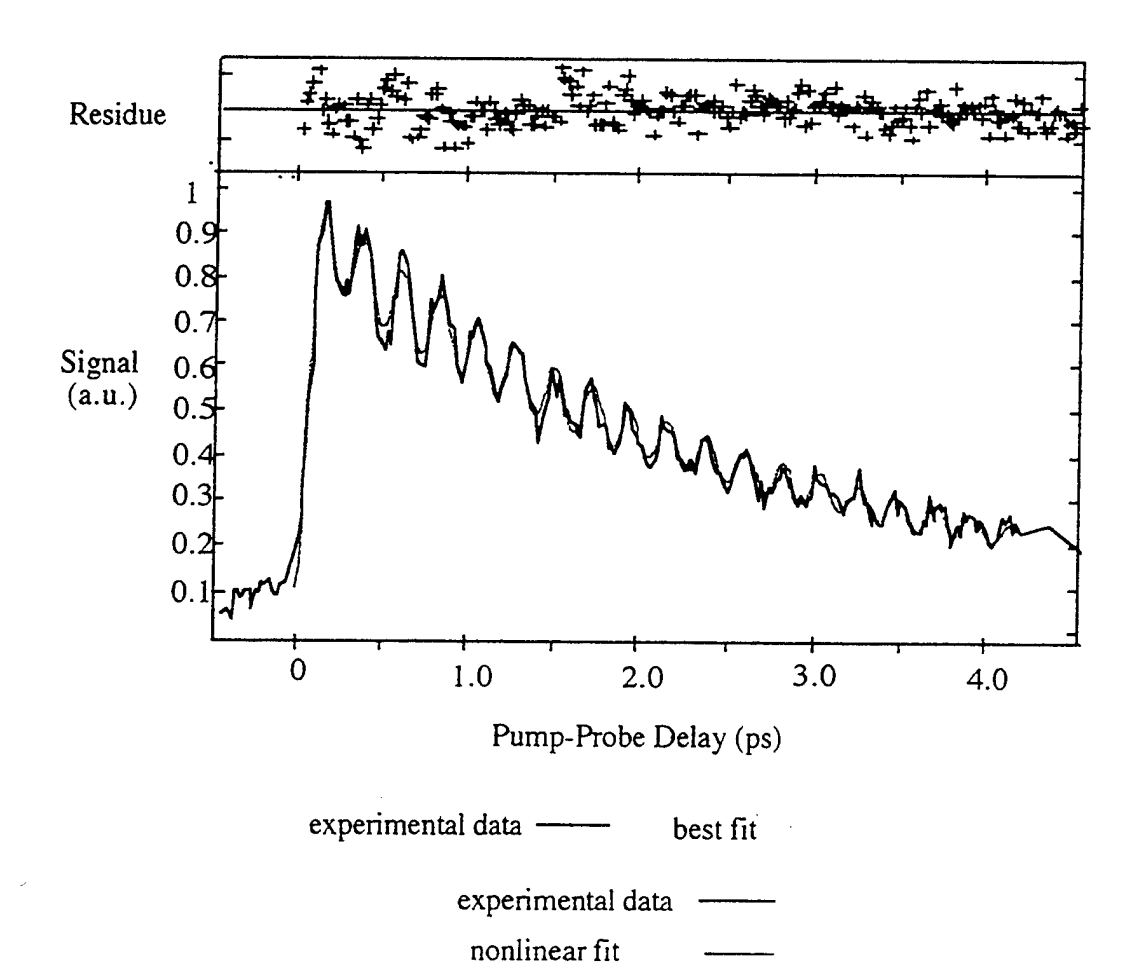
High Resolution Absorption Transitions (14):

$$X^{2}B_{1} \rightarrow A^{2}A_{2}$$
 (700) = 25832.2 cm⁻¹
 $X^{2}B_{1} \rightarrow A^{2}A_{2}$ (602) = 25969.8 cm⁻¹
 $\Delta E = 137.6$ cm⁻¹

Best Fit Parameters:

$$\tau_a = 4.2 \text{ ps}$$
 $\tau_b = 2.0 \text{ ps}$ $\omega = 137.9 + /- .4 \text{ cm}^{-1}$

Figure 3.8 Nonlinear least squares fit of O³⁷ClO



High Resolution Absorption Transitions (14):

$$X^{2}B_{1} \rightarrow A^{2}A_{2}$$
 (700) = 25798.8 cm⁻¹
 $X^{2}B_{1} \rightarrow A^{2}A_{2}$ (602) = 25932.9 cm⁻¹
 $\Delta E = 134.1 \text{ cm}^{-1}$

Best Fit Parameters:

$$\tau_a = 4.2 \text{ ps}$$
 $\tau_b = 2.0 \text{ ps}$ $\omega = 135 \text{ +/- 1 cm}^{-1}$

The data of the heavier isotope is noisier, but the best fit quantum beat frequency is within one cm⁻¹ of the predicted value. The measured t_a and t_b lifetimes, corresponding to the decays out of the (700) and (602) vibrational states of OClO*, are 50% shorter than the linewidth data. There is also discrepancy between the t_a and t₁ measured from the products. In the fits of both isotopes, there is a significant deviation from the experimental data at short delay (zero to 1000 fs). Both aspects can be accounted for in a multi-dimensional quantum mechanical model, but this simple model is sufficient to explain the quantum beats.

3.4 Conclusion

The photodissociation dynamics of OCIO have been studied near 3.2 eV excitation by time-resolved mass spectrometry. Upon excitation, the molecule dissociates through a two step mechanism: the optically prepared A 2 A₂ state crosses to an intermediate state in 4.6 ps, which subsequently dissociates in .25 ps. The identity of the intermediate state is a mixture of the dark 2 A₁ and 2 B₂ states. Contrary to previous experimental and theoretical work, the direct dissociation channel of the A 2 A₂ state is closed. A 240 fs quantum beat has been observed in the O^{3.5}ClO⁺ and O^{3.7}ClO⁺ species, which has been adequately described by a vibrational coherence on the pump-prepared A 2 A₂ state. The simple quantum beat model fits the data well from 1 ps to infinity, but a multi-dimensional quantum mechanical model is needed to fit all the details of the dynamics.

Future studies should investigate other excitation energies. The ability to find the onset for the direct dissociation channel may be hampered by the tunability of the laser system. These experiments were done at a pump wavelength of 385 nm, but it has been proven by experience that tuning to shorter wavelengths below 379 nm is extremely difficult, due to the drop off of the gain curve of the titanium:sapphire lasing medium. The tuning of the laser system to 400 nm is easily possible. The dynamics at this wavelength

are expected to be slower, but it would be interesting to see if the mixing of the two dark intermediates states separates at less excitation energies.

Further experiments should also include an unambiguous determination of the branching ratio. This can not be reported immediately because the absolute detection efficiency of each of the product species has not been determined. This can be done by the photodissociation of ClOCl, which has a single dissociation channel in the region of 3 - 3.5 eV (11):

$$ClOCl + h\nu_{pump} \rightarrow ClO(^2\Pi) + Cl(^2P)$$

A subsequent ionization of the probe would characterize the efficiencies of these two species. A determination of the efficiency of ground state O_2 was attempted by a probe only experiment:

$$O_2(^3\Sigma_g^-) + h\nu_{probe} \rightarrow O_2^+$$
.

A 2% mixture of O_2 :Ar was expanded through the source and ionized by a probe only experiment, but there was no resulting signal. This shows that all of the molecular oxygen detected in this experiment is from electronically excited. This is not surprising, however, because Davis and Lee have reported that 80% of the molecular oxygen detected is electronically excited, most likely in the $^1\Delta$ state (11). An efficiency of O_2 ($^1\Delta$) can be determined by first passing the O_2 :Ar mixture through a microwave discharge, which has been shown as an effective means of producing electronically excited molecular oxygen and atomic oxygen (23).

Chapter 3 References

- 1. M. J. Molina and F. S. Rowland, Nature 249, 810 (1974).
- 2. J. C. Farman, B. G. Gardiner, and J. D. Shanklin, Nature 294, 733 (1981).
- 3.a. P. Hamill and O. B. Toon, Physics Today 44, 34 (1991) and references therein.
 - b. J. G. Anderson, D. W. Toohey, and W. H. Brune, Science 251, 39 (1991).
 - c. W. H. Brune, J. G. Anerson, D. W. Toohey, D. W. Fahey, S. R. Kawa, R. L. Jones, D. S. McKenna, and L. R. Poole, Science 252, 1260 (1991).
- 4.a. A. A. Turnipseed, J. W. Birks, and J. G. Calvert, J. Phys. Chem. 95, 4356 (1991).
 b. A. J. Hills, R. J. Cicerone, J. G. Calvert, and J. W. Birks, Nature 328, 405 (1987).
- 5.a. S. Solomon, R. W. Sanders, and H. L. Miller, Jr., J. Geophys. Res. D. 95, 13,807 (1990). b. S. Solomon, R. W. Sanders, M. A. Carroll, and A. L. Schmeltekopf, J. Geophys. Res. D. 94, 11,393 (1989). c. S. Solomon, G. H. Mount, R. W. Sanders, and A. L. Schmeltekopf, Geophys. Res. Lett. 92, 8329 (1987).
- A. Wahner, R. O. Jakoubek, G. H. Mount, and A. R. Ravishankara, J. Geophys.
 Res. D. 94, 11,405 (1987).
- 7. S. P. Sander and R. R. Friedl, J. Phys. Chem. 93, 4764 (1989).
- 8. E. Ruhl, A. Jefferson, and V. Vaida, J. Phys. Chem. 94, 2990 (1990).
- 9.a. S. Solomon, Nature 347, 347 (1990).
 b. V. Vaida and J. Simon, Science 268, 1443 (1995).
- 10. E. Bishenden, J. Haddock, and D. J. Donaldson, J. Phys. Chem. 95, 2113 (1991).
- 11. H. F. Davis and Y. T. Lee, J. Chem. Phys. 105, 8142 (1996).
- 12. J. L. Gole, J. Phys. Chem. 84, 1333 (1980).

- 13.a. R. F. Delmdahl, S. Baumgartel, and K.-H. Gericke, J. Chem. Phys. 104, 2883
 (1996). b. S. Michielsen, A. J. Merer, S. A. Rice, F. A. Novak, K. F. Freed, and Y. Hamada, J. Chem. Phys. 74, 3089 (1981). c. A. Furlan, H. A. Scheld, and J. R. Huber, J. Chem. Phys. 106, 6538 (1997).
- E. Richard and V. Vaida, J. Chem. Phys. 94, 153 (1991).
 E. Richard and V. Vaida, J. Chem. Phys. 94, 163 (1991).
- K. A. Peterson and H.-J. Werner, J. Chem. Phys. 96, 8948 (1992). b. K. A.
 Peterson and H.-J. Werner, J. Chem. Phys. 99, 302 (1993).
- 16. K. A. Peterson and H.-J. Werner, J. Chem. Phys. 106, 6358 (1997).
- 17. M. Rose, M. Rosker, and A. H. Zewail, J. Chem. Phys. 88, 6672 (1988).
- 18.a. I. Fischer, M. J. J. Vrakking, D. M. Villeneuve, and A. Stolow, Chem. Phys. 207, 331 (1996).
 b. P. Ludowise, M. Blackwell, and Y. Chen, Chem. Phys. Lett. 258, 530 (1996).
 c. M. Blackwell, P. Ludowise, and Y. Chen, J. Chem. Phys. 107, 283 (1997).
- 19. R. I. Derby and W. S. Hutchinson, Inorg. Synth. 4, 152 (1953).
- 20. H. F. Davis, Ph. D. Thesis, University of California, Berkeley, 1992.
- 21. R. Flesch, E. Ruhl, K. Hottmann, and H. Baumgartel, J. Phys. Chem. **97**, 837 (1993).
- 22. J. L. Franklin and J. G. Dillard, ed., Nat. Stan. Ref. Data Ser. NBS26 (1969).
- 23.a. D. A. Shirley, ed., <u>Electron Spectroscopy</u>, Amsterdam, North-Holland, 1972, p 345-350. b. A.-L. Roche, K. Kirby, S. L. Guberman, and A. Dalgarno, J. Elec. Spec. 22, 223 (1981).

Chapter 4

The Photodissociation Dynamics of Chlorine Dioxide Studied by Time-resolved Photoelectron Spectroscopy

4.1 Introduction

Time-resolved mass spectrometry has been a powerful technique to study chemical reaction dynamics (1). It is an established method used to determine all of the species involved in a photodissociation, but does not determine the energies of the ions involved, and may be complicated by dissociative ionization. A complimentary technique is time-resolved photoelectron spectroscopy, in which the kinetic energy of the ejected electron indicates the electronic state of the ionized species (2). Because photoelectric transitions take place on the order of a few electric dipole oscillations, the ejected electron will be indicative of the parent ion, not of a fragment of dissociative ionization (2a). This chapter contains the time-resolved photoelectron spectroscopy (time-resolved PES) of chlorine dioxide, which is used in conjunction of the time-resolved mass experiments of chapter 3 to gain a better understanding of the photochemical dynamics of this atmospherically important molecule.

The time-resolved mass measurements of chapter 3 described the dynamics of chlorine dioxide near 3.2 eV as an indirect two step dissociation. Upon excitation to the A 2 A₂ state, the molecule crosses to an intermediate state in 4.6 ps, which subsequently dissociates in .25 ps:

$$OCIO + hv_{3.2 \text{ eV}} \rightarrow OCIO^* (A^2A_2) \rightarrow OCIO^{\dagger} \rightarrow CIO, CI, O, O_2.$$

The intermediate state, OClO[†], is a mixture of the dark ²A₁ and ²B₂ states. There were two different sources of the product ions: ionization of OClO[†] leads to electronically excited OClO⁺, which is unstable and spontaneously dissociates to product ions and a direct ionization of the neutral products. The time-resolved PES of OClO will identify the electronic states of OClO⁺, and show that the dissociative ionization is important in understanding the mass results.

Time-resolved PES will also shed light on one of the most controversial aspects of OCIO photodissociation, namely the branching ratio of the dissociation channels. OCIO been shown to be extremely important in the stratospheric ozone depletion budget (section 3.0). A number of groups have shown that two reactions are open (3):

OCIO (X
$${}^{2}B_{1}$$
)+ hv \rightarrow OCIO* (A ${}^{2}A_{2}$) \rightarrow CIO (${}^{2}\Pi$) + O (${}^{3}P$) [1]

$$\rightarrow Cl (^{3}P) + O_{2} (^{3}\Sigma_{g}^{+}, ^{1}\Delta, ^{1}\Sigma_{g}^{+})$$
 [2]

Reaction [1] does not contribute to stratospheric ozone depletion, but reaction [2] increases the net CI concentration in the stratosphere, which leads to ozone destruction. It has been thought that a 10% yield of [2] to [1] would significantly alter the ozone budget (4).

Bishenden and Donaldson measured the branching ratio of reaction [2]:[1] to be a maximum of 15% at 360 nm (5). This was done by photolysis and a subsequent resonance-enhanced multi-photon ionization (REMPI) probe of the ClO and Cl fragments. In a different experiment, Davis and Lee measured the branching ratio to be a maximum of 3.9% at 404 nm, with negligible amounts at wavelengths shorter than 380 nm (6). This was done by photofragment translational energy spectroscopy, which detects the ClO, Cl, O, and O_2 products by a softer ionization method that minimized dissociative ionization.

In this experiment, excitation of a 387 nm pump pulse (3.2 eV), two probe photons at 257 nm (4.8 eV) are needed to ionize the OCIO species to the ground state of the OCIO⁺ ion and three photons are necessary to ionize each of the products. The signal at infinite

delay is dominated by three photon ionization of ClO⁺. It will be shown that there is a four photon probe ionization of ClO to an electronically excited ClO⁺ state, which is dissociative:

$$ClO + 2h\nu_{probe} \rightarrow ClO^* + 2h\nu_{probe} \rightarrow ClO^+\,(^1\Pi) \rightarrow Cl^+ + O.$$

This may explain why there is such a large discrepancy between the previous branching ratio measurements. The REMPI experiment requires high laser powers that could access this state. The resulting Cl yield would be an artifact of the detection scheme.

A comparison of the mass and photoelectron data will follow. The seemingly contradictory results of the two experiments will be resolved.

4.2 Experimental

The experimental apparatus is discussed in depth in chapter 2. The experimental conditions were the same as in the time-resolved mass measurements in section 3.1, with a few exceptions. Briefly, the femtosecond pump and probe pulses of 387 nm and 257 nm, respectively, were produced by a Titanium:sapphire oscillator and regenerative amplifier operating at 772 nm and 3.2 kHz repetition rate. The pump was one half of the second harmonic output of the laser frequency doubled in a .300 mm BBO crystal. The remaining second harmonic and residual fundamental were mixed in another .300 mm thick BBO crystal optimized for third harmonic generation. The maximum pump pulse energy obtainable was 50 µJoules/pulse, but was attenuated to 6 µJoules/pulse to ensure 1 photon absorption of the pump to the A 2A2 state of interest. The typical probe output was 13 Woules/pulse, but was attenuated to less than 6 Woules/pulse to minimize high power effects (7). The typical time response of the laser system is 120 +/- 20 fs measured by the pump/probe cross correlation measured after the exit window of the molecular beam chamber. The probe polarization was parallel to the photoelectron flight direction to maximize the collection efficiency of the angular dependence of the photoelectric effect (8). The pump polarization was maintained to be horizontal because of the method used to

measure the pump/probe cross correlation by difference frequency generation in a KDP nonlinear crystal after the exit window. A Stanford Research Systems SR-540 optical chopper was used to subtract of the probe-only background on a shot-to-shot basis.

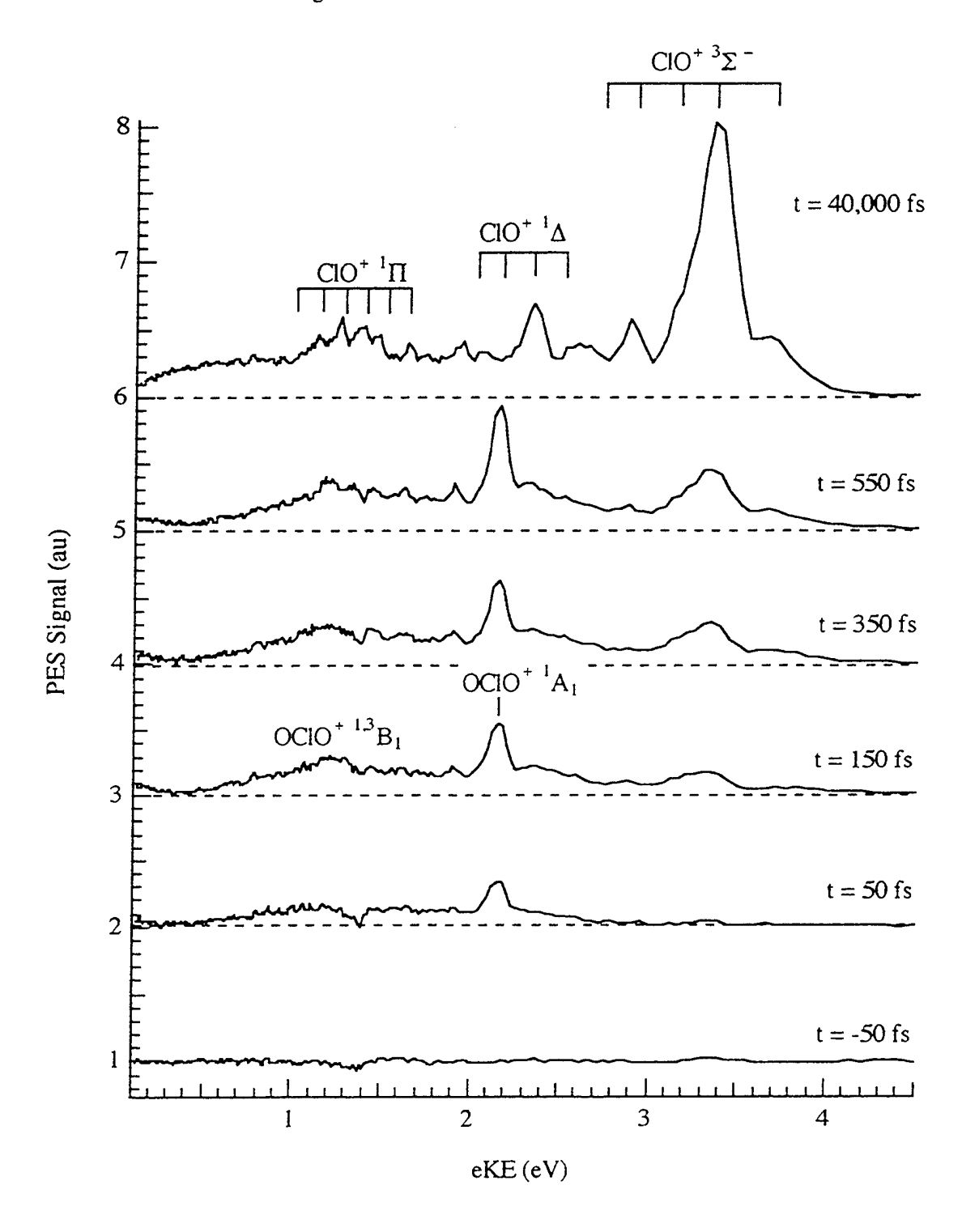
The experiments were done in a continuous molecular beam vacuum chamber and time-of-flight photoelectron spectrometer. A dilute mixture of OCIO in argon was expanded through a .100 mm diameter aperture, skimmed twice, and entered an ionization chamber 18 cm downstream. As the molecular beam enters the interaction area, it absorbs a single pump photon and is subsequently ionized by two or more probe photons. The ejected photoelectrons are collected by a microchannel plate detector 15 cm away in a doubly magnetically shielded flight tube in which the ion optics used for the mass experiments are removed. Conceptually, the ion optics could remain in the photoelectron flight tube if they could be electrically grounded to maintain a field-free region, but small stray potentials (~1 V) on the optics would prohibit reliable data collection. Baffles in the flight tube ensured collection of a point source of electrons of approximately 1 mm³ volume. To ensure an accurate energy calibration the fs PES of nitric oxide, NO, and xenon were acquired in the exactly the same experimental conditions. The data was acquired by a 486 66 Mhz computer, and later transferred to a 166 Mhz Pentium computer for analysis.

Due to the fact that the expected photoelectron signal is a factor of 1000 times less than that of the mass, the data was collected in the single-particle counting regime (9). This required the collection of thousands of laser shots to ensure a statistically valid photoelectron spectrum. Typical delay scans consisted of 320000 shots at a given pump/probe, with at least 6 delay steps. This was repeated at least 10 times for reproducibility.

4.3 Results and Discussion

The typical fs PES data of OCIO photodissociation is shown in figure 4.1. The six different spectra correspond to six different pump/probe delays.

Figure 4.1 Time-resolved PES of OCIO



At delay = -50 fs, there is no signal. After zero delay, a sharp peak begins to grow in at 2.15 eV, as well as a broad diffuse band centered at 1.23 eV. Both of these features are assigned to different electronic states of the OClO⁺ ion. Both features are not present at 40 ps, which is dominated by a number of peaks that are assigned to different electronic states of the ClO⁺ ion. A detailed discussion of the assignment at short delay time and at 40 ps delay will follow.

4.31 Short Pump/Probe Delay Assignment

The assignment at short delay time was done from the definition of the photoelectric effect, in which the photoelectron kinetic energy, eKE, is a function of the total photon energy, hv_{total}, and ionization potential, I.P. (2a, 8):

$$eKE = hv_{total} - I.P.$$

One would expect the spectra to be dominated by the time-dependent Franck-Condon factors of the molecule on the excited states and the ion states. Therefore, one would observe a time-dependent vibrational progression as the molecule dissociates on the OCIO* and OCIO* states. This is complicated by an accidental resonance of 1 pump + 1 probe on a high lying Rydberg state, OCIO**, which converges to the first ionization potential. Upon absorption of a subsequent photon, the molecule is ionized:

$$OClO + h\nu_{pump} \rightarrow OClO^* + h\nu_{probe} \rightarrow OClO^{**} + h\nu_{probe} \rightarrow OClO^+ (X\ ^1A_1)$$

The ion vibrational progression is thus dominated by a single peak, because the Franck-Condon factors between the Rydberg state and the ion state are essentially unity for $\Delta v=0$ transitions and zero for all others. This is due to the negligible geometry change between the Rydberg state and the ion state, as described in section 2.6. At the pump and probe energies used in this experiment, 1 pump + 1 probe is on resonance with the $4p_x^{\ \Pi} \ v_{210}$

Rydberg state, where v_{210} correspond to vibrational excitation of two quanta in the

symmetric stretch and one quantum of bend (10). The resulting photoelectron spectrum has a prominent peak of $OClO^+$ (X 1A_1 , v_{210}). Table 4.1 displays the pertinent data in assigning the 2.2 eV peak. Figure 4.2 displays a zoomed in spectrum at delay = 150 fs to show that the expected eKE value is in excellent agreement with the predicted value.

Table 4.1 Assignment of 2.156 eV Peak

$$h\nu_{pump} = 3.204 + /-.021 \text{ eV} \qquad h\nu_{probe} = 4.806 + /-.031 \text{ eV}$$

$$h\nu_{pump} + h\nu_{probe} = 8.010 + /-.052 \text{ eV}$$

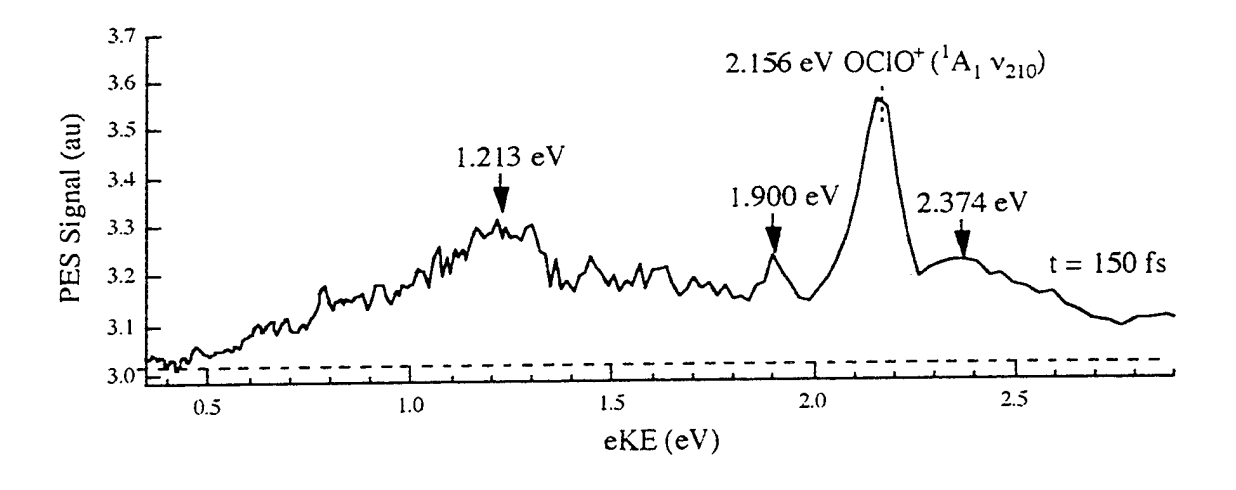
$$h\nu_{pump} + 2h\nu_{probe} = 12.816 + /-.083 \text{ eV}$$

$$OCIO(X^{2}B_{1}) \rightarrow OCIO^{**}(4p_{x}^{H}\nu_{210}) 7.969 \text{ eV} (10)$$

$$I.P. (X^{1}A_{1}, \nu_{210}) = 10.660 \text{ eV} (10)$$

$$eKE = h\nu_{total} - I.P. = 2.156 \text{ eV}$$

Figure 4.2 Time-resolved PES of OCIO Photodissociation at 150 fs Delay



There are other features in the time-resolved PES data at short time delay. The feature labeled by the arrow at 2.374~eV is a ClO⁺ peak that is beginning to grow in at this delay. There is also a small peak at 1.900~eV which follows the behavior of the 2.156~eV peak. This is probably another resonance enhanced peak of a different Rydberg state that leads to ionization to the OClO⁺ 1 A₁ state. Since the pump and probe pulse have a large bandwidth, a 1 probe + 1 probe resonant scheme from the A 2 A₂ state is nearly on resonance with different vibrational levels D and E states observed by VUV absorption spectroscopy (11). Such Rydberg states have either 3 quanta of asymmetric stretch or 5 quanta of bend, which is nearly .5 eV of internal energy. This 1.900 eV peak would correspond to an OClO⁺ 1 A₁ with .571 eV internal energy. Such a state has not been characterized by the modern Helium I PES (10), but the $\Delta v = 0$ rule would predict that much vibrational excitation in the ion.

The peak labeled by the arrow at approximately 2.4 eV is a ClO⁺ state is beginning to grow in at this delay. The arrow at about 1.2 eV is also partly due to the structured band of ClO⁺ growing in, but the shape at 150 fs delay is different from 40 ps, as seen in figure 4.1. This is due ionization from the intermediate state, OClO⁺. This state is a mixture of the dark ²A₁ and ²B₂ states. Ionization from these states lead to electronically excited states of the ion. This can be justified by considering the molecular orbitals of the neutral and ionic states. Following the treatise by Peterson and Werner (12) the following MO's of the ground and excited states of the neutral are:

The lowest states of the ion correspond to removal of a 3b₁ electron of the neutral. The resulting MO's and experimentally determined adiabatic ionization potentials (10) are:

$$\begin{aligned} &\text{OCIO}^+ \text{ X }^1 \text{A}_1 & \dots (5b_2)^2 \ (8a_1)^2 \ (1a_2)^2 \ (3b_1)^0 & \text{I.P.}_{ad} = 10.345 \ \text{eV} \\ &\text{OCIO}^+ \ ^{3.1} \text{B}_1 & \dots (5b_2)^2 \ (8a_1)^1 \ (1a_2)^2 \ (3b_1)^1 & \text{I.P.}_{ad} = 12.400, \ 12.440 \ \text{eV} \\ &\text{OCIO}^+ \ ^{3.1} \text{A}_2 & \dots (5b_2)^1 \ (8a_1)^2 \ (1a_2)^2 \ (3b_1)^1 & \text{I.P.}_{ad} = 13.330, \ 13.500 \ \text{eV} \\ &\text{OCIO}^+ \ ^{3.1} \text{B}_2 & \dots (5b_2)^2 \ (8a_1)^2 \ (1a_2)^1 \ (3b_1)^1 & \text{I.P.}_{ad} = 12.870, \ 15.250 \ \text{eV} \end{aligned}$$

The expected eKE's from ionization of the B₁, A₂, and B₂ states do not yield the experimentally determined values, because the total photon energy available is only 12.816 eV (10). Baumgertel et al. have also determined the fragmentation threshold of OClO⁺ to be 13.5 eV. If three probe photons are used to ionize the intermediate state, then a higher electronic state of ³B₁ symmetry can be accessed. The corresponding M.O. for this state is:

$$OClO^{+3.1}B_{2} - ...(6a_{1})^{2}(7a_{1})^{1}(2b_{1})^{2}(5b_{2})^{2}(8a_{1})^{2}(1a_{2})^{2}(3b_{1})^{1} - I.P._{ad} = 16.1, 17.1 \text{ eV},$$

which involves the removal of an electron from the 7a₁ orbital. This is possible only by an electron rearrangement, which has been used to explain some of the bands in the He I PES of OCIO (10.b). The strict selection rules for the multi-photon ionization from the intermediate state are relaxed because it is known from the mass experiments in chapter 3 that the intermediate state is a highly mixed state of the ²A₁ and ²B₂ states. The He I PES of OCIO has determined this state's adiabatic ionization potential to be near 16.1 eV, but has no distinct vibrational structure. This is thought to be because this state spontaneously dissociates. The peak in the experimental spectrum at 1.2 eV does correspond to an unassigned feature at an ionization potential of 16.4 eV in the He I PES of McDowell et al (10.b). The total photon energy of 1 pump + 3 probe is 17.622 eV, The resulting eKE of 1.2 eV matched the experimental feature at 1.2 eV.

4.32 40 ps Delay Assignment

The assignment at 40 ps delay was done in the same manner, except that the species that can be ionized are the ground electronic states of the ClO, Cl, O, and the lowest three states of O_2 . Figure 4.3 displays the pump/probe PES at 40 ps delay.

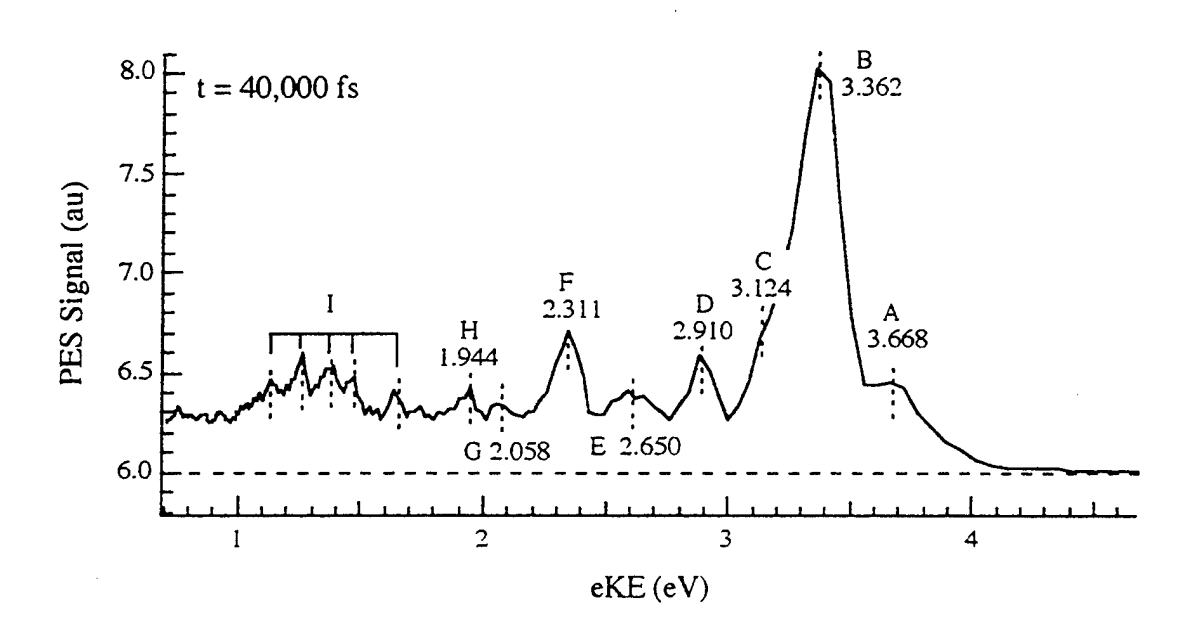


Figure 4.3 fs PES of OCIO Photodissociation at 40 ps Delay

All of the features are assigned to different electronic states of the ClO⁺ ion. It is interesting to note that no features have been assigned to the Cl, O, and O_2 products, even though there were appreciable amounts of Cl⁺, O⁺, and O_2 ⁺ in the mass experiments. This is due to a number of reasons. Foremost, there are many accidental two photon probe resonances that lead to a large three photon ionization signal:

$$\text{CIO}\,(^2\Pi) + 2h\nu_{\text{probe}} \rightarrow \text{CIO*} + h\nu_{\text{probe}} \rightarrow \text{CIO*}.$$

The electronically excited ClO* state is any one of the F, G, H, or higher unassigned Rydberg states (13). Many resonances occur because of the broad bandwidth of the probe laser can access any of these states in which there is a high density of electronic states (13).

There are no such resonances for the other fragments. The nonresonant ionization signal of the other fragments are probably present in the diffuse background of the spectrum at 40 ps, but are washed out by the larger resonant ClO⁺ species. The dashed lines in figures 4.1, 4.2, and 4.3 refer to the data baseline, which shows that there is a very broad diffuse signal that is the largest at 40 ps delay.

There could also be a contribution from the angular dependence of the photoelectric effect. All of the spectra reported were acquired by a vertically polarized probe laser, which should maximize the collection efficiency (2a, 8). Yet, if there was an anisotropic distribution of electrons, (i.e. $\beta = 2$), then the collection efficiency would be decreased. This can be alleviated by using a different polarization of the probe laser. An attempt was made to acquire the time-resolved PES spectra with a vertically polarized pump and horizontally polarized probe, but no significant changes to the PES spectra were observed.

A more compelling reason is dissociative ionization of ClO:

$$ClO^+(^3\Pi) \rightarrow Cl^+ + O$$
,

which would explain such a large Cl⁺ mass signal. The PES spectra, however, would be indicative of ClO⁺ state that dissociates. The majority of the PES spectra can be assigned by direct ionization, but dissociative ionization is important. This will be considered momentarily.

The assignments are based on the known VUV absorption spectroscopy (13) and the known photoelectron spectroscopy of ClO (14). Figure 4.4 shows the relevant molecular orbital diagram for ClO. The ground electronic state has an unpaired electron in an anti-bonding Π orbital. The ground state is $X^2\Pi_{3/2,1/2}$, which has a vibrational frequency of .106 eV. Ionization of a 3π electron leads to three different ionic states: $X^3\Sigma^2$, Δ^2 , and Δ^2 , all of which are bound. Ionization of a Δ^2 electron leads to six different electronic states, none of which correspond to any of the time-resolved PES peaks. The

corresponding M.O.'s, of the three lowest states of the ion with their corresponding ionization potentials vibrational frequencies are listed in figure 4.5.

Figure 4.4 ClO Molecular Orbital Diagram of ClO

Figure 4.5 Molecular Orbital Diagrams of the Three Lowest ClO+ States

$$\frac{1}{4}$$
 $\frac{1}{4}$ $\frac{1}{3}$ $\frac{1}{4}$ $\frac{1}{4}$ $\frac{1}{3}$ $\frac{1}{4}$ $\frac{1}{4}$ $\frac{1}{2}$ $\frac{1}{4}$ $\frac{1}{4}$ $\frac{1}{2}$ $\frac{1}{4}$ $\frac{1$

The three lower states of the ion are stable because the removal of the anti-bonding 3π electron increases the bond strength.

The Rydberg resonances involved, which have been observed by VUV high resolution absorption (13) and multi-photon PES (14, 15) are listed in Table 4.2. The photoelectron assignments are given in Table 4.3. It has been shown that the H and F states correlate to the $^{1}\Sigma^{-}$ state of the ion, and the G state correlates to the $^{1}\Delta$ state of the ion (15). The $^{1}\Sigma^{+}$ state is energetically accessible, but is not observed, probably because of a lack of an enhancement of a Rydberg state that correlates to it. Likewise, there are no assignments to ion states that result from 2π ionization. The strongest peaks in the experimental spectrum are those from v = 1 of neutral ClO. This is expected because it has been shown that the 40% of the CIO produced at 3.2 eV photolysis is produced in the v=1 state, 20% is in v=0 (6). There are many unassigned resonances that are within the bandwidth of 2 probe photons, and there are many more which are nearly in resonance. The probe pulse is Gaussian in shape, and the listed +/- width refers to the full-width at half peak height. There is still intensity of the probe outside of this value, which means that states nearby the 2 probe energy can be important. It is very difficult to predict what the intensity pattern of these resonances would have on the PES spectrum, especially on the states that are near resonance.

Table 4.2 Assigned and Unassigned Rydberg States that Enhance Ionization

9.680 eV (unassigned)	9.631 eV (unassigned)
9.590 eV (unassigned)	9.579 eV (unassigned)
9.558 eV G(v=3)	9.455 eV H(v=2)
9.416 eV F(v=6)	9.300 eV (unassigned)

Table 4.3 CIO Resonance Enhanced 2+1 Probe Ionization PES

$$hv_{probe} = 4.806 + -.031 \text{ eV}$$
 $eKE_{exp} = expected \text{ eKE}$ $eKE_{obs} = observed \text{ eKE}$

A.
$$CIO(X^{2}\Pi, v=1) + 2 hv_{probe} \rightarrow CIO^{**}(?) + 1 hv_{probe} \rightarrow CIO^{+}(X^{3}\Sigma^{-}, v=0)$$

I.P. = 10.781 eV eKE_{exp} = 3.637 eV eKE_{obs} = 3.668 eV error = -.031 eV

B.
$$CIO(X^{2}\Pi, v=1) + 2 hv_{probe} \rightarrow CIO^{**}(H, v=2) + 1 hv_{probe} \rightarrow CIO^{+}(X^{3}\Sigma^{-}, v=2)$$

I.P. = 11.039 eV eKE_{exp} = 3.379 eKE_{obs} = 3.362 error = .017

C. CIO (X
$${}^{2}\Pi$$
, v=0) + 2 hv_{probe} \rightarrow CIO** (?) + 1 hv_{probe} \rightarrow CIO* (X ${}^{3}\Sigma$, v=3)
I.P. = 11.274 eV eKE_{exp} = 3.144 eKE_{obs} = 3.124 error = .020

D. CIO (X
$${}^{2}\Pi$$
, v=0) + 2 hv_{probe} \rightarrow CIO** (F, v=5) + 1 hv_{probe} \rightarrow CIO⁺ (X ${}^{3}\Sigma$, v=5)
I.P. = 11.532 eKE_{exp} = 2.886 eKE_{obs} = 2.910 error = -.024

E.
$$CIO(X^2\Pi, v=0) + 2 hv_{probe} \rightarrow CIO^{**}(?) + 1 hv_{probe} \rightarrow CIO^{+}(^1\Delta, v=0)$$

I.P. = 11.750 eV eKE_{exp} = 2.668 eKE_{obs} = 2.650 error = .018

F.
$$CIO(X^2\Pi, v=0) + 2 hv_{probe} \rightarrow CIO^{**}(G, v=3) + 1 hv_{probe} \rightarrow CIO^{+}(^{1}\Delta, v=3)$$

I.P. = 12.131 eV eKE_{exp} = 2.289 eKE_{obs} = 2.311 error = -.022

G.
$$CIO(X^2\Pi, v=0) + 2 hv_{probe} \rightarrow CIO^{**}(?) + 1 hv_{probe} \rightarrow CIO^{+}(^1\Delta, v=5)$$

I.P. = 12.385 eV eKE_{exp} = 2.033 eKE_{obs} = 2.058 error = -.025

H.
$$CIO(X^2\Pi, v=0) + 2 hv_{probe} \rightarrow CIO^{**}(F, v=6) + 1 hv_{probe} \rightarrow CIO^{+}(^{1}\Delta, v=6)$$

I.P. = 12.385 eV eKE_{exp} = 2.033 eKE_{obs} = 2.058 error = -.025

The remaining feature of the 40 ps spectrum is the vibrational progression labeled by I. This must be either ClO or O_2 . A four photon probe ionization can reach the ${}^3\Pi$ state of ClO⁺. This arises from ionization of a 7 σ electron, and its corresponding M.O. is shown in Figure 4.7. This has been characterized by He I PES (14) to be a diffuse band with a small amount of vibrational structure. This is thought to be dissociative

$$ClO^+(^3\Pi) \rightarrow Cl^+ + O$$
,

because of the weakening of the sigma bond upon removal of the electron. This is the main source of Cl⁺ observed in the mass experiment. The previous vibrational structure does match the vibrational progression of the observed band at 1.5 eV. The electron integrated signal of this band does follow the evolution of the 3.6 eV ClO⁺ peak.

Figure 4.6 M.O. of the ³Π state of ClO⁺

The molecular oxygen signal is expected to be very small because the mass signal show that O_2^+ signal is 20 times less than ClO^+ (figure 3.4). The absence of molecular oxygen may also be due to a lack of resonance enhancement. The mass experiments of chapter 3 have proved that the experiment is insensitive to ionization of ground state oxygen. A 2% O_2 :Ar molecular beam was expanded into the molecular beam spectrometer

under identical conditions of the OCIO probe-only experiment to determine the detection efficiency of O_2^+ , but no ion signal from O_2^+ or O^+ was found. This is somewhat expected, because the photofragment experiments showed that 80% of the O_2 is electronically excited, probably in the $^1\Delta$ state (6). The He I PES of molecular oxygen in the $^1\Delta$ state has been obtained (16) by first passing O_2 through a microwave discharge before entering the PES spectrometer. The M.O.'s of three lowest electronic states of the neutral are listed in figure 4.7.

Figure 4.7 Molecular Orbital Diagram of O₂

Three bands due to this state were observed: ${}^2\Pi$ (I.P. = 11.086 eV, we=.232 eV), ${}^2\Phi$ (I.P. = 18 eV), and ${}^2\Delta$ (I.P. = 19 eV), which are weak and do not correspond to any of the observed features. No experimental work has been done on the PES of O_2 (b ${}^1\Sigma_g$), but the expected spectra can be determined from the O_2 (${}^3\Sigma_g$) PES (17). The expected PES bands are listed in Table 4.4.

Table 4.4 Expected eKE's of O₂ PES

Transition	I.P. (eV)	$\omega_{e}(eV)$	eKE (eV)
$O_2(^1\Delta) \rightarrow O_2^+(X^2\Pi)$	11.086	.232	3.33
$O_2(^1\Sigma_g^-) \rightarrow O_2^+(X^2\Pi)$	10.436	.232	3.98
$O_2(^1\Sigma_g^-) \rightarrow O_2^+(a^4\Pi)$	14.481	.128	4.753 (4 hv)
$O_2(^1\Sigma_g^-) \rightarrow O_2^+(A^2\Pi)$	15.402	.111	3.822 (4 hv)
$O_2(^1\Sigma_g^-) \rightarrow O_2^+(b^4\Sigma)$	16.535	.148	2.689 (4 hv)

A justification of the absence of Cl and O can been seen in the known He I PES (10.b, 18) and atomic emission spectra (19) of these atoms. This is quite surprising for Cl especially, because of the strong Cl⁺ ion signal observed in the mass experiments of chapter 3. Figure 3.4 shows that at 6 ps pump/probe delay, the Cl⁺ signal is only about 1/3 the size of the ClO⁺ signal. If all of the Cl signal arose from ionization of neutral Cl, then there should be a corresponding PES peak. Since there is not, then the Cl⁺ must arise from dissociative ionization of ClO. The absence of the direct ionization signal may also be due to a lack of 1 or 2 photon resonances of Cl or O nearby to enhance ionization. A three probe transition can directly access the lowest ionic states, but the expected eKE's of those states do not match any of the observed features in figure 4.3. Table 4.5 illustrates this point.

Table 4.5 Expected PES Spectra for Cl and O

Cl ground state: ${}^{2}P_{3/2}$ electronic configuration: $1s^{2} 2s^{2} 2p^{6} 3s^{2} 3p^{5}$

Cl⁺:	state	electronic configuration	I.P (eV)	expected eKE (eV)
	${}^{3}P_{2}$	3p ⁴	13.017	1.401
	$^{3}P_{1}$	3p ⁴	13.103	1.315
	$^{3}P_{0}$	3p ⁴	13.140	1.278
	¹ D ₂	3p ⁴	14.462	4.762 (4 hv)
	¹S	3p ⁴	16.476	2.748 (4 hv)

O ground state: ³P

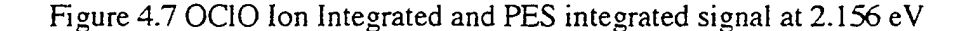
electronic configuration: 1s² 2s² 2p⁴

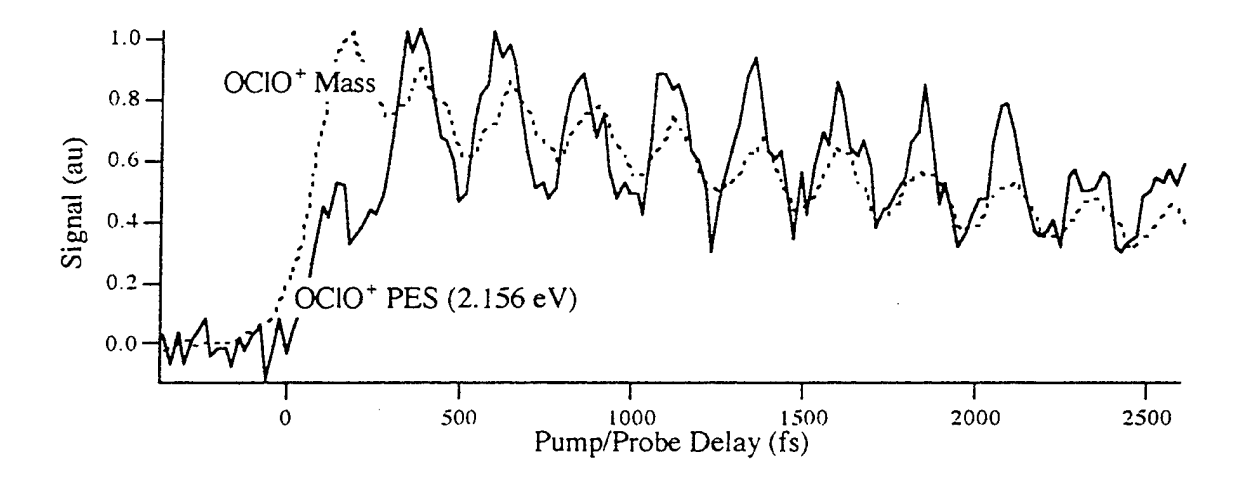
O⁺:	state	electronic configuration	I.P (eV)	expected eKE (eV)
	⁴S	2p³	13.62	.80
	²D	2p³	16.96	2.26 (4 hv)
	² P	2p³	18.63	.59 (4 hv)

4.33 Comparison of time-resolved Mass and Photoelectron Results

Some interesting comparisons can be done between the time-resolved mass and PES data. It is known from the mass experiments in chapter 3 that the OCIO* state has a time evolution of sharp rise at zero delay time, and a 240 fs quantum beat superimposed on top of a biexponential decay. The quantum beats are due to the fact that the pump pulse has enough bandwidth to simultaneously excite two vibrations of the A 2 A₂ state. A

nonstationary superposition of these vibrations oscillate with a period dependent on the difference in energy between the two vibrational levels. An oscillation is expected in the PES because there should be a change in the overlap of the wavefunction on the A 2 A₂ state and the OClO** $4p_x^{\Pi}$ state as this nonstationary state oscillates on the A 2 A₂ state. Figure 4.7 shows both the mass integrated ion signal and photoelectron integrated signal at 2.156 eV as a function of pump/probe delay. Even though the signal/noise ratio of the PES data is not as good as the mass, an interesting comparison can be made. The oscillation in the PES has the same period and phase as the signal, but has a different shape at short delay time. This is due to subtleties in the quantum mechanics that can only be described by a multi-dimensional quantum mechanical simulation. This was mentioned in chapter 3 in regards to the inability to fit the mass data at short delay times by the simple coherent biexponential decay model.

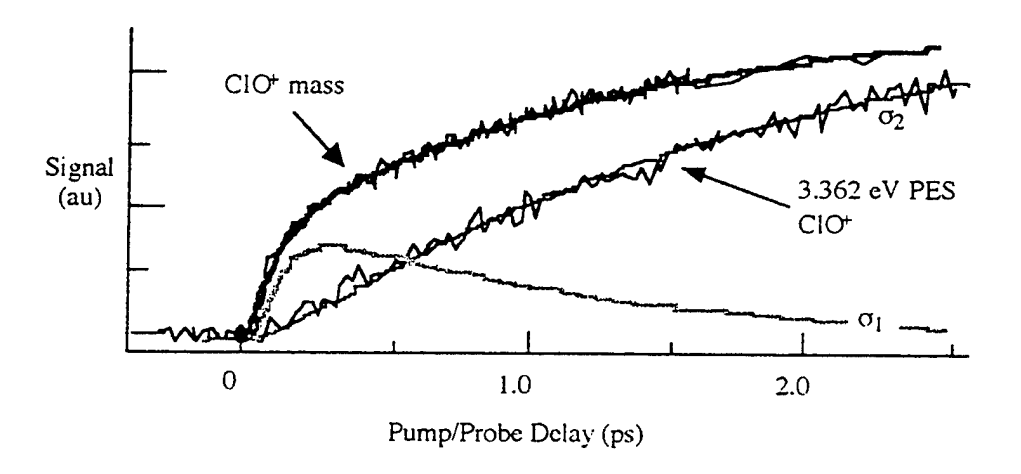




A comparison of the CIO+ mass and PES data is also interesting. At first inspection, it appears as if the mass and PES data are not in agreement. The electron integrated time evolution of the largest peak at 3.362 eV is an exponential rise, which is predicted from the

dissociation model, which does not match the best fit of the ClO⁺ mass data. To properly fit the mass data, however, two sources of product ions must be included. The two terms of the mass fitting function were (section 3.2.1.): σ_1 , which is the dissociative ionization of the OClO[†] state, and σ_2 , which is the direct ionization of the neutral product. The integrated PES data will reflect the direct ionization of ClO. Figure 4.8 displays the comparison of the mass integrated and electron integrated spectra. The PES is in excellent agreement with the direct ionization term of the mass data. The seemingly contradictory data are in agreement.

Figure 4.8 Electron Integrated PES 3.362 eV peak Compared to CIO+ Mass Data



4.4 Conclusion

In summary, time-resolved PES has been used to gain a better understanding of the photodissociation dynamics of OCIO near 3.2 eV excitation. At early pump/probe delay, two electronic states of OCIO⁺ have been observed, one of which is above the fragmentation threshold and dissociates to product ions. This is very supportive of the two-step dissociation model derived from the mass experiments in section 3.2.1. At long delay, CIO⁺ is observed in a variety of electronic states, one of which is dissociative to Cl⁺ + O. Therefore, the Cl⁺ ion observed in the time-resolved mass experiments is from

dissociative ionization. This has some serious implications in experiments attempting to determine the branching ratio. The REMPI detection scheme of Bishenden and Donaldson may be hampered by this effect. The branching ratio of Davis and Lee is probably more accurate, because of their low laser powers and detection scheme.

Unfortunately, no molecular oxygen was detected in the PES experiments. Experimental and theoretical works have implied that the O₂ produced is electronically excited, but the identity could not be determined. A future experiment concerns tuning the laser wavelength to 404 nm, where the maximum amount of molecular oxygen was produced (6). Time-resolved PES spectroscopy is an ideal method to determine the identity of the electronic states of these ions.

Chapter 4 References

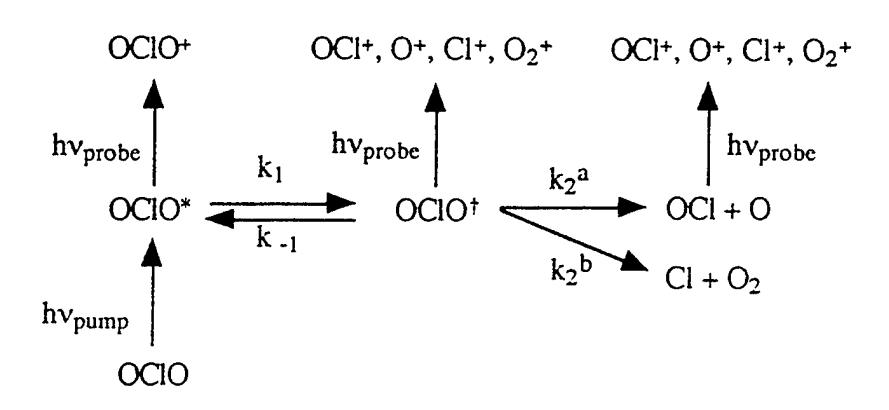
- M. Dantus, M. H. M. Janssen, A. H. Zewail, Chem. Phys. Lett. 181, 281 (1991).
 S. A. Trushia, W. Fuss, T. Schikarskirt, W. E. Scmid, et al, J. Chem. Phys.
 106, 9386, (1997). c. V. Engel, T. Baumert, Ch. Meier, and G. Gerber, Z. Phys. D
 28, 37 (1993). d. T. Baumert, J. L. Herek, and A. H. Zewail, J. Chem. Phys. 99, 4430 (1993).
- J. Berkowitz, Photoabsorption, Photoionization, and Photoelectron Spectroscopy,
 New York, Academic Press, 1979. b. D. R. Cyr and C. C. Hayden, J. Chem. Phys.
 104, 771 (1996). c. B. J. Greenblatt, M. T. Zanni, and D. M. Neumark, Science
 276, 1675 (1997). d. I. Fischer, M. J. J. Vrakking, D. M. Villeneuve, and A.
 Stolow, Chem. Phys. 207, 331 (1996). e. P. Ludowise, M. Blackwell, and Y.
 Chen, Chem. Phys. Lett. 258, 530 (1996).
- 3. V. Vaida and J. D. Simon, Science 268, 1443 (1995).
- 4. S. Solomon, Nature **347**, 347, (1990).
- 5. E. Bishendon, J. Haddock, and D. J. Donaldson, J. Phys. Chem. 95, 2113 (1991).
- 6. H. F. Davis and Y. T. Lee, J. Chem. Phys. 105, 8142 (1996).
- A. Zavriyev, I. Fischer, D. M. Villeneuve, and A. Stolow, Chem. Phys. Lett. 234, 281 (1995).
 b. M. Blackwell, P. Ludowise, and Y. Chen, J. Chem. Phys. 107, 283 (1997).
 c. P. Ludowise, M. Blackwell, and Y. Chen, Chem. Phys. Lett. 258, 530 (1996).
- 8. R. E. Ballard, <u>Photoelectron Spectroscopy and Molecular Orbital Theory</u>, New York, John Wiley and Sons, 1978.
- 9.a. C. Lewis, W. R. Ware, L. J. Doemeny, and T. L. Nemzek, Rev. Sci. Instrum. 44, 107 (1973).
 b. S. A. Nowak and F. E. Lytle, Appl. Spec. 45, 728 (1991).

- 10.a. R. Flesch, E. Ruhl, K. Hottmann, and H. Baumgartel, J. Phys. Chem. 97, 837 (1993). b. A. B. Cornford, D. C. Frost, F. G. Herring, and C. A. McDowell Disc. Faraday Soc. 54, 56 (1972).
- 11. S. Hubinger and J. B. Nee, Chem. Phys. 181, 247 (1994).
- 12. K. A. Peterson and H.-J. Werner, J. Chem. Phys. 96, 8948 (1992).
- 13.a. J. A. Coxon and D. A. Ramsey, Can. J. Phys. 54, 1034 (1976). b. N. Basco and R. D. Morse, Proc. R. Soc. Lond. A. 336, 495 (1974). c. N. Basco and R. D. Morse, J. Mol. Spec. 45, 35 (1973).
- 14.a. D. K. Bulgin, J. M. Dyke, N. Jonathan, and A. Morris, J. Chem. Soc. Faraday Trans. 3 75, 456 (1978).
- N. P. L. Wales, W. J. Buma, and C. A. de Lange, Chem. Phys. Lett. 259, 213 (1996).
- 16.a. D. A. Shirley, ed., <u>Electron Spectroscopy</u>, Amsterdam, North-Holland, 1972, p 345-350. b. A.-L. Roche, K. Kirby, S. L. Guberman, and A. Dalgarno, J. Elec. Spec. 22, 223 (1981).
- 17. J. L. Gardner and J. A. Samson, J. Chem. Phys. 62, 4460 (1975).
- 18.a. J. L. Franklin and J. G. Dillard, ed., Nat. Stan. Ref. Data Ser. NBS26 (1969).
 b. N. Johnathan, A. Morris, D. J. Smith, and K. J. Ross, Chem. Phys. Lett. 7, 497 (1970).
- 19. C. E. Moore, Atomic Energy Levels, NBS Circ. 467, 1949.

Appendix 1

Derivation of the Two-step Photodissociation Model

The most general sequential photodissociation model is:



Upon excitation of a pump pulse, the molecule is placed on the A 2 A₂ state, which is denoted as OClO*. Subsequently, it can cross to OClO† intermediate state with a rate constant, k_1 . From there, the molecule can return to OClO* by rate constant k_2 , or dissociate to ClO and O by rate constant k_2 , or dissociate to Cl and O₂ by rate constant k_2 . Anywhere along this path, a number of probe pulses ionize the transient species or products. There are two sources of product ions: ionization of OClO† leads to an excited electronic state of the ion, which spontaneously dissociates, and the second source is ionization of the neutral products.

The corresponding rate equations are:

$$\frac{d[OCIO^*]}{dt} = -k_1[OCIO^*] + k_{-1}[OCIO^{\dagger}]$$
 [1]

$$\frac{d[OClO^{\dagger}]}{dt} = k_1[OClO^*] - (k_{-1} + k_2)[OClO^{\dagger}]$$
 [2]

$$\frac{d[ClO]}{dt} = \frac{d[O]}{dt} = k_2^a [OClO^{\dagger}]$$
 [3]

$$\frac{d[Cl]}{dt} = \frac{d[O_2]}{dt} = k_2^b [OClO^{\dagger}].$$
 [4]

Equations [3] and [4] can be simplified because k_1 is the rate limiting step. This is justified by the high resolution absorption measurements of the A 2A_2 state, which determined the lifetime of 3.2 eV excitation to be 6.6 ps (1), even though the angular photofragment experiments measured the lifetime measured to be significantly shorter (2). This implies that the dissocition from the intermediate state is faster than rate of crossing from the A 2A_2 state. Therefore, the time behavior of the products is reduced to:

$$\frac{d[products]}{dt} = k_2[OClO^{\dagger}],$$
 [5]

where:
$$k_2 = k_2^a + k_2^b$$
. [6]

A general solution of the coupled rate equations [1], [2], and [5] is (3):

$$[OCIO*](t) = Ae^{-kt} \cosh(k_b t)$$

$$\left[OClO^{\dagger}\right](t) = Be^{-kA} \sinh(k_b t)$$
 [5]

$$[products](t) = \sigma_1 e^{-k_b t} \sinh(k_b t) + \sigma_2 \left\{ 1 - e^{-k_b t} \left[\cosh(k_b t) + \frac{k_a}{k_b} \sinh(k_b t) \right] \right\}, [6]$$

where:

$$k_a = \frac{k_1 + k_{-1} + k_2}{2}, [7]$$

$$k_{b} = \sqrt{k_{a}^{2} - k_{1}k_{2}}.$$
 [8]

The hyperbolic cosine and sine functions are defined as (2):

$$\cosh(x) = \frac{1}{2} \left[e^x + e^{-x} \right],$$
 [9]

$$\sinh(x) = \frac{1}{2} \left[e^x - e^{-x} \right].$$
 [10]

It is impossible to obtain k_1 , k_{-1} , and k_2 , because there only two equations that define them. The solution can be simplified, however, because the high resolution absorption data observed neither an extra transition nor an extra perturbation near 3.2 eV excitation, implying that there is a large difference of the density of states between the A^2A_2 state and the dark 2A_1 and 2B_2 states (1). Once the molecule reaches OClO[†], the probability of it returning to OClO* is small. Therefore, k_{-1} can be ignored, and the photodissociation model is reduced to:

OCIO+ OCI+, O+, CI+, O₂+ OCI+, O+, CI+, O₂+

$$hv_{probe}$$
 hv_{probe}
 hv_{probe}
 hv_{pump}
OCIO

OCIO

OCIO

 hv_{pump}
OCIO

The products time behavior, R(t), is:

$$R(t) = \sigma_1 \left[\exp(-k_2 t) - \exp(-k_1 t) \right] + \sigma_2 \left[1 - \left[1 - \frac{k_1 + k_2}{k_1 - k_2} \right] \left(\exp(-k_2 t) - \exp(-k_1 t) \right) \right]$$
[11]

The σ_1 term corresponds to dissociative ionization of the OClO[†], and the σ_2 term corresponds direct ionization of the neutral products. The strength of this model is that two rate constants, k_1 and k_2 , can be used to fit all four products.

Appendix 1 References

- 1.a. E. Richard and V. Vaida, J. Chem. Phys. 96, 8948 (1992) b. ibid. 94, 163 (1992).
- 2. H. F. Davis and Y. T. Lee, J. Chem. Phys. 105, 8142 (1996).
- 3. W. E. Boyce and R. C. Di Prima, <u>Elementary Differential Equations and Boundary</u>

 <u>Value Problems</u>, 4th ed., New York, John Wiley and Sons, 1986.
- 4. G. B. Thomas, Jr. and R. L. Finney, <u>Calculus and Analytic Geometry</u>, Reading, MA, Addison-Wesley, 1986.



Report Number (14)	LBNL	40711	
oubl. Date (11)	199708		
Publ. Date (11) Sponsor Code (18) JC Category (19)	DOE/ER;	NSF, XF	DOE/ER

DOE